Experimental study on thermal properties of planetary constituent materials

Youyue Zhang

Graduate school of natural science and technology

Okayama University

Contents

Abstract 1

Part 1. Effect of iron content on thermal conductivity of olivine with implications for cooling history of rocky planets 5

1.1 Abstract 6

1.2 Introduction 6

1.3 Experimental 8

1.4 Results 11

1.5 Discussion 12

1.6 Planetary Applications 21

1.7 Conclusion 26

Reference 28

Tables 34

Figures 39

Part 2. Effect of iron content on thermal conductivity of ferropericlase: implications for planetary mantle dynamics 50

2.1 Abstract 51

2.2 Introduction 51

2.3 Experimental 53

2.4 Results and discussion 56

2.5 Geological implications 64

2.6 Conclusion 69

Reference 71

Tables 76

Figures 80

Part 3. Simultaneous measurements of thermal conductivity and thermal diffusivity of bridgmanite and post-spinel: implications for planetary mantle dynamics and evolution 92

3.1 Abstract 93

3.2 Introduction 93

3.3 Experimental 96

3.4 Results and discussion 97

3.5 Planetary implication 105

3.6 Conclusion 109

References 110

Tables 115

Figures..... 117

Acknowledgements..... 128

Abstract

Planet internal heat transport, which provides the energy for plate tectonics, magnetic field, volcanism and earthquakes, is governed by thermal conductivity of planetary materials. Knowledge of thermal conductivity helps understand the thermal history of the past of a planet, the nowadays thermal dynamics in planetary interior and predicts the future scenario of the activity level of a planetary dynamo. In the complex evolution of terrestrial planets, the constituents of the mantle continue undergoing physical mixing and chemical exchange, and the composition will show heterogenous distribution in different time and space. Inner pressure, temperature conditions will also change with secular cooling. Therefore, to con`strain the thermal evolution and interior thermal state of terrestrial planets, studies of thermal conductivity of constituted components of planetary mantle with variable composition under different conditions are needed.

In the past a few decades, thermal conductivities of minerals have been extensively studied. However, data obtained under high pressure and high temperature are rare, which are mostly determined only under ambient temperature or only determined under one specific pressure. Studies trying to understand composition effect are even less. Moreover, in most methods, thermal conductivity cannot be directly measured, only thermal diffusivity or effusivity was measured, a derived thermal conductivity value based on assumed heat capacity value made systematic errors. Lack of reliable sufficient data, planet simulations always take a rough constant value throughout the whole planetary mantle under any period of the planet, which must result in non-negligible deviation from reality of the planet. Along with recent year human beings more planet exploration missions, efforts of providing systematic accurate thermal properties of planetary are urgently needed.

During my Ph.D. period, I concentrate on application and improvement of a high accuracy pulse

heating method, which allows precise simultaneous measurement of thermal conductivity and thermal diffusivity. Combining multi-anvil high pressure experimental technique, thermal properties of constituted components of planetary mantle now can be accurately measured under conditions from upper mantle to topmost lower mantle of the Earth. The main achievements for thermal properties measurement of terrestrial planet main phases are illustrated as below:

(1) Olivine

Olivine is the most abundant mineral in the terrestrial planet upper mantle and is dominant substance that makes up small asteroids. Thermal conductivity and thermal diffusivity were measured simultaneously for olivine polycrystal with different Fe contents (Fo, Fo_{90}, Fo_{70}, Fo_{50}, Fo_{31} and Fo_{0}) up to 10 GPa and 1100 K. With increasing Fe in olivine, thermal conductivity of olivine first decreases and then slightly increases, the lowest value appeared at composition about Fo_{31} at ambient temperature. The thermal conductivity of Fo_{31} is about 35% of Fo. Compared with single crystal olivine, the grain boundary scattering of polycrystalline olivine lowered the absolute value, pressure dependence and temperature dependence of thermal conductivity. Heat capacity of Fo_{70} and Fo_{50} calculated from λ and κ is independent of pressure and is controlled by nearly constant thermal expansion coefficient with increasing temperature.

The composition dependent thermal conductivity of olivine suggests a warmer upper mantle and thicker crust of Mars than expected. The Fe-poor mantle of Mercury would lead to a faster cooling rate than other terrestrial planets. Olivine dominant asteroids with high Fe content have longer cooling history and smaller thermal inertia on the surface.

(2) Ferropericlase

Ferropericlase is the second most abundant mineral in the Earth's lower. Thermal conductivity and thermal diffusivity were measured simultaneously for polycrystalline ferropericlase with

different Fe contents (Fp_3, Fp_5, Fp_{10}, Fp_{20}, Fp_{30} and Fp_{50}) up to 23 GPa and 1100 K. The measurement results revealed a dramatic effect of Fe that even small addition will decrease the absolute value and pressure dependence of ferropericlase by several times compared with end member MgO. Fe substitution also reduces the temperature sensitivity of thermal conductivity of ferropericlase, leading to a unique nonmonotonic behavior of temperature response.

Based on the systematic measurement data, I derive a universal equation as an applicable tool to estimate thermal conductivity of ferropericlase with variable compositions as functions of temperature and pressure. The results suggest that Fe-poor ferropericlase ($X_{Fe} < 0.1$) is thermal conductor while Fe-rich ferropericlase ($X_{Fe} \geq 0.3$) is likely to work as thermal insulator under terrestrial planet mantle conditions. The highly composition-dependent λ of ferropericlase implicates that the crystallization sequence and depth of ferropericlase may influence the magma ocean cooling of terrestrial planets and results in thermal heterogeneity in the deep mantle.

(3) Post-spinel and bridgmanite

Aluminium (Al)-, iron (Fe)-bearing bridgmanite is the dominant phase in the Earth's lower mantle. Simultaneous measurements of thermal conductivity (λ) and thermal diffusivity (κ) of post spinel and bridgmanite with five different compositions ($MgSiO_3$, $Mg_{0.97}Fe_{0.03}SiO_3$, $Mg_{0.91}Fe_{0.09}SiO_3$, $Mg_{0.97}Al_{0.05}Si_{0.98}O_3$ and $Mg_{0.89}Fe_{0.09}Al_{0.05}Si_{0.97}O_3$) were performed up to 24 GPa and 1100 K. Pressure dependence of thermal properties of bridgmanite was obtained by multi-anvil measurements for the first time. The results show that initial small amount adding of impurity (5 mol% Al or 3 mol% Fe) leads to almost halved λ values. Impurity will decrease not only the absolute value of λ, but also result in smaller pressure, temperature dependence of λ. The impurity influence is not simple linear relationships with substitution amount, additional Al impurity (5 mol%) leads to higher absolute value, pressure dependence and temperature dependence of Fe-

bearing bridgmanite ($Mg_{0.91}Fe_{0.09}SiO_3$), possibly due to increase of ferric iron content.

Low λ value of bridgmanite in MORB will delay the phase transition inside of a subducting slab and result in long time stagnation at the base of transition zone. After peeling of MORB layer, larger λ of bridgmanite in harzburgite will result in quick completion of transition to denser phase inside the slabs due to faster temperature equilibrium and trigger restart of sinking of a stagnant slab. Temperature-sensitive λ value of Mg end member bridgmanite may cause the magma ocean cooling rate difference of Earth and Venus from the initial crystallization of impurity depleted bridgmanite.

Part 1. Effect of iron content on thermal conductivity of olivine with implications for cooling history of rocky planets

1.1 Abstract:

The influence of Fe concentration on heat transport properties of olivine was investigated to understand the cooling history of rocky planets such as Mercury, Mars and asteroids. Thermal conductivity (λ) and thermal diffusivity (κ) were measured simultaneously for olivine polycrystal with different Fe contents (Fo, Fo_{90}, Fo_{70}, Fo_{50}, Fo_{31} and Fo_{0}) up to 10 GPa and 1100 K by a pulse heating method. With increasing Fe in olivine, thermal conductivity of olivine first decreases and then slightly increases. The minimum λ was found to be at composition near Fo_{31}; the absolute λ value of Fo_{31} is about 65% lower than that of Fo. Small amounts of Fe in olivine can strongly reduce the thermal conductivity at low temperature; λ value of Fo_{90} is about 50% of Fo at room temperature. Thermal conductivities of polycrystalline olivine have smaller absolute values and weaker pressure and temperature dependences, compared with those of natural single crystal olivine determined by previous studies. Heat capacity of Fo_{70} and Fo_{50} calculated from λ and κ is independent of pressure and is controlled by nearly constant thermal expansion coefficient with increasing temperature. Smaller λ of olivine aggregate with high Fe content would produce a warmer mantle and, in turn, possibly a thicker crust in the Fe-rich Mars, while heat in the Fe-poor Mercury can escape faster than the other terrestrial planets. Olivine-dominant asteroids with high Fe concentration could have longer cooling history and lower thermal inertia on the surface.

1.2 Introduction

To understand the thermal state and dynamics of the Earth and planetary interiors, knowledge of thermal transport properties of mantle materials is essential. Previous studies have suggested that temperature and pressure dependences of thermal conductivity (λ) can affect mantle convection and plate tectonics involving subduction dynamics. Patterns of convection and temperature distribution can be strongly influenced by the variation of thermal conductivity (e.g.,

Dubuffet et al., 1999; Van den Berg et al., 2002; Tosi et al., 2013). In the Earth, the change of thermal conductivity of materials around and inside the subduction zone can also alter the thermal structure of descending slabs and affect the origin of the deep focus earthquakes (e.g., Hauck et al., 1999; Marton et al., 2005; Maierová et al., 2012).

Olivine is the most abundant mineral in the Earth's upper mantle – believed to make up at least 50% of the mineral proportion in this area. Chemical composition of olivine in the Earth's upper mantle is characterized by high forsterite content around Fo_{90} (e.g., Gaul et al., 2000). For other terrestrial planets, Mercury is believed to have a FeO-poor mantle along with end member silicates (Namur et al., 2016), whereas olivine in the Martian mantle would be more Fe-rich, speculated to be about Fo_{70} (Khan et al., 2018). Recent studies suggested that surface of some asteroids is dominated by Fe-rich olivine, which was found to range from Fo_{49} to Fo_{70} (e.g., Sunshine et al., 2007; Sanchez et al., 2014). Hence, the effect of Fe content in olivine on thermal conductivity could be significant for understanding the thermal structure and cooling history of these terrestrial planets and asteroids.

In the past a few decades, thermal conductivity and diffusivity of olivine with low Fe contents (Fo, Fo_{93}, Fo_{90}) have been extensively investigated under both room pressure (e.g., Kanamori et al., 1968; Chai et al., 1996; Pertermann and Hofmeister, 2006) and high pressure (e.g., Katsura, 1995; Xu et al., 2004; Osako et al., 2004; Chang et al., 2017). In contrast, thermal transport properties of olivine with higher Fe contents were poorly constrained by high pressure experiments (Fujisawa et al., 1968). The available experimental data are insufficient to understand the relationship between thermal conductivity and Fe content of olivine. Therefore, a systematic study is needed to understand the cooling history of terrestrial planets.

Osako (2004) first applied a pulse heating method of one-dimensional sample configuration for

thermal property measurements of mantle materials. By using this method, thermal conductivity and thermal diffusivity can be measured simultaneously, which make it possible to obtain information on heat capacity under high pressure.

In this study, by combining multi-anvil high pressure experimental technique and pulse heating method (Osako et al., 2004), thermal conductivity and diffusivity of olivine were determined simultaneously. Thermal properties of olivine with six different Fe contents (Fo, Fo_{90}, Fo_{70}, Fo_{50}, Fo_{31}, Fo_0) were measured under the Earth's upper mantle condition in a 5000-ton Kawai type multi-anvil press. For Fo_{90}, Fo_{70}, Fo_{50} and Fo_{31}, I measured thermal conductivity and diffusivity up to 10 GPa and 1100 K. For fayalite (Fo_0), taking into consideration the relatively low transition temperature to spinel phase under high pressure, the measurement condition was limited up to 8 GPa and 700 K. For forsterite, I obtained data up to 5 GPa and 1000 K. Based on the present data, I will discuss an origin of effect of Fe content in olivine solid solution on thermal properties and consider an impact on the cooling history of the rocky planetary interiors.

1.3 Experimental

1.3.1 Sample preparation

To obtain sintered olivine aggregate with different Fe contents, well-ground oxides mixtures with different ratio of MgO, Fe_2O_3 and SiO_2 to be desired stoichiometric composition were prepared. The oxide mixtures then were compressed to disk-shaped pellets with 1–2 mm thickness and baked in gas mixture furnace at 1373 K for samples with high Fe content and at 1573 K for samples with low Fe content under iron-wüstite (IW) buffer for more than 8 hours. The oxygen fugacity was controlled by mixing of CO_2 and H_2 gases. Oxides reacted to form olivine at high temperatures in the gas flow. After quench, the recovered pellets were well ground to very fined-grained powder (~1 μm).

Olivine aggregates with different Fe contents were sintered at 1273-1473 K and 1 GPa in an end-loaded piston cylinder apparatus. To remove water from samples, Fe foil with 0.02 mm thickness was used as a sample capsule surrounded by Pyrex glass, which was used as a sample container to prevent generation of cracks during decompression. The recovered samples were cored to cylindrical shape with 2.6 mm diameter. The detailed experimental conditions for each sintering run are shown in Table 1.1.

1.3.2 Sample characterization

Microstructures of the recovered samples were observed by field-emission scanning electron microscope (FE-SEM). All samples exhibited a homogeneous texture with constant grain size. For samples with high Fe contents (Fo_0 and Fo_{31}), the grain size ranged from 5 to 8 μm. For Fo, Fo_{90}, Fo_{70} and Fo_{50}, the grain size was finer and about 1 μm. The chemical compositions of olivine both before and after thermal conductivity measurement were determined by an electron probe microanalyzer (EPMA) (JEOL JXA-8800). The average chemical compositions for each sample are shown in Table 1.2. The water content of low iron content olivine (Fo, Fo90 and Fo70) both before and after the experiments were measured by Fourier-transform infrared (FTIR) spectroscopy. Typical infrared spectra are shown in Fig. 1.1. The samples are dry both before and after the measurement experiments.

1.3.3 Thermal conductivity measurement

In a pulse heating method, three thin disks of the sintered olivine sample are necessary to prepare for measurements. An impulse heater and a thermocouple are set on each interface between two disks, respectively. When the impulse heater heats the sample, thermal perturbation can be detected by the thermocouple.

The temperature disturbance ΔT monitored by thermocouple is expressed as:

$$\Delta T = A\sum_{n=1}^{\infty}\frac{1}{n^2}\sin\frac{n\pi}{3}\sin\frac{n\pi x}{d}\exp\left(-n^2Bt\right)\times\left[\exp(n^2B\tau)-1\right] \quad (t>\tau) \tag{1.1}$$

where t is the time from the start of pulse heating, x is the position measured from the end of the sample, d is the total height of the three thin disks, and τ is the duration of the pulse. The parameters A and B are defined as follows:

$$A = \frac{2Wd}{\pi^2\lambda S} \qquad B = \frac{\pi^2\kappa}{d^2}\ , \tag{1.2}$$

where W is the power of the impulse heating, S is the heater area. Eq. (1.1) can be established under the boundary condition of constant temperature at both sample ends. Given the rapid converge of series (1) for ΔT, summation up to n = 10 yields sufficiently accurate value for current experimental setting. The parameters A and B are determined through the least square fitting of the experimental data to Eq. (1.1) up to n = 15 (Osako et al., 2004).

Fig. 1.2 shows the cell assembly. Two TiB_2-doped BN+AlN disks with 0.25 mm in thickness were used as a main heater to maintain an ambient temperature. The sample temperature was monitored using a thin flattened chromel-alumel thermocouple with 0.02 mm in thickness and 0.2 mm in width, which was inserted on one interface between two sample disks. A molybdenum impulse heater with 2.5 mm diameter and 0.02 mm thickness was placed on another interface to perform a pulse heating. To effectively attain a uniform and nearly one-dimensional heating over the cross section of the sample, the impulse heater was produced by regular photo-etched trench technique. When the transient heat flow generated by pulse heating was applied to the sample disks, the corresponding transient signal was monitored by thermocouple as a peak on the electromotive force (emf). To realize a constant temperature boundary condition, molybdenum blocks were in direct contact with the sample and were used as a heat sink. Zirconia sleeves and blocks were used as a thermal insulator. The thermal insulator sleeve can effectively limit lateral heat flow to achieve

one-dimensional heat flow in the sample.

Measurements were performed at pressure up to 10 GPa and at temperature up to 1100 K (Table 1.1). To avoid generation of inductive noise, the main heater was heated by a direct current (DC) power supply. The resolution of signal caused by pulse heating on the emf of thermocouple was about 0.1 μV. Averaging acquisitions of 128 or 256 were executed to eliminate the electric noise appeared randomly on the oscilloscope. In data acquisition, to counteract inductive noise caused by the pulse current, the direction of the DC pulse current was inverted one after another.

1.4 Results

Thermal conductivity (λ) and thermal diffusivity (κ) of olivine aggregates with different Fe contents measured at room temperature as a function of pressure are shown in Fig. 1.3a and 1.3b, respectively. The sample sizes at the measured conditions were corrected based on the compression data of Abramson et al. (1997) (Fo_{90}), Finkelstein et al. (2014) (Fo) and Zhang et al. (1998) (Fo_0). Errors of λ (ca. 3%) and κ (ca. 2%) mainly comes from the uncertainty of heating area S, pulse heating power W, sample thickness d and the fitting errors of A and B. λ and κ data of all samples show similar trend with increasing pressure and were fitted into a linear expression with a constant pressure derivative. Temperature for each measurement had a small difference ranging from 293 K to 299 K, which may slightly influence the absolute value. The coefficients obtained as fitting parameters are listed in Table 1.3.

Fig. 1.4a and 1.4b show the variation of λ and κ with different Fe contents in olivine at room temperature. Previous measurement data of Osako (2004), Xu (2004), Fujisawa (1968) and Horai (1971) are also plotted in these figures.

Temperature dependence of λ and κ of olivine at 6, 8 and 10 GPa as a function of Fe content are shown in Fig. 1.5. For both end-member compositions (Fo and Fa), temperature dependence data

were only obtained at 5 and 8 GPa, respectively. The changes of sample sizes during heating were corrected based on the data of density change with temperature for olivine with different iron concentration (Chung, 1971). Both λ and κ decrease with increasing temperature, and were fitted by an empirical form, which expresses as $c_0 + c_1/T$, where T is the absolute temperature. All the fitting parameter values are shown in Table 1.3.

The measurement results were also fitted into to a power-law approach which is similar to Xu et al. (2004) to show the combined influence of pressure and temperature on thermal conductivity and diffusivity. The only fitting parameter is the exponent n. The fitting results of the following expressions are given in Table 1.4:

$$\lambda = \lambda_{300K,1bar} \left(\frac{300}{T}\right)^n (1 + aP), \quad \kappa = \kappa_{300K,1bar} \left(\frac{300}{T}\right)^n (1 + bP). \tag{1.3}$$

Here $\lambda_{300K,1bar}$ and $\kappa_{300K,1bar}$ are the thermal conductivity and diffusivity value at 300 K and room pressure derivated from the pressure dependence fitting results (parameter a_1, b_1 in Table 1.3). a and b are the pressure factors, equal to a_0/a_1 and b_0/b_1 respectively (Table 1.3). For thermal conductivity, parameter n values of end members are near 1 while those of compositions are near 0.6. And for thermal diffusivity, n values of all the compositions are near 1, whereas end members are larger than 1 and other compositions are smaller than 1(Table 1.4).

1.5 Discussion

1.5.1 Comparison with previous studies

Fig. 1.6 shows a comparison of data of this study and previous works. The pressure derivative of λ ($\partial \ln \lambda / \partial P$) of Fo_{90} in this study, 1.9 % GPa^{-1}, is smaller than those of single crystal olivine (Fo_{93}) reported by Osako et al. (2004), which are 3-4% GPa^{-1} for all the three principle crystallographic directions. The absolute value of λ determined by this study at room pressure is close to the measurement results of [010] direction in study of Osako et al. (2004) but lower than the other two

directions. Differences of composition and texture of the measured samples could lead to inconsistent results.

Osako et al. (2004) used natural Fo_{93} single crystal, while the samples measured in this study are synthetic Fo_{90} aggregate with small grain size of about 1 μm. In the present study, olivine with higher Fe content (Fo_{90}) can decrease phonon group velocities and small grain size can enhance phonon-boundary scattering. Both effects contribute to a reduction of λ. The effect of grain boundary scattering can be estimated from the following equation:

$$\lambda_{poly}^{-1} = \lambda_{single}^{-1} + NR_{GB}\,, \tag{1.4}$$

where λ_{poly}, λ_{single}, N, and R_{GB} are the thermal conductivities of polycrystalline and single crystal, the number of grain boundaries per meter along heat flow, and the grain boundary thermal resistance, respectively (Smith et al., 2003). Fo_{90} aggregate with small grain size of about 1 μm in this study indicates that N is about 10^6 m^{-1}. Typical value of the grain boundary thermal resistance is in the range $10^{-8} \sim 10^{-7}$ m^2KW^{-1} (Smith et al., 2003). I assumed R_{GB} of Fo_{90} is 5×10^{-8} m^2KW^{-1}. Combined with the present λ_{single} of Fo_{93} (average value of three directions) from Osako et al. (2004), Eq. (1.4) give a quite similar result of λ_{poly} with measurement results of this study at room temperature. I also calculated λ_{single} of Fo from the Fo polycrystal results, using same parameter as Fo_{90}. The value of λ_{single} of Fo at ambient condition is consistent with that calculated from thermal diffusivity value of Fo [001] measured by Pertermann and Hofmeister (2006). The results are plotted in Fig. 1.7. The damped harmonic oscillator-phonon gas model predicts the pressure dependence of λ of minerals:

$$\frac{\partial(\ln\lambda)}{\partial P} = \frac{1}{K_T}\left(4\gamma + \frac{1}{3}\right)\,, \tag{1.5}$$

where K_T is the bulk modulus and γ is the Grüneisen parameter (Hofmeister, 1999). The bulk sound model predicts the pressure dependence of λ of minerals:

$$\frac{\partial(\ln\lambda)}{\partial P} \approx \frac{K'}{K_{\mathrm{T}}} , \tag{1.6}$$

where K_{T} is the bulk modulus and K' is the pressure derivative of bulk modulus (Hofmeister, 2007). I calculated the pressure dependence of λ of Fo and Fo_{90} both models from the model expressed by Eqs. (1.5) and (1.6) using thermoelastic parameters Fo and Fo_{90} (Zhang, 1998; Zha et al., 1998). I assumed an exponential dependence as a function of pressure and the ambient condition values are based on Pertermann and Hofmeister (2006) and Osako et al. (2004). The calculated results from both simple models are in good agreement with single crystal results of Fo_{93} but deviate largely from the calculated Fo single crystal results. The present results also overestimated the absolute value and pressure dependence of polycrystalline olivine. Thus, such simple models cannot be used for the estimation of aggerates as a consequence of complex grain boundary behaviors. Predictions of mineral with Mg end member may also require more improvement.

Xu et al. (2004) used Fo_{90} aggregates with grain size of 30-40 μm, which is much larger than those of samples used by this study, suggesting smaller effect of phonon-boundary scattering. However, the absolute κ value in their study is distinctly smaller than that of samples with small grain size. Their κ values were determined by the Ångström method. The cell design of Xu et al. (2004) is based on that of Katsura (1995), who also obtained very small κ value (Fig. 1.6b). Such lower κ values may be caused by small ratio of the length to the diameter of their samples. In the Ångström method, a periodic heat wave propagates through a sample, and both phase and amplitude depend on λ. This method assumes that the sample dimension is an infinite long circular cylinder. To satisfy this assumption as much as possible, the ratio of the length to the diameter of the sample should be as large as possible, at least several times. Nevertheless, both Xu et al. (2004) and Katsura (1995) applied the sample dimension with a length to diameter ratio close to 1, which would lead to smaller κ values. Although the absolute values in this study are much larger, the

pressure dependence of thermal diffusivity κ ($\partial\kappa/\partial P$) of Fo_{90} is 4% GPa^{-1}, similar to which reported by Katsura (1995). Xu et al. (2004) results showed much larger pressure dependence of thermal diffusivity κ, which is about 9% GPa^{-1}. The abnormal low absolute κ value at 4 GPa may lead to such high-pressure dependence. If only consider their data at 7 and 10 GPa, then the pressure dependence of κ is only about 3% GPa^{-1}. Fujisawa et al., (1986) reported much higher-pressure dependence of κ for forsterite. They used two 0.2 mm chromel-alumel thermocouples at the center and the edge of the sample, respectively, while their sample diameter is only 3 mm. Use of such thick thermocouple could assist heat escape to lateral direction and yielded large error.

The temperature dependence of λ and κ in the present study is similar to Osako et al. (2004) at low temperature (T < 600 K) but apparently smaller at high temperature. The difference between two studies is possibly due to different heat transport process in single crystal and polycrystal at high temperatures. In polycrystalline materials, the Umklapp scattering (phonon-phonon scattering) can weaken with respect to scattering from grain boundaries at high temperatures. The negative influence on λ from phonon-phonon scattering will slack off. Thus, for thermal conductivity, a relatively weaker effect of temperature is expected compared with single crystal. Although the absolute values are different, similar temperature dependence of κ can be seen in data at high temperature by Xu et al. (2004), who also used Fo_{90} polycrystal samples. In spite of their higher absolute value obtained by Fujisawa (1968), who also used polycrystal samples in their thermal diffusivity measurements, the temperature dependence of Fo_0 seems to be consistent with the present result.

It is a matter to consider that the contribution of radiative heat transport cannot be ignored at high temperatures. Gibert et al. (2005) pointed out that a significant radiative transfer in both olivine single crystals and polycrystal aggregates appeared at high temperature (> 600 K) under ambient

pressure. Higher efficiency of radiative heat transport in single crystal at high temperatures is expected because of higher transparency of single crystal. However, pressure effect would reduce contribution of radiative heat transport. Early experimental work implied that iron-bearing minerals for both single crystal and polycrystal generally become optically opaque at moderate pressure in association with an increase of Fe^{3+} concentration (Mao and Bell, 1972). The samples used in this study were buffered by IW buffer and seems to contain less Fe^{3+} than natural olivine. Under high pressure, the present sample should be more optically transparent, giving rise to a higher radiative heat transport contribution and a gentler decay of λ at high temperatures.

In the measured temperature range (< 1100 K), effect of radiative heat transport of Fe-bearing olivine would only be a negligibly small contribution at moderate pressure (> 1 GPa). On the other hand, some studies on optical absorption spectroscopy of Fe-bearing silicate phase at high temperatures suggested that the contribution of the radiative thermal conductivity is even smaller than expected from T^3 dependency (Keppler et al., 2008). Thus, for Fe-bearing olivine, the measurement results in this study can be extrapolated to the condition of lowermost part of the upper mantle using fitting results of Eq. (1.3) (Table 1.4). Although, for Fe-free olivine (forsterite), no significant contribution of radiative thermal conductivity was found in the measurement temperature range, I should take into account of radiative thermal conductivity to extrapolate my data of Fe-poor olivine to higher temperatures.

1.5.2 The influence of Fe content on thermal conductivity (λ)

At room temperature, the variation of λ of olivine aggregates with various Fe contents shows a similar trend at various pressures (Fig. 1.3a). With increasing Fe content, λ decreases and has a minimum value at composition around Fo_{31} (Fig. 1.4a). When Fe content becomes higher than Fo_{31}, λ slightly increases. The absolute λ value of Fo_{31} is about 35% of Fo and about 68% of Fo_{90}

at room temperature. At relatively low temperatures, phonons are considered to be a main carrier for heat transport. Thus, such λ variation against Fe content could be explained by synergistic effects of atomic mass and configuration entropy on phonon. The increase of anharmonicity by Fe substitution could shorten the mean free path of phonons. As a result, Fe enrichment in olivine would lead to a lower λ. On the other hand, in solid solution, reduction of the phonon group velocities by replacement of larger atomic mass (Fe) results in the decrease of λ. The substitution of Fe in Mg site of olivine will raise the configuration entropy, which reaches the maximum value at composition of Fo_{50}. Then the configuration entropy will decrease with an additional increase in Fe content. When only the influence of configuration entropy is considered, the fluctuation of λ should be symmetric as a function of Fe content and has the minimum at Fo_{50}. However, given the lager atomic mass of Fe, the phonon group velocities should monotonically decrease with increasing Fe content, thus, λ should continue to decrease to fayalite composition. As shown in Fig. 1.4a, the variation of λ showing the shift of the minimum value to the high Fe content is attributed to the simultaneous presence of the above two effects.

As temperature increases, the difference in λ among olivine samples with various Fe contents tends to become smaller. According to the fitting equation shown in Table 1.3, the absolute λ value of Fo_{31} at 800 K correspond to 72, 74 and 77% of the value of Fo_{90} at 6, 8 and 10 GPa, respectively. Meanwhile, at temperatures higher than 500 K, the minimum value appears at composition of Fa (Fig. 1.5b). One possible explanation is that phonon scattering become a major factor beyond the influence of configuration entropy because phonon scattering can be effectively enhanced with increasing temperature. Therefore, at relatively high temperatures (> 500 K), temperature and atomic mass are the most important factors controlling λ of olivine.

Thermal conductivity λ of Fo_{90} is about 50% of Fo at 6 GPa and room temperature, λ of Fo_{70} is

43% of Fo, λ of Fo_{50} is 37% of Fo and λ of Fo_{31} is 35% of Fo. From the measurement results, I note that small addition of Fe to the Mg endmember composition (X_{Fe} = 0.1) significantly reduces the lattice thermal conductivity (about 50 %) of olivine at room temperature. However, with the further increase of Fe content, the influence of Fe on λ becomes weaker. Such phenomenon has been also found in other minerals such as bridgmanite and ferropericlase (Manthilake et al., 2011). Mg end member of mantle minerals may have higher λ than those containing small amounts of minor elements at low temperatures. A larger temperature dependence of end members of olivine can also be confirmed by the fitting result. Fo shows a more than twice temperature dependence than Fo_{90}.

The pressure dependence of λ ($\partial\lambda/\partial P$) decreases with increasing Fe content. Hofmeister (2007) discussed several models of vibrational heat transfer and concluded that $\partial \ln\lambda/\partial P$ can be well represented by K'/K_T, which is deduced from bulk sound model. Hard materials such as mantle mineral phases cluster near a K' of 4 (the harmonic value) and recent studies on influence of Fe content on bulk modulus (e.g., Liu et al., 2005) demonstrated that K_T increases with increasing X_{Fe}. Thus, smaller pressure dependence can be predicted from an increase of Fe content according to Hofmeister (2007). Pressure dependence ($\partial\lambda/\partial P$) of Fo is almost three times larger than that of Fo_{90} determined in this study. However, the difference in bulk modulus of Fo and Fo_{90} is negligibly small, which cannot account for simple estimation K'/K_T. Although the reason why there is the large divergence is still unknown, such large discrepancy of λ between Mg end member and minerals with minor elements suggests that it may cause large errors if I simply use λ of the end member composition to simulate the condition of the Earth and planetary interiors. The influence of Fe content on thermal transport should be considered.

Ohta et al. (2017) estimated the Fe concentration effect on thermal conductivity of MgO-FeO

system (Ferropericlase) under various temperatures at 1 bar based on previous data and measurement results by Padture and Klemens (1997) model (Fig. 1.8). In this model, the influence of scattering by solute atom on the thermal conductivity λ can be written as follows:

$$\lambda = \lambda_i \left(\frac{\omega_0}{\omega_M}\right) \arctan\left(\frac{\omega_M}{\omega_0}\right) \tag{1.7}$$

with

$$\left(\frac{\omega_0}{\omega_M}\right)^2 = \frac{AT}{C(1-C)}, \quad \lambda_i = C\lambda_A + (1-C)\lambda_B. \tag{1.8}$$

Here ω_M is the phonon frequency corresponding to the maximum of the acoustic branch of the phonon spectrum, ω_0 is the phonon frequency where the intrinsic mean free path is equal to that due to solute atoms, A is a constant, and C is the concentration of the solute atoms. λ_i is the solid-solution thermal conductivity without the solute-atom phonon scattering, λ_A and λ_B are thermal conductivities with end compositions at a given temperature. I obtained typical n values (1.08, 0.65, 0.6, 0.55,0.6 and 0.83 for Fo, Fo90, Fo70, Fo31 and Fa, respectively) (Table 1.4) to obtain thermal conductivity values under different temperature at 1bar according to Eq. (1.3) and plotted the data points in Fig. 1.8. Data of this study can be well fitted by Eqs. (1.7) and (1.8) especially at higher temperatures, and the constant A value is about 1.5×10^{-4}, 1.8×10^{-4}, 2.7×10^{-4} and 3.7×10^{-4} for 300, 400, 600 and 1000 K, respectively. The small deviation at low temperature might be caused by grain boundary scattering which is more obvious at low temperature. Thermal conductivity values of compositions measured in this study can be calculated from Eq. (1.3) with typical n values for different compositions. This model is useful to predict phonon thermal conductivity values of olivine with any composition, and the calculated values are useful for simulations of thermal evolution of rocky planets consisting of olivine with different iron content.

1.5.3 Heat Capacity

Heat capacity C can be calculated from λ and κ:

$$C = \frac{\lambda}{\rho\kappa} \tag{1.9}$$

Given the boundary condition of this method, the calculated C should be an average value of C_v and C_p. Fig. 1.9 show pressure dependences of C of olivine with different Fe contents and Fig. 1.10 shows a composition dependence of heat capacity. Heat capacities of Fo, Fo_{90} $Fo_{31}$and Fo_0 show apparent negative pressure dependence, whereas C of Fo_{70} and Fo_{50} show almost no pressure dependence within error. C and $\partial C_P/\partial P$ calculated from olivine with different compositions at ambient temperature are compared with those from previous studies in Table 1.5. The heat capacity of Fo under ambient pressure in this study agrees with that observed by calorimetric measurements within 2%. The absolute C value of Fo_{90} is consistent with that obtained from calorimetric measurements (Watanabe 1982) as well as the average value of three directions in Fo_{93} single crystal (Osako et al., 2004). The $\partial C_P/\partial P$ value is more than twice higher than those by Osako et al. (2004), and such discrepancy might be caused by the different states of the measured sample as discussed before. Compared with calorimetric measurements data, C value of Fo_0 at ambient temperature in the present study is about 7 % larger than the result of Watanabe (1982). Heat capacity value of fayalite under ambient pressure in present study is inferred from the high-pressure heat capacity value which were calculated from λ and κ. Given the errors from the results of thermal transport property values measured in this study and the errors of the density under high pressure based on the results of Zhang et al. (1998), such discrepancy is within an acceptable range. In Fig. 1.10, the results of Watanabe (1982; 1987) were also plotted. Large discrepancy appeared at composition of Fo_{31} and Fo_{50}. Such inconsistency maybe caused by the different characteristics of each sample. However, Watanabe (1987) did not report detailed information on Fo_{50} and Fo_{20} samples. Thus, the accuracy of heat capacity of Fo_{70} and Fo_{50} is still in debate. The good agreements of heat capacity of Fo_{100}, Fo_{90} and Fo_0 in this study with calorimetric measurements

indicate the validity of pulse heating method for the investigation of heat capacity of minerals under high-pressure.

Characteristics of the thermal expansion coefficient α from the pressure derivatives of C can be evaluated by the following equation:

$$\left(\frac{\partial C_p}{\partial P}\right) = -\frac{T}{\rho}\left(\alpha^2 + \left(\frac{\partial \alpha}{\partial T}\right)_P\right) \tag{1.10}$$

The temperature derivative of α for olivine with different Fe contents was evaluated using the observed pressure dependences of the heat capacity and typical α value (2.65×10^{-5} K^{-1}). The results are listed in Table 1.5. If the negative small $\partial\alpha/\partial T$ of Fo_{70} and Fo_{50} is definite, α can be expected to be nearly constant, suggesting that the volume change of Fo_{70} and Fo_{50} with temperature is almost linear.

1.6 Planetary Applications

The thermal history of asteroids plays an important role in understanding terrestrial planet formation. The surface composition and temperatures can be detected by infrared telescope facility and radiometer, respectively. Combined with physical properties of minerals measured in the laboratory, thermal models of asteroids can be performed to test viability for postulated heat sources such as ^{26}A1 decay (e.g., Herndon and Herndon, 1977), and to simulate thermal evolution of asteroids (e.g., Ghosh and McSween, 1998) and meteorite parent bodies (e.g., Miyamoto et al., 1981). A wide variation of thermal conductivity of olivine can largely change the modelling results for thermal evolution of asteroids by a direct effect on the thermal conduction process. These values would also alter thermal inertia, which varies as the square root of thermal conductivity, thus affecting the Yarkovsky (e.g., Rubincam, 1965) and YORP (Paddack, 1969) evolution of orbits and spin for solid object. Recent discoveries of monomineralic-olivine asteroids with composition range from Fo_{49} to Fo_{70} (e.g., Sunshine et al., 2007; Sanchez et al., 2014) can be a

good window for understanding terrestrial planet formation.

To understand how the compositional-dependent thermal conductivity would influence the cooling history of asteroids, I perform a simple heat conduction model of asteroids which are only consist of different iron content olivine. This model fully neglects other complex factors related with the thermal evolution of asteroids, such as the role of internal heat sources. Considering various shapes of asteroids, the heat conduction must be simulated by solutions in different geometries. Here I simply simulate cooling process in sphere shape asteroids with different composition. I assume the asteroids only composed of olivine with different Fe contents and the heat only transported by heat conduction. The radius of all the asteroids is assumed to be 500 km. Initially there is uniform temperature distribution within the asteroid and the temperature is assumed to be 1600K. Based on measurement results of this study, I simulate the heat conduction process by software COMSOL^{TM}. I performed the simulation using both a constant thermal conductivity and a temperature-dependent thermal conductivity. Room temperature values were chosen for constant thermal conductivity models, which could maximize the differences between different compositions. I used the heat capacity value reported by Watanabe (1982; 1986). All the asteroids have a diffused surface with a typical thermal emissivity value 0.9 and the surface temperature was set at cosmic background radiation (2.7 K). The Time-dependent study were performed until 4.5 gigayears (Gy). At 4.5 Gy, all the asteroids totally cool down. Here I show the temperature distribution inside of the asteroids at 1 Gy and Time-dependent temperature of the center point of the asteroids with constant thermal conductivity and temperature-dependent thermal conductivity in Fig. 1.11a, b and c, respectively. The simulation results show vital importance of not only the Fe content of olivine but also the temperature dependence of thermal conductivity. Even some variations of Fe content could produce a considerable difference of heat

loss for geological time scale. The temperature dependent thermal conductivity leads to larger difference in heat loss compared with constant thermal conductivity value. The temperature distribution within the asteroids also largely different if I consider the temperature dependence of thermal conductivity (Fig. 1.11). Among all the composition of the asteroids, Mg end member one shows much faster cooling than all the other composition, and almost totally cools down within 1 Gy, while composition of Fo_{31} asteroid still could keep 1200 K at the center at 1 Gy. With a temperature dependent thermal conductivity, asteroid with composition of Fo_{90} is also as cold as about 100 K at 1 Gy while a constant thermal conductivity value yields 400 K at the center. Apparently, temperature-dependent and Fe content-dependent thermal conductivity has non-negligible effect on the thermal evolution of small asteroids. Thus, thermal model of asteroid covered only by olivine with high Fe content like Fo_{49} might produce larger error by using the thermal conductivity values of Fe-poor olivine (Fo_{90} or Fo). Results of this study suggest a longer cooling history for asteroids covered by olivine with high Fe content.

On the other hand, the surface processes of airless bodies are controlled by surface energy balance. Thus, surface inertia, which determines response of surface temperature by insolation, is significant. Thermal inertia Γ is given by

$$\Gamma = \sqrt{\lambda \rho C_p} \tag{1.11}$$

where λ is thermal conductivity, ρ is the density and C_p is heat capacity. Based on the present data on composition dependent λ and C_p, the thermal inertia value of a surface with Fo_{49} composition can be about 20% lower than that with Fo_{90} and 37% lower than with Fo. Although this variation is not bulky compared with the errors of some models for simulation of asteroid surface temperature, for specific olivine-dominant asteroid, more consideration of composition dependent thermal conductivity and heat capacity can improve the accuracy of the models and lead to a better

estimation for Yarkovsky effects.

Bulk composition of the Martian mantle is usually believed to have an enrichment in Fe compared with the Earth's mantle. The mineral phase of the Martian mantle is similar to that of the Earth, consisting primarily of the mineral olivine $(Mg,Fe)_2SiO_4$. However, the depth of olivine stability field is much deeper than the Earth due to the lower gravity of Mars. The phase transition is expected to take place at depth more than 1000 km in Mars, while the radius of Mars is only about 3390 km (Verhoeven et al., 2005). The thermal evolution models of Mars usually have assumed a constant thermal conductivity in mantle and crust with a typical value of 4 $Wm^{-1}K^{-1}$. Schumacher and Breuer (2006) have emphasized the large influence of a variable thermal conductivity on the thermochemical evolution of Mars in their models, especially for the formation of crust. Hahn et al. (2001) suggested that the differences of crustal heat flux are mainly caused by variations of crustal thickness. Thus, a more accurate numerical simulation of the thermal structure and evolution of Mars requires a better constrained database of experimental data on thermal conductivity of various minerals and their dependence on pressure and temperature. The present results match this purpose well. According to Khan et al. (2018), the olivine composition of Mars was assumed to be about Fo_{70}. The thermal conductivity of olivine expected in the Martian mantle can be more than 10% lower than that of Fo_{90}, giving rise to a warmer mantle and a thicker crust than the expectation based on Fo_{90} data. Schumacher and Breuer (2006) estimated thickness of the Martian crust by models with different thermal conductivities of the Martian crust and mantle. A model using 4 $Wm^{-1}K^{-1}$ of λ for both crust and mantle yielded crustal thickness of about 70 km, while model with variable mantle thermal conductivities using the relations for λ (e.g. a typical value is 3.3 $Wm^{-1}K^{-1}$ at 6 GPa and 800 K) provided by Hofmeister (1999) gave a 15 km thicker crust. Considering the composition dependence of λ, the crustal

thickness of Mars is expected to be more than 85 km. The present results suggest that the slower cooling of the inner part could support the global partial melt zone which may explain the existence of the recent volcanism in the Mars.

Mercury is known as a high metal-silicate ratio planet. Its low inferred abundance of FeO (≤ 4 wt %) (Nittler et al., 2011; Weider et al., 2012) in the silicate portion of Mercury could be treated as an end-member among the terrestrial planets. Based on the measurement results of this study, the high thermal conductivity of Fo suggests a fast heat loss through the thin end member mantle. Efficient heat escape from the Mercurian core could influence the magnetic field strengths by affecting the vigor of convection in the liquid outer-core, which is inconsistent with the observed weak magnetic field of Mercury. In addition, high heat flow enhances rapid solidification of the core, which is conflict with the observation of the presence of an active dynamo in Mercury. There are several possibilities which could explain the inconsistency. Firstly, the mantle composition of Mercury may not be the Mg-end member silicate. As shown in Fig. 1.4a, even small addition of Fe from Mg end member will lead to considerable reduction of thermal conductivity. Secondly, there might be abundant radioactive elements in the mantle of Mercury as heat source, which keeping the Mercury's mantle at a relatively high temperature. As shown in Fig. 1.5a, the difference of thermal conductivity by different compositions becomes smaller and thermal conductivity becomes small even for Fo at high temperature. In such case, the heat loss of Mercury will be inhibited. Another possibility is the possible presence of a thin layer with low thermal conductivity as assumed by Grott et al. (2011). Such efficient insulator could also suppress the heat loss of Mercury.

The large discrepancy in thermal transport properties between Fo and impurity-bearing olivine implies that the choice of thermal transport parameter values is significant. To constrain the

thermal structure and evolution of the Mercury, variable thermal conductivities, considering the effect of pressure, temperature and composition, should be used in the numerical models of evolution of Mercury's interior. All the numerical models of evolution of Mercury's interior (e.g., Grott et al., 2011; Michel et al., 2013; Tosi et al., 2013), however, have ignored those effects and chose constant value for mantle thermal conductivity. Grott et al. (2011) and Tosi et al. (2013) used a thermal conductivity of 4 $Wm^{-1}K^{-1}$in their models, while Michel et al (2013) used a lower value of 3 $Wm^{-1}K^{-1}$. The usual preferred thermal conductivity value ($\leq$ 4 $Wm^{-1}K^{-1}$) and thermal diffusivity constant value ($\leq 10^{-6}\,m^2\,s^{-1}$) may yield deviation from the realistic condition of Mercury, especially at the shallow depth of the Mercury's mantle. To distinguish what suppresses the heat loss of Mercury and whether convection can persist in such a thin Fe-poor mantle, composition, pressure and temperature dependent heat transport properties in this study can provide better reference.

1.7 Conclusion

Thermal conductivity and thermal diffusivity of olivine with different Fe contents were measured simultaneously by pulse heating method under high pressure and high temperature. Heat capacity under high pressure was also obtained. The major conclusions of this work are as follows:

i. Thermal conductivity of olivine was varied by different Fe contents and the lowest value appeared at composition about Fo_{31} at room temperature. The thermal conductivity of Fo_{31} was about 70% of Fo_{90} and 35% of Fo.

ii. Compared with single crystal olivine, the grain boundary scattering of polycrystal olivine lowered the absolute value of thermal conductivity and reduced the pressure dependence of thermal conductivity at room temperature and temperature dependence of thermal conductivity under high temperature.

iii. The composition dependent thermal conductivity of olivine suggests a warmer upper mantle and thicker crust of Mars than expected. The Fe-poor mantle of Mercury would lead to a faster cooling rate than other terrestrial planets. Olivine dominant asteroids with high Fe content have longer cooling history and smaller thermal inertia on the surface.

Reference

Abramson, E.H., Brown, J.M., Slutsky, L.J., Zaug, J., 1997. The elastic constants of San Carlos olivine to 17 GPa. J. Geophys. Res. 102, 12253-12264.

Chai, M., Brown, J.M., Slutsky, L.J., 1996. Thermal diffusivity of mantle minerals. Phys. Chem. Miner. 23, 470-475.

Chang, Y.-Y., Hsieh, W.-P., Tan, E., Chen, J., 2017. Hydration-reduced lattice thermal conductivity of olivine in Earth's upper mantle. Proc. Natl. Acad. Sci. 114 (16), 4078-4081, doi:10.1073/pnas.1616216114.

Chung, D. H., 1971. Elasticity and equations of state of olivines in the Mg_2SiO_4-Fe_2SiO_4 system. Geophys. J. Roy. Astron. Soc., 25, 511-538.

Dubuffet, F., Yuen, D.A., Rabinovicz, M., 1999. Effects of a realistic mantle thermal conductivity on the pattern of 3D convection. Earth Planets. Sci. Lett. 171, 401-409.

Finkelstein, G.J., Dera, P.K., Jahn, S., Oganov, A.R., Holl, C.M., Meng Y, Duffy, T.S., 2014. Phase transitions and equation of state of forsterite to 90 GPa from single-crystal X-ray diffraction and molecular modeling. Am Mineral 99, 35-43.

Fujisawa, H., Fujii, N., Mizutani, H., Kanamori, H., Akimoto, S., 1968. Thermal diffusivity of Mg2SiO4, Fe2SiO4, and NaCl at high pressures and temperatures. J. Geophys. Res. 73, 4727-4733.

Gaul, O.F., Griffin, W.L., O'Reilly, S.Y., Pearsona, N.J., 2000. Mapping olivine composition in the lithospheric mantle. Phys. Earth Planet. Int. 182, 223-235.

Ghosh, A., Mcsween, H.Y., 1998. A thermal model for the differentiation of Asteroid 4 Vesta based on radiogenic heating. Icarus 134, 187-206.

Gibert, B., Schilling, F.R., Gratz, K., Tommasi, A., 2005. Thermal diffusivity of olivine single

crystals and a dunite at high temperature: evidence for heat transfer by radiation in the upper mantle. Phys. Earth Planet. Inter. 151, 129-141.

Grott, M., Breuer, D., and Laneuville, M., 2011. Thermo-chemical evolution and global contraction of Mercury. Earth Planet. Sci. Lett., 307, 135-146.

Hahn, B. C., S. M. McLennan, and E. C. Klein, 2011. Martian surface heat production and crustal heat flow from Mars Odyssey Gamma-Ray spectrometry. Geophys. Res. Lett., 38(14), L14203.

Hauk, S.A., Phillips, R.J., Hofmeister, A.M., 1999. Variable conductivity: effects on the thermal structure of subducting slabs. Geophysics. Res. Lett. 26 (21), 3257-3260.

Herndon, J.M., Herndon, M.A., 1977. Aluminum-26 as a planetoid heat source in the early solar system. Meteoritics 12, 459-465.

Hofmeister, A.M., 1999. Mantle values of thermal conductivity and the geotherm from phonon lifetimes. Science, 283, pp. 1699-1706.

Hofmeister, A.M. 2007. Pressure dependence of thermal transport properties. Proc Natl Acad Sci USA 104:9192–9197.

Horai K., 1971. Thermal conductivity of rock-forming minerals. J Geophys Res. 76:1278-1308.

Kanamori, H., Mizutani, H., Fujii, N., 1969. Method of thermal diffusivity measurement. J. Phys. Earth, 17, 43-53.

Katsura, T., 1995. Thermal diffusivity of olivine under upper mantle conditions. Geophys. J. Int. 122, 63-69.

Keppler, H., Dubrovinsky, L.S., Narygina, O., Kantor, I., 2008. Optical absorption and radiative conductivity of silicate perovskite to 125 gigapascals. Science 322, 1529-1532.

Khan A., Liebske C., Rozel A., Rivoldini A., Nimmo F., Connolly J.A.D., Plesa A.-C., Giardini D., 2018. A geophysical perspective on the bulk composition of Mars. J. Geophys. Res., 123, pp. 575-

611.

Liu, L.-G., Chen, C.-C., Lin, C.-C., and Yang, Y.-J, 2005. Elasticity of single crystal aragonite by Brillouin spectroscopy. Physics and Chemistry of Minerals. 32, 97–102.

Maierová, P., Chust T., Steinle-Neumann, G., Čadek O., Čížková, H., 2012. The effect of variable thermal diffusivity on kinematic models of subduction. J Geophys Res. 117: B07202.

Manthilake, M.A.G.M., de Koker, N., Frost, N., McCammon, D.J., 2011. Lattice thermal conductivity of lower mantle minerals and heat flux from Earth's core. Proc. Nat. Acad. Sci. 108, 17901–17904.

Mao, H.K., Bell, P.M., 1972. Electrical conduction and the red shift of absorption in olivine and spinel at high pressure. Science 176, 403-406.

Marton, F.C., Shankland, T.J., Rubie, D.C., Xu, Y., 2005. Effects of variable thermal conductivity on the mineralogy of subducting slabs and implications for the mechanisms of deep earthquakes. Phys. Earth Planet. Int. 149, 53-64.

Michel, N. C., Hauck, S. A., Solomon, S. C., Phillips, R. J., Roberts, J. H., and Zuber, M. T., 2013. Thermal evolution of Mercury as constrained by MESSENGER observations. J. Geophys. Res. Planets, 118, 1033–1044.

Miyamoto, M., Fujii, N., Takeda, H., 1981. Ordinary chondrite parent body: An internal heating model. Proc. Lunar Planet. Sci. Conf. 12th, 1145-1152.

Nittler, L. R., et al., 2011. The major-element composition of Mercury's surface from MESSENGER X-ray spectrometry. Science, 333(6051), 1847–1850.

Namur, O., Collinet, M., Charlier, B., Grove, T. L., Holtz, F. and McCammon, C., 2016. Melting processes and mantle sources of lavas on Mercury. Earth Planet. Sci. Lett., 439, 117–128.

Ohta, K., Yagi, T., Hirose, K., Ohishi, Y., 2017. Thermal conductivity of ferropericlase

in the Earth's lower mantle. Earth Planet. Sci. Lett. 465, 29–37.

Osako, M., Ito, E., Yoneda, A., 2004. Simultaneous measurements of thermal conductivity and thermal diffusivity for garnet and olivine under high pressure. Phys. Earth Planet. Inter. 143–144, 311-320.

Paddack, S.J., 1969. Rotational bursting of small celestial bodies: effects of radiation pressure. J. Geophys. Res., 74, 4379-4381.

Padture, N., Klemens, P., 1997. Low thermal conductivity in garnets. J. Am. Ceram. Soc. 80, 1018–1020.

Pertermann, M., Hofmeister, A.M., 2006. Thermal diffusivity of olivine-group minerals. Am. Mineral 91, 1747–1760.

Rubincam, D.P., 1995. Asteroid orbit evolution due to thermal drag. J. Geophys. Res. 100, 1585-1594.

Sanchez, J.A., Reddy.V., Kelley, M.S., Cloutis, E.A., Bottke, D.N., Nesvorny, D. Lucas, M.P., Hardersen, P.S., Gaffey, M.J., Abell, P.A., Corre, L.L., 2014. Olivine-dominated asteroids: Mineralogy and origin. Icarus 228, 288-300.

Schumacher, S., Breuer, D., 2006. Influence of a variable thermal conductivity on the thermochemical evolution of Mars. J. Geophys. Res. 111: E02006.

Smith, D., Fayette, S., Grandjean, S., Martin, C., Telle, R., Tonnessen, T., 2003. Thermal resistance of grain boundaries in alumina ceramics and refractories. J. Am. Ceram. Soc., 86, pp. 105-111.

Sunshine, J.M., Bus, S.J., Corrigan, C.M., McCoy, T.J., Burbine, T.H., 2007. Olivine-dominated asteroids and meteorites: Distinguishing nebular and igneous histories. Meteoritics and Planetary Science 42, 155-170.

Tosi, N., Grott, M., Plesa, A.-C., and Breuer, D., 2013. Thermochemical evolution of Mercury's

interior, J. Geophys. Res. Planets, 118, 2474–2487.

Tosi, N., Yuen D. A., de Koker N., and Wentzcovitch R. M., 2013. Mantle dynamics with pressure- and temperature-dependent thermal expansivity and conductivity. Phys. Earth Planet. Inter., 217, 48–58.

Van Den Berg, A.P., Yuen, D.A., Allwardt, J.R., 2002. Non-linear effects from variable thermal conductivity and mantle internal heating: implications for massive melting and secular cooling of the mantle. Phys. Earth Planet. Int. 129, 359-375.

Verhoeven, O., Rivoldini, A., Vacher, P., Mocquet, A., Choblet, G., Menvielle, M., Dehant, V., Hoolst, T.V., Sleewaegen, J., Barriot, J.P., Lognonné, P., 2005. Interior structure of terrestrial planets: Modeling Mars' mantle and its electromagnetic, geodetic, and seismic properties. J. Geophys. Res. 110, E04009.

Watanabe, H., 1982. Thermochemical properties of synthetic high-pressure compounds relevant to the Earth's mantle. In: Akimoto, S., Manghnani, M.H. (Eds.), High Pressure Research in Geophysics. Center for Academic Publication, Tokyo, pp. 441–464.

Watanabe, H., 1987. Physical-chemical properties of olivine and spinel solid solutions in the system Mg_2SiO_4-Fe_2SiO_4, High-Pressure Research in Mineral Physics *(*The Akimoto Volume*)*. M.H. Manghnani, and Y. Syono, eds., Terra Scientific Publishing Co., Tokyo/American Geophysical Union, Washington, D.C., pp. 275–278.

Weider, S. Z., Nittler, L. R., Starr, R. D., McCoy, T. J., Stockstill-Cahill, K. R., Byrne, P. K., Denevi, B. W., Head, J. W., and Solomon, S. C., 2012. Chemical heterogeneity on Mercury's surface revealed by the MESSENGER X-ray spectrometer. J. Geophys. Res., 117, E00L05.

Xu, Y., Shankland, T.J., Linhardt, S., Rubie, D.C., Langenhorst, F., Klasinski, K., 2004. Thermal diffusivity and conductivity of olivine, wadsleyite and ringwoodite to 20 GPa and 1373 K. Phys.

Earth Planet. Int. 143–144, 321-336.

Zha, C.S., Duffy, T.S., Downs, R.T., Mao, H.K., Hemley, R.J., 1998. Brillouin scattering and X-ray diffraction of San Carlos olivine: direct pressure determination to 32 GPa. Earth Planet. Sci. Lett. 159, 25–33.

Zhang, L., 1998. Single crystal hydrostatic compression of (Mg,Mn,Fe,Co)2SiO4 olivines. Phys Chem Min 25, 308-312.

Tables

Table 1.1 Summary of sintering and measurement experimental conditions.

Run No.	Starting material	Capsule	T (K)	Duration (min)	Run No.	P (GPa)	T (K)
PC697	Fo powder	Fe	1473	30	5K3316	Up to 5 GPa	Up to 1000 K
PC666	Fo_{90} powder	Fe	1473	30	5K3271	Up to 10 GPa	Up to 1100 K
PC661	Fo_{70} powder	Fe	1373	30	5K3251	Up to 10 GPa	Up to 1100 K
PC646	Fo_{50} powder	Fe	1273	10	5K3239	Up to 10 GPa	Up to 1000 K
PC655	Fo_{31} powder	Fe	1273	10	5K3267	Up to 10 GPa	Up to 1000 K
PC618	Fa powder	Fe	1273	10	5K3143	Up to 8 GPa	Up to 700 K

All these experiments were conducted at 1 GPa. For high iron content sample, duration is shorter to avoid large grain size.

Table 1.2 Chemical composition of synthetic olivine aggregates before and after thermal conductivity measurement.

	PC618	PC646	PC655	PC661	PC666	PC697
SiO_2	29.52	35.90	33.79	38.00	39.88	41.96
MgO	0	23.65	13.73	35.83	48.47	56.24
FeO	69.75	41.63	53.61	26.84	9.91	0
Total	99.26	101.18	101.13	100.67	98.26	98.20
$Mg^{\#}$	0	50	31	70	90	100
	5K3143	5K3239	5K3248	5K3251	5K3271	5K3316
SiO_2	29.89	35.30	32.25	37.28	40.70	42.56
MgO	0	23.79	13.23	35.07	50.79	56.90
FeO	69.43	41.65	54.00	26.90	10.32	0
Total	99.32	100.73	99.48	99.26	101.81	99.46
$Mg^{\#}$	0	50	31	70	90	100

For each sample, five different spots were analyzed.

Table 1.3 Coefficients of fitting parameters of thermal conductivity λ and thermal diffusivity κ

Olivine	$\lambda = a_0P + a_1$		$\kappa = b_0P + b_1$	
	a_0 ($Wm^{-1}K^{-1}$)	a_1 (GPa^{-1})	b_0 ($10^{-6}m^2s^{-1}$)	b_1 (GPa^{-1})
Fo	0.289	8.114	0.122	3.077
Fo_{90}	0.096	4.490	0.040	1.649
Fo_{70}	0.089	3.733	0.020	1.317
Fo_{50}	0.082	3.142	0.021	1.285
Fo_{31}	0.074	3.034	0.023	1.208
Fo_0	0.064	3.502	0.027	1.097
Olivine	P (GPa)	$\lambda = c_0 + c_1/T$	$\kappa = C_0 + C_1/T$	
		c_0 ($Wm^{-1}K^{-1}$)	c_1 (Wm^{-1})	C_0 ($10^{-6}m^2s^{-1}$)	C_1 ($10^{-6}m^2s^{-1}K$)
Fo	5	-0.195	2836	-0.349	1149.8
Fo_{90}	6	1.216	1132.7	0.221	491.7
Fo_{70}	6	1.301	857.7	0.222	346.6
Fo_{50}	6	1.197	745.7	0.258	320.8
Fo_{31}	6	0.927	766.1	0.122	355.1
Fo_{90}	8	1.255	1188	0.227	505.3
Fo_{70}	8	1.284	947.2	0.215	358.2
Fo_{50}	8	1.209	779.8	0.257	334.3
Fo_{31}	8	1.069	766.6	0.202	333.5
Fo_0	8	0.569	1018.9	-0.069	401.8
Fo_{90}	10	1.27	1236.7	0.227	521.9
Fo_{70}	10	1.335	963.8	0.21	371.5
Fo_{50}	10	1.248	782.6	0.187	372.7
Fo_{31}	10	1.236	755.5	0.221	227.2

Table 1.4 parameters derived from fitting the equations $\lambda = \lambda_{300K,1\ bar}(300/T)^n(1+aP)$ and $\kappa = \kappa_{300K,1\ bar}(300/T)^n(1+bP)$ to the experimental data

Olivine	P(GPa)	$\lambda = \lambda_{300K,1\ bar}(300/T)^n(1+aP)$		$\kappa = \kappa_{300K,1\ bar}(300/T)^n(1+bP)$	
		n	$a=a_0/a_1$	n	$b=b_0/b_1$
Fo	5	1.087	0.036	1.275	0.04
Fo_{90}	6	0.667	0.021	0.839	0.024
Fo_{90}	8	0.662	0.021	0.855	0.024
Fo_{90}	10	0.673	0.021	0.877	0.024
Fo_{70}	6	0.6	0.024	0.812	0.015
Fo_{70}	8	0.608	0.024	0.84	0.015
Fo_{70}	10	0.62	0.024	0.844	0.015
Fo_{50}	6	0.545	0.026	0.795	0.016
Fo_{50}	8	0.576	0.026	0.817	0.016
Fo_{50}	10	0.621	0.026	0.897	0.016
Fo_{31}	6	0.655	0.024	0.925	0.019
Fo_{31}	8	0.603	0.024	0.857	0.019
Fo_{31}	10	0.574	0.024	0.88	0.019
Fa	8	0.831	0.018	1.145	0.025

Table 1.5 List of heat capacity, $\partial C_P/\partial P$ and $\partial\alpha/\partial T$ for olivine with different Fe contents

	$C\|_{P=0}$ ($Jkg^{-1}K^{-1}$)	$\partial C_P/\partial P$ ($Jkg^{-1}K^{-1}Pa^{-1}$)	$\partial\alpha/\partial T$
Fo (this study)	819	-8.00×10^{-9}	8.61×10^{-8}
Fo_{90}	815	-7.19×10^{-9}	7.94×10^{-8}
Fo_{70}	798	0	-7.02×10^{-10}
Fo_{50}	652	0	-7.02×10^{-10}
Fo_{31}	631	-8.67×10^{-10}	1.07×10^{-8}
Fo_{0}	719	-6.72×10^{-9}	9.86×10^{-8}
Fo (Watanabe 1982)	828		
Fo_{93} (Osako et al., 2004)	801	-3.31×10^{-9}	3.69×10^{-8}
olivine (Watanabe 1982)	816		
Fo_{0} (Watanabe 1982)	827		

Figures

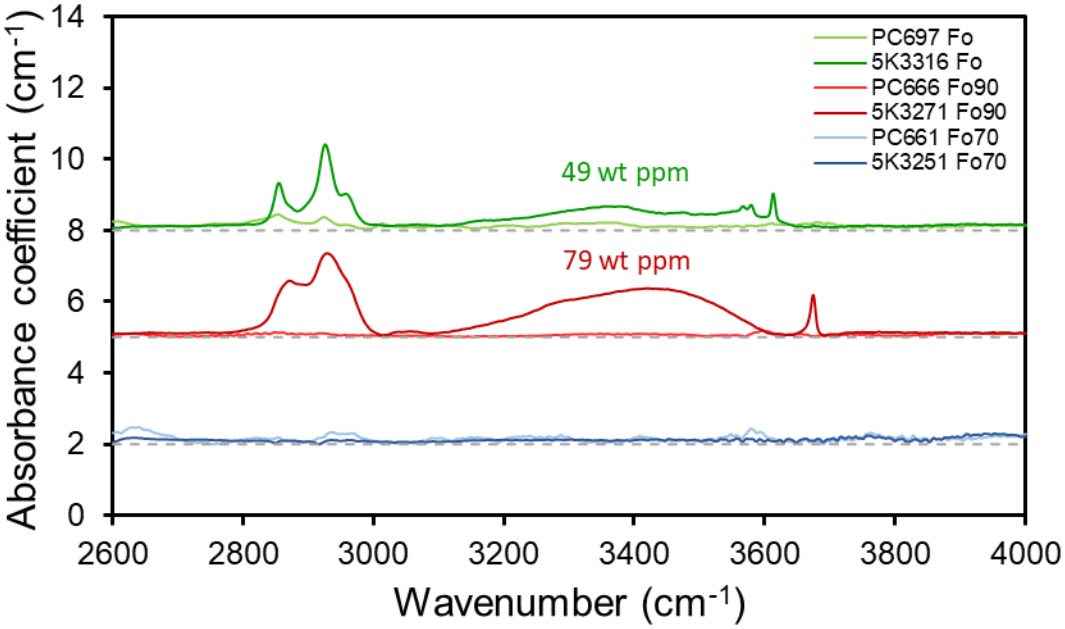

Fig. 1.1 Representative FTIR spectra of Olivine with low iron content. Note that absorption peak at around 2800-3000 cm^{-1} in 5K3316 and 5K3251 may arise from the C-H stretching vibrations of hydrocarbon species (epoxy resin). To obtain water content, contributions from epoxy were subtracted. Paterson's calibration (Paterson, 1982) was used to calculate the water content, the integration range is 3000-3780 cm^{-1}.

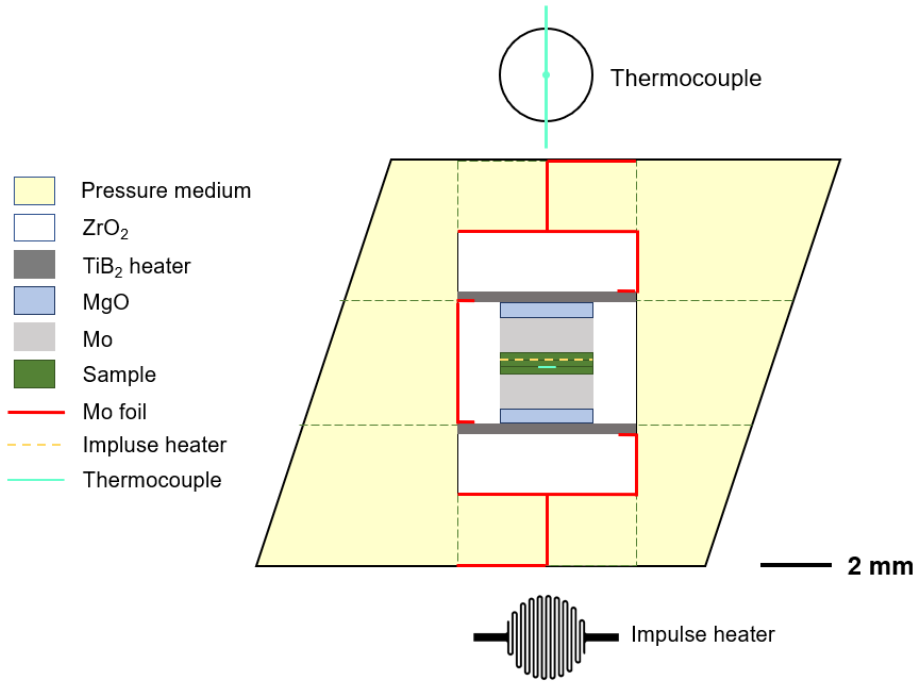

Fig. 1.2 The cross section of the cell assembly for thermal conductivity measurement.

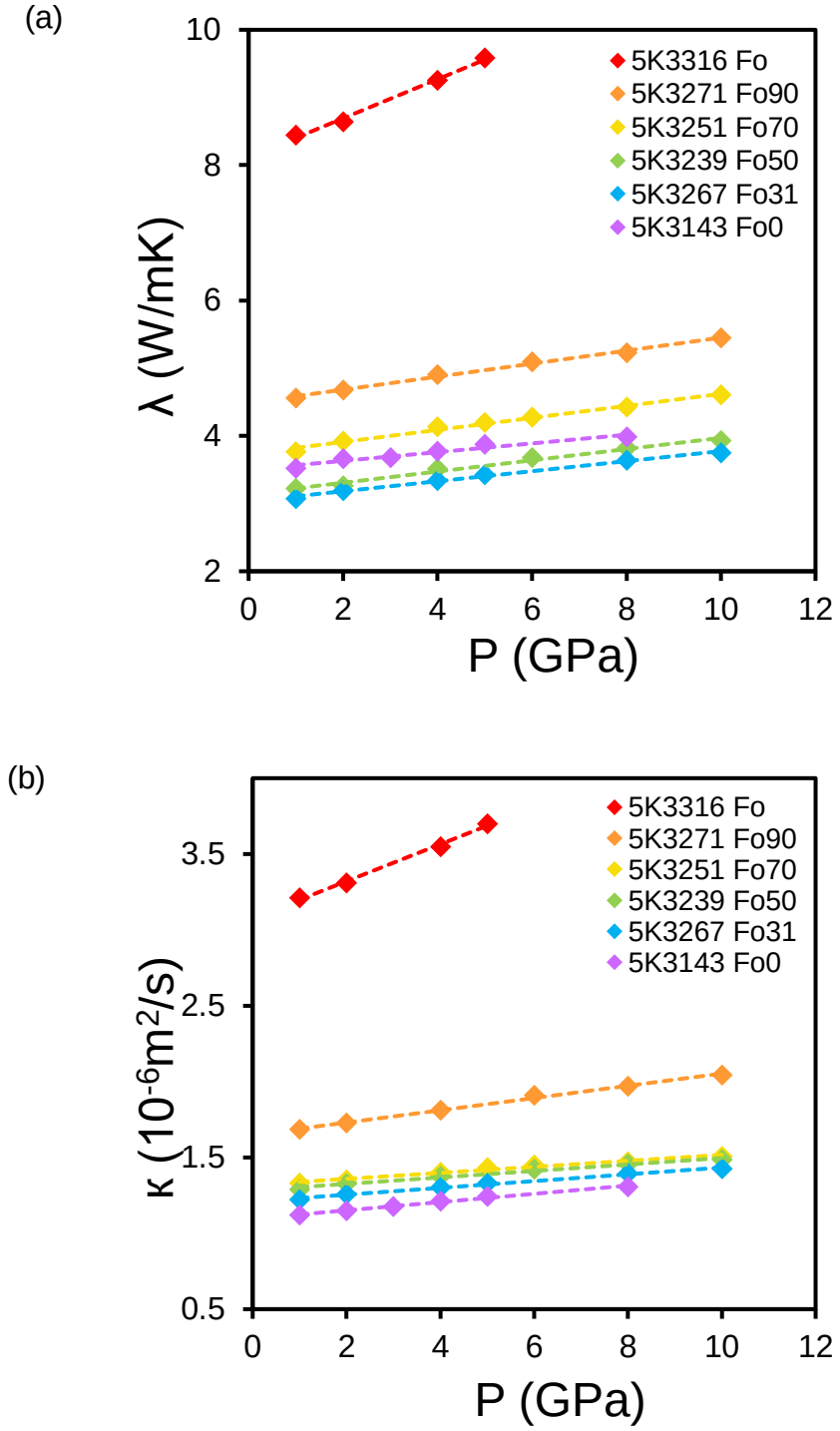

Fig. 1.3 (a) Pressure dependence of thermal conductivity λ of olivine with different composition at room temperature. (b) Pressure dependence of thermal diffusivity κ of olivine with different composition at room temperature.

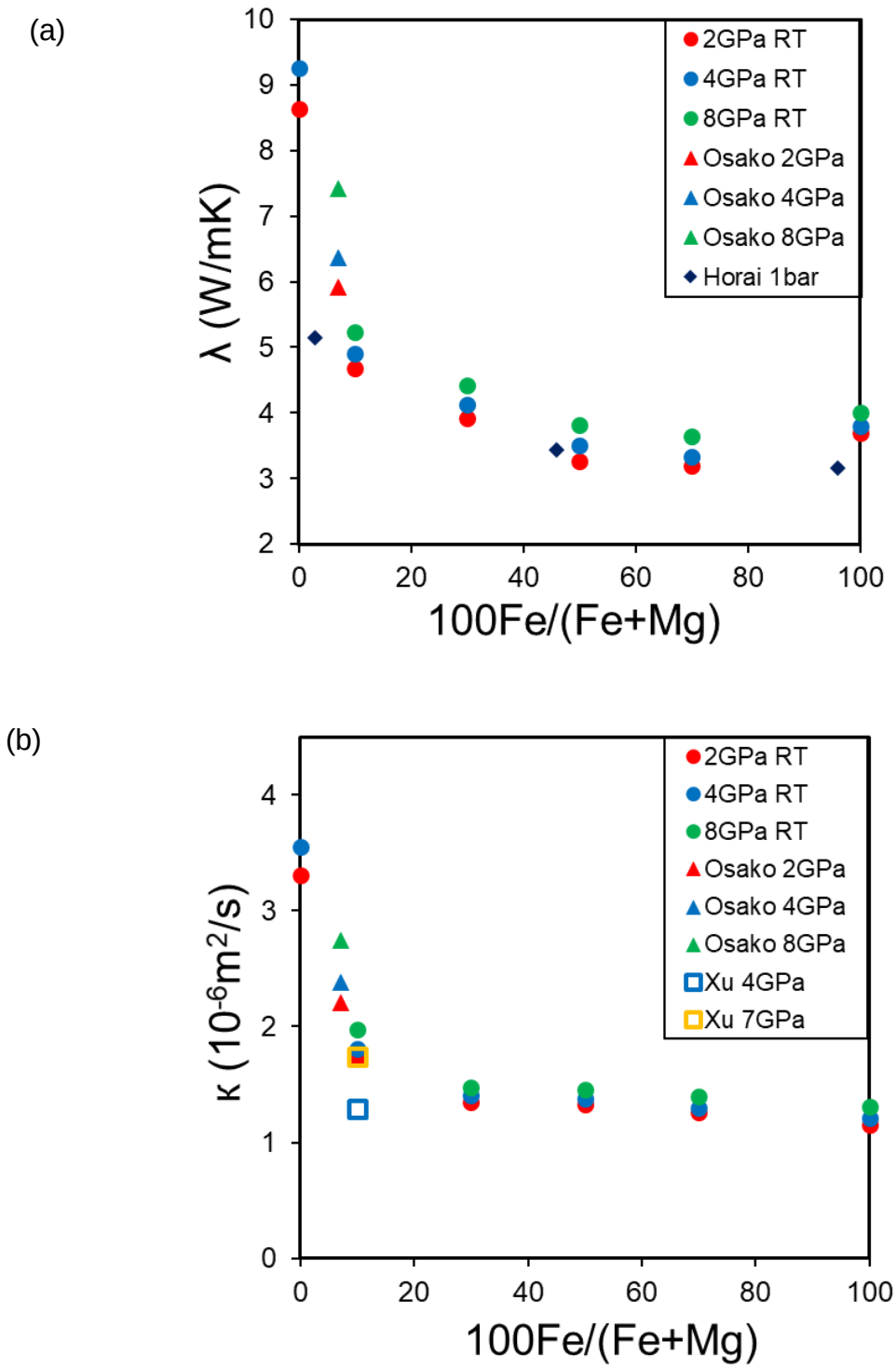

Fig. 1.4 (a) Compositional dependence of thermal conductivity λ of olivine at room temperature. (b) Thermal diffusivity κ of olivine as a function of Fe content at room temperature.

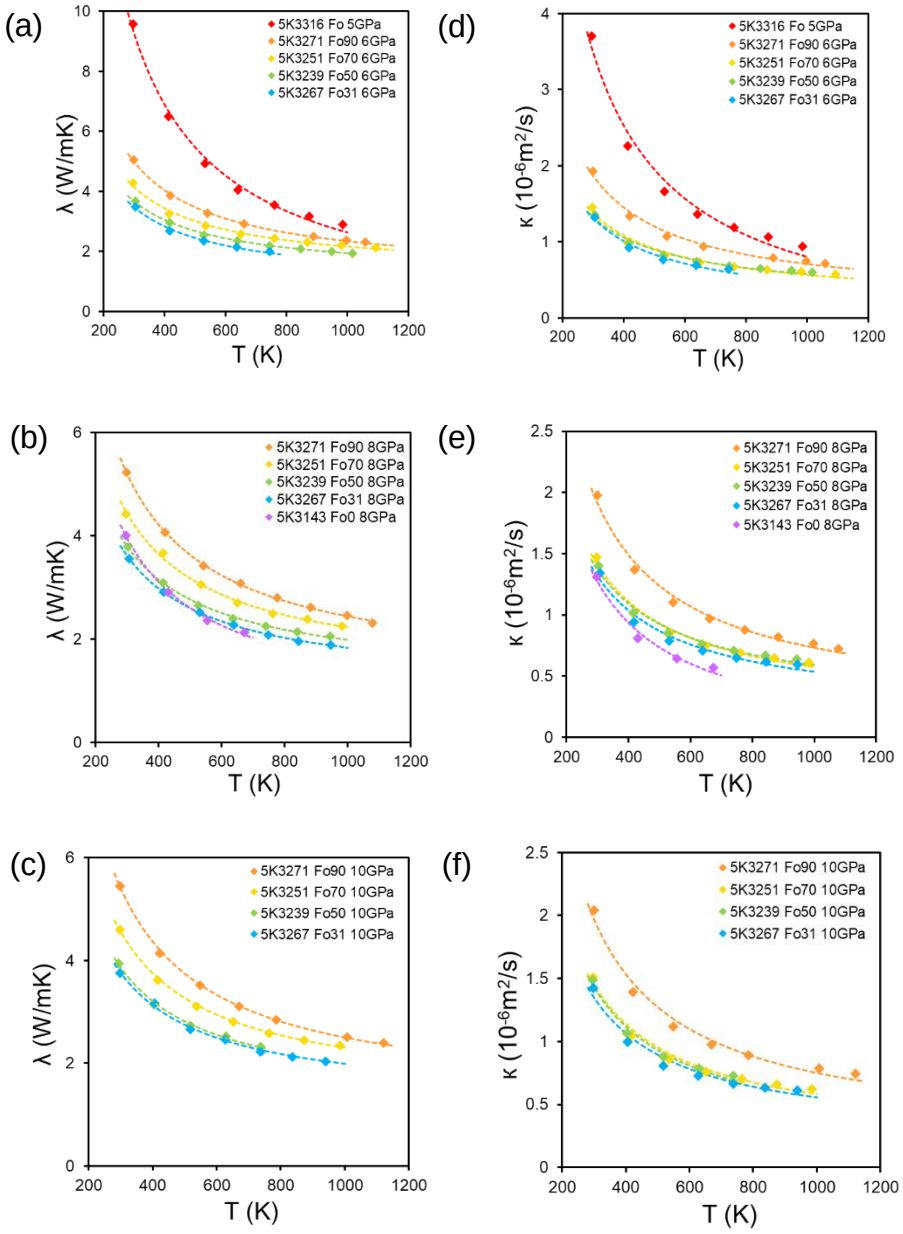

Fig. 1.5 Temperature dependence of thermal conductivity λ of olivine with different Fe contents at different pressures (a) 6 GPa, (b) 8 GPa and (c) 10 GPa. Temperature dependence of thermal diffusivity κ of olivine with different Fe contents at different pressures (d) 6 GPa, (e) 8 GPa and (f) 10 GPa.

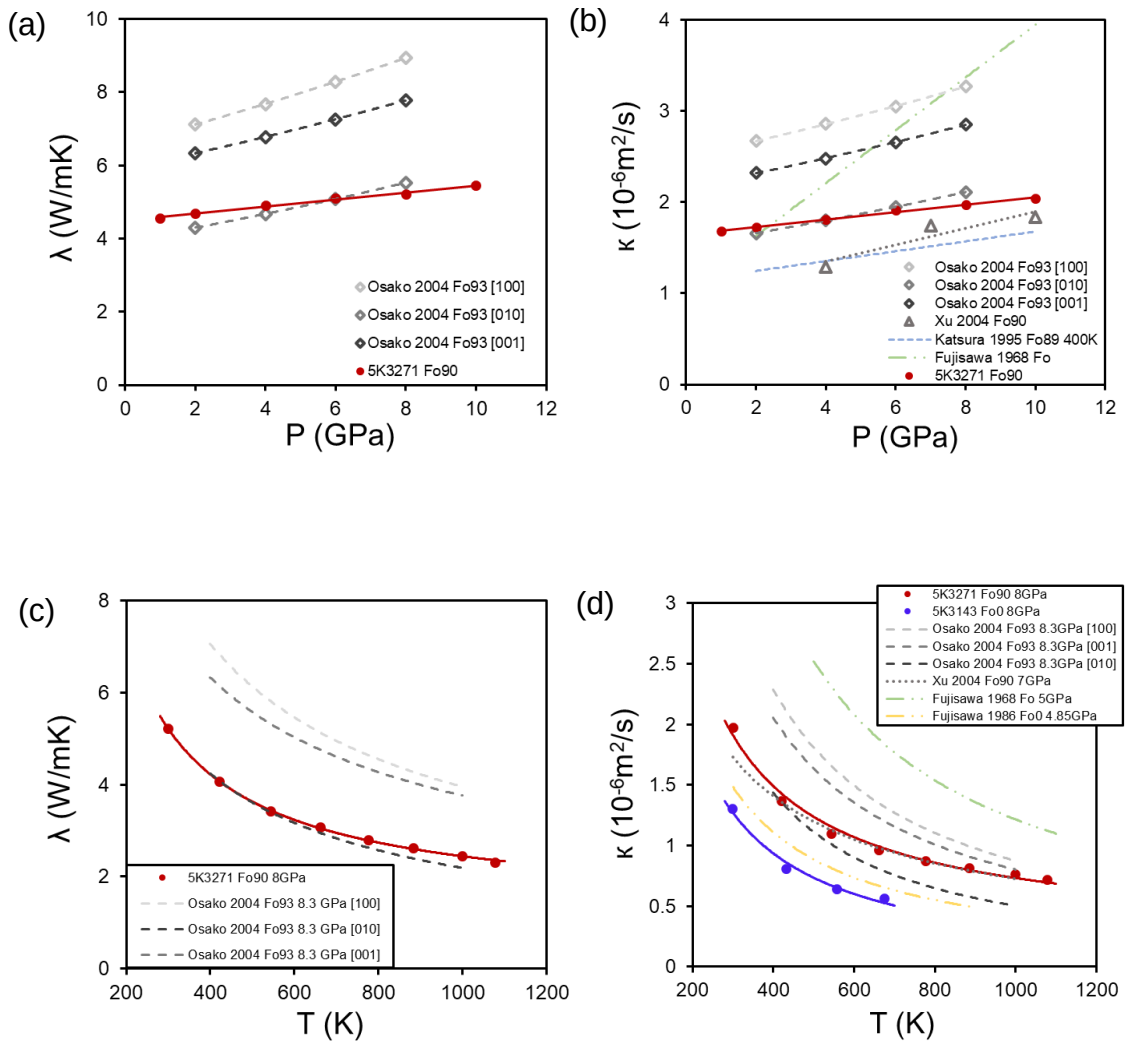

Fig. 1.6 Comparison of thermal conductivity λ and thermal diffusivity κ of olivine with previous results. (a) Pressure dependence of thermal conductivity λ (b) Pressure dependence of thermal diffusivity κ (c) Temperature dependence of thermal conductivity λ (d) Temperature dependence of thermal diffusivity κ

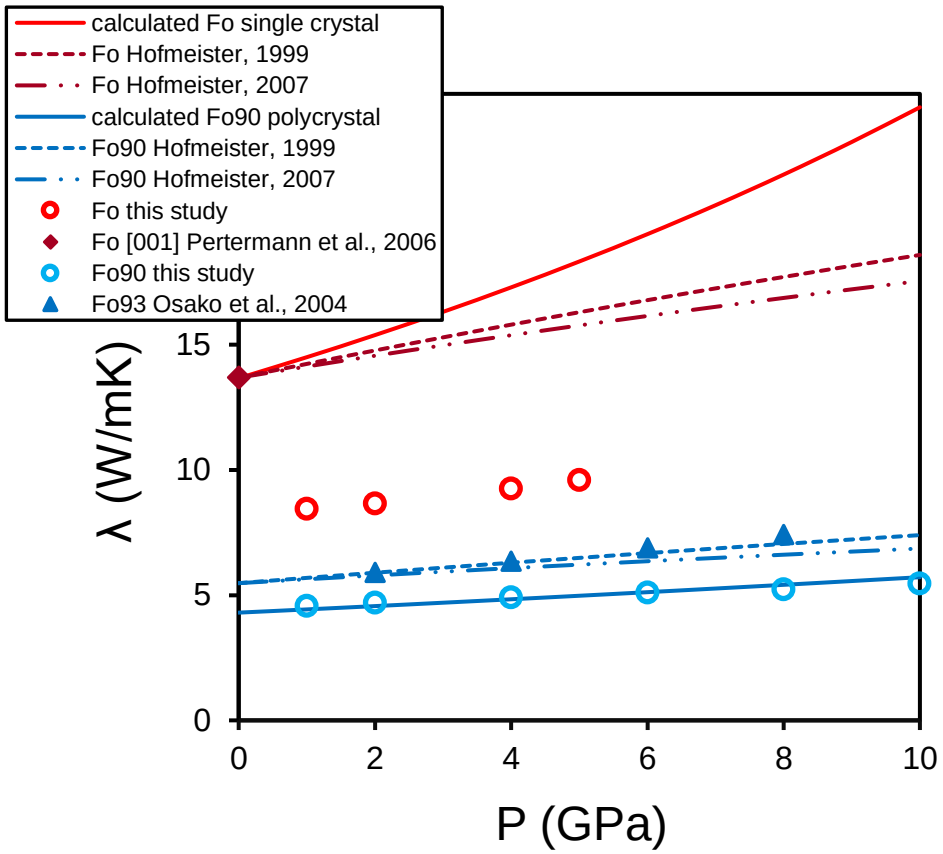

Fig. 1.7 Comparison of thermal conductivity of olivine single crystal λ_{single} and polycrystal λ_{poly} with models' predictions. The conductivity profiles for Fo and Fo_{90} are given by red and blue curves, respectively.

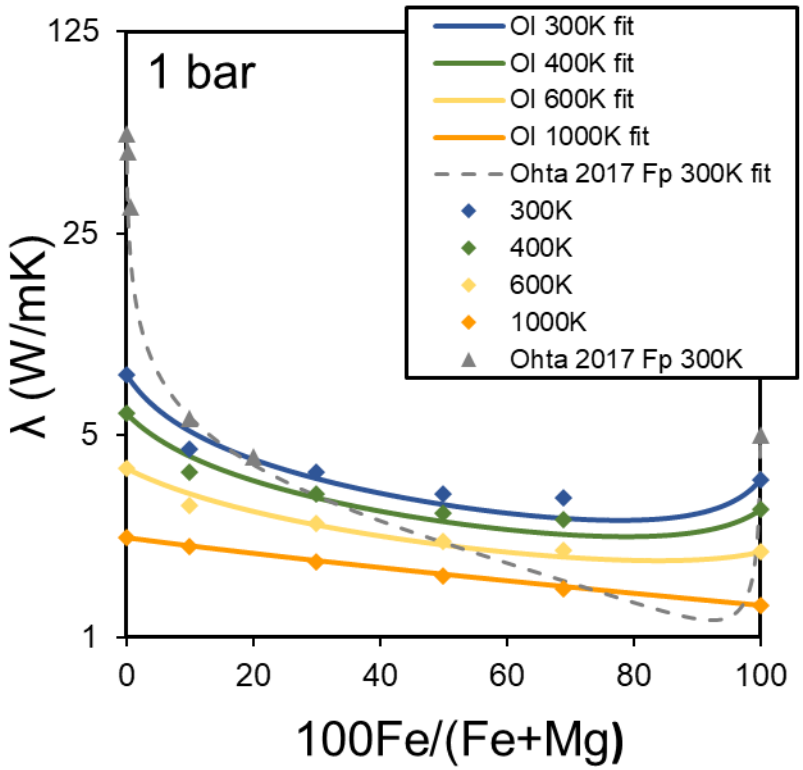

Fig. 1.8 Compositional dependence of thermal conductivity λ under different temperatures at 1 bar.

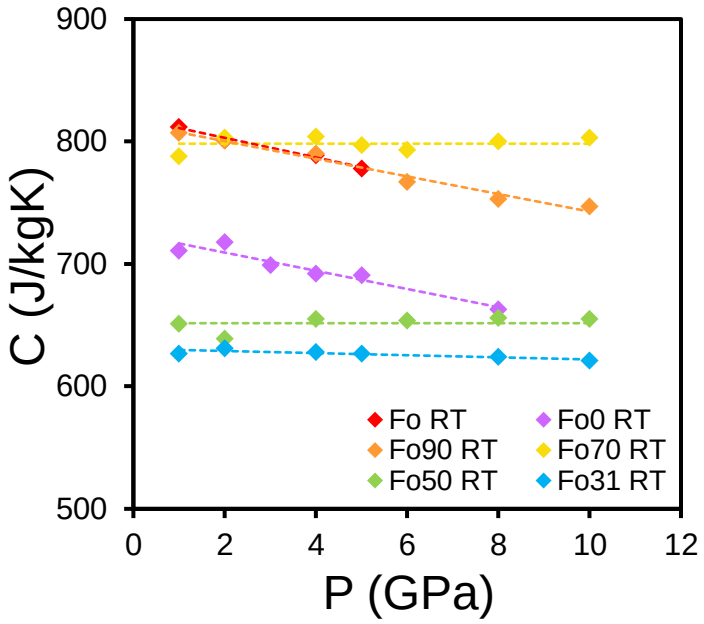

Fig. 1.9 Pressure dependence of heat capacity C of olivine with different Fe content.

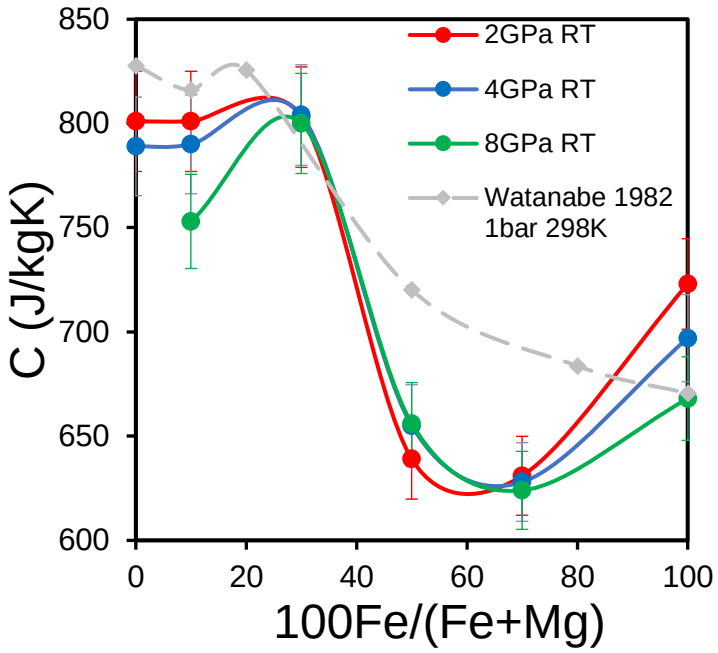

Fig. 1.10 Compositional dependence of heat capacity of olivine at room temperature

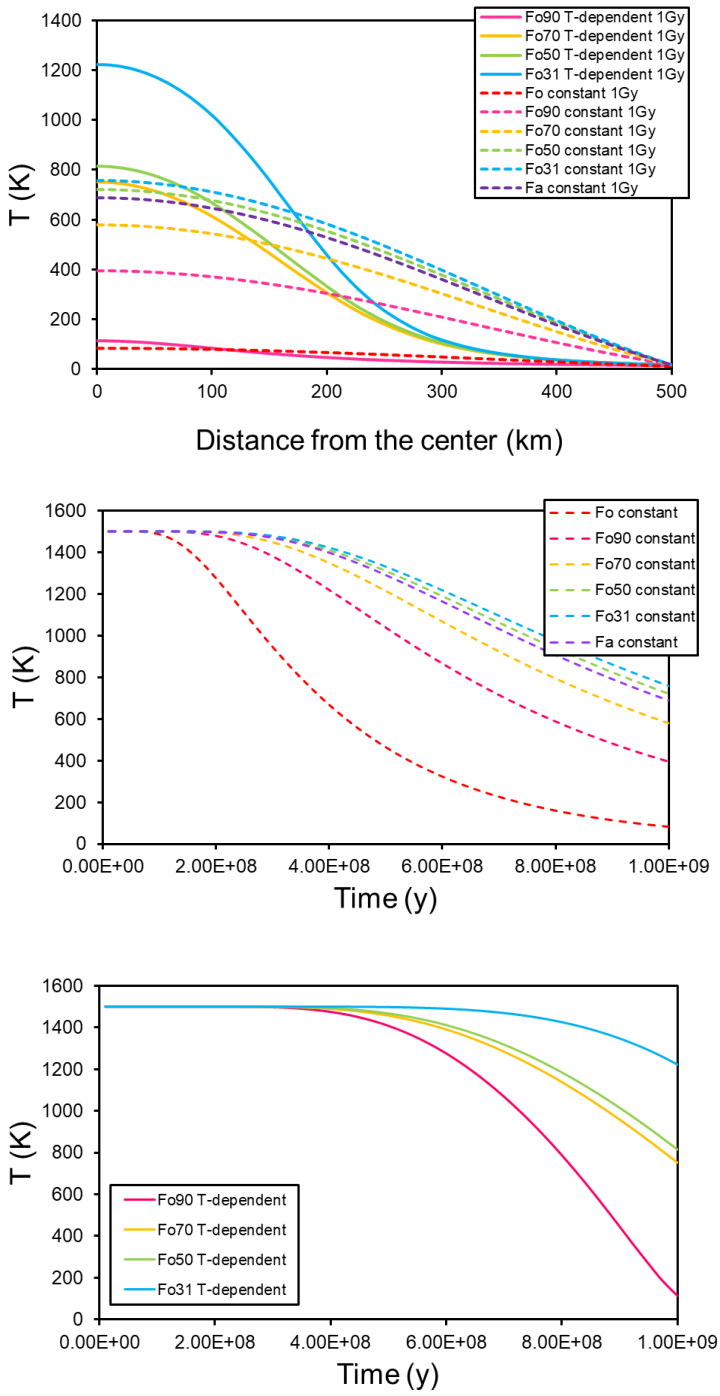

Fig. 1.11 Temperature distribution inside the asteroids with different olivine composition. (a)Temperature distribution inside asteroids at 1 Gy. (b) Time-dependent temperature at the center of the asteroids with constant thermal conductivity. (c) Time-dependent temperature at the center of the asteroids with temperature-dependent thermal conductivity.

Part 2. Effect of iron content on thermal conductivity of ferropericlase: implications for planetary mantle dynamics

2.1 Abstract:

Ferropericlase is the second most abundant mineral in the Earth's lower mantle and can play very different roles in heat transport with the Fe content change under different mantle conditions and earth evolution stage. However, effect of Fe content on pressure- and temperature-dependent thermal conductivity of ferropericlase has been poorly constrained. In this study, thermal conductivity (λ) and thermal diffusivity (κ) were measured simultaneously for polycrystalline ferropericlase with different Fe contents (Fp_3, Fp_5, Fp_{10}, Fp_{20}, Fp_{30} and Fp_{50}) up to 23 GPa and 1100 K by a pulse heating method. Even small amount of Fe in ferropericlase can strongly reduce the thermal conductivity by several times at low temperature compared with MgO periclase. With increasing Fe in ferropericlase, both their pressure and temperature dependence decrease. λ of ferropericlase with various Fe contents is not sensitive to temperature compared with silicates and shows a first increase and then decrease tendency with increasing temperature. A universal equation was derived to estimate λ of ferropericlase with arbitrary composition under planetary mantle conditions. High thermal conductivity of Fe-depleted ferropericlase crystallized at the early stage of cooling of magma ocean may not suppress the heat loss efficiently, whereas ferropericlase with high Fe concentration may prolong the cooling of basal magma ocean at the final stage of magma ocean cooling. This study suggests that Fe content in ferropericlase is an important factor controlling the cooling history of terrestrial planets.

2.2 Introduction

Thermal conductivity (λ) of planetary materials plays a key role in controlling the heat transport in the planetary interior. Knowledge of thermal conductivity helps understand the thermal history of the past of a planet, the nowadays thermal dynamics in planetary interior and predicts the future scenario of the activity level of a planetary dynamo. In the complex evolution of terrestrial planets,

the constituents of the mantle continue undergoing physical mixing and chemical exchange, and the composition will show heterogeneous distribution in different time and space (Trønnes et al. 2019). To constrain the thermal history and interior thermal state of terrestrial planets, studies of thermal conductivity of constituted components of planetary mantle with variable composition are needed.

Ferropericlase is the second most abundant mineral in the Earth's lower mantle. Thermal conductivity of the end member MgO has been extensively studied under high pressures and high temperatures (e.g., Touloukian et al., 1970; Dalton et al., 2013). However, the high thermal conductivity value of such pure composition should not be used for estimating the mantle thermal conductivity as many studies have done before, because in the realistic planetary mantle the Fe substitution could largely influence the thermal properties of ferropericlase. Previous studies indicated that the Fe content in ferropericlase changes with depth on account of that the Fe partitioning between ferropericlase and the other phases is altered by pressure, temperature, oxygen fugacity and spin transition (e.g., Irifune et al., 2010; Sinmyo and Hirose, 2013). In addition, the spatial distribution of ferropericlase may not be homogeneous in the lower mantle depending on the style of the early-stage evolution of the Earth's interior. It has been suggested that a presence of the iron-rich ferropericlase can account for the ultralow velocity zones (ULVZs) observed just above the CMB (Thorne and Garnero, 2004; Wicks et al., 2010). In this region, the efficiency of heat transport to the mantle may be largely different from that of the surrounding mantle. Furthermore, in the early Earth, ferropericlase may influence the cooling process of magma ocean. Thus, understanding these geological problems requires knowledge of the effects of pressure, temperature and composition on thermal conductivity of ferropericlase.

Several studies have measured the thermal conductivity of ferropericlase as a function of pressure

both in a large volume multi-anvil press (Manthilake et al., 2011) and a diamond anvil cell (DAC) (Goncharov et al., 2015; Ohta et al., 2017; Hsieh et al., 2018). However, these studies are poorly consistent with each other, and their methods do not allow measuring thermal conductivity directly. They measured thermal diffusivity (Manthilake et al., 2011; Ohta et al., 2017) and effusivity (Goncharov et al., 2015; Hsieh et al., 2018) instead of thermal conductivity, which may enlarge the error of their results. The temperature dependence of thermal conductivity of ferropericlase was only reported by Manthilake et al. (2011) at only two different pressures. Although the composition dependence was also preliminarily discussed in these studies (Manthilake et al., 2011; Ohta et al., 2017; Hsieh et al., 2018), a unified view applicable to the realistic mantle conditions have not been achieved. More systemic direct measurements of thermal conductivity of ferropericlase under high pressure and high temperature are needed.

In this study, I performed a high accuracy pulse heating method (Osako et al., 2004) combining multi-anvil high-pressure experimental technique. Simultaneous measurements of thermal conductivity and diffusivity of ferropericlase aggregates with 6 different Fe contents (Fp_3, Fp_5, Fp_{10}, Fp_{20}, Fp_{30}, Fp_{50}) were conducted under high pressure up to 23 GPa in a large volume Kawai type multi-anvil press. High temperature data up to 1100 K were obtained for Fp_3, Fp_5, Fp_{10} and Fp_{20}. Based on the present data, I will discuss the effect of Fe content on pressure- and temperature-dependence of thermal properties of ferropericlase. I also discuss the influence of composition dependent thermal conductivity of ferropericlase on the thermal evolution of planetary mantle.

2.3 Experimental

2.3.1 Sample preparation

Starting materials for the thermal conductivity measurements were well-sintered polycrystalline ferropericlase $(Mg_{1-x}Fe_x)O$ with variable compositions (X_{Fe} = 0.03, 0.05, 0.10, 0.20, 0.30 and 0.50).

To obtain ferropericlase with desired compositions, MgO and Fe_2O_3 powders with different ratios were mixed well in agate mortar with ethanol. The oxide mixtures then were compressed to disk-shaped pellets with 1–2 mm thickness and baked in gas mixture furnace at 1573 K under iron-wüstite (IW) buffer for more than 8 hours. CO_2 and H_2 gases flowed into the furnace to control the internal oxygen fugacity, and oxides reacted to form ferropericlase. After quench, the recovered pellets were well ground to fined-grained powder (~1 μm).

Ferropericlase aggregates with different Fe contents were sintered at 1373 K and 1 GPa in an end-loaded piston cylinder apparatus. To keep the oxygen fugacity of samples and eliminate the contamination of water, Fe foil with 0.02 mm thickness was used as a sample capsule. The recovered samples were well-sintered and then cored to cylindrical shape with 2.1 (Fp_3 and Fp_5) or 2.6 mm (Fp_{10}, Fp_{20}, Fp_{30} and Fp_{50}) diameter.

2.3.2 Sample characterization

Phase of the sintered materials was identified by two dimensional (2D) micro-focused X-ray diffractometer (RINT RAPID II) in reflection geometry. The X-ray diffraction patterns were identified to be ferropericlase. Microstructures of the recovered samples were observed by field-emission scanning electron microscope (FE-SEM). All samples exhibited a homogeneous texture with constant grain size. For samples with low Fe contents (Fp_3, Fp_5 and Fp_{10}), the grain size was about 2 μm, for Fp_{20}, Fp_{30}, the grain size was about 3 μm and for Fp_{50} about 5 μm. The chemical compositions of ferropericlase both before and after thermal conductivity measurement were determined by an energy dispersive X-ray spectroscopy (EDS).

2.3.3 Thermal conductivity measurement and improvement of cell assembly

The experiments were conducted by means of the pulse-heating method (Osako et al., 2004; Zhang et al., 2019) in the Kawai-type apparatus (USSA5000). In a pulse heating method, three

thin disks of the sintered ferropericlase sample are required. An impulse heater and a thermocouple are set on each interface between two disks, respectively. When the impulse heater heats the sample, the temperature disturbance ΔT detected by thermocouple can be expressed as:

$$\Delta T = A\sum_{n=1}^{\infty}\frac{1}{\mathrm{n}^2}\sin\frac{\mathrm{n}\pi}{3}\sin\frac{n\pi x}{d}\exp\left(-\mathrm{n}^2\mathrm{B}t\right)\times\left[\exp(\mathrm{n}^2\mathrm{B}\tau)-1\right]\quad(t>\tau) \tag{2.1}$$

where t is the time from the start of pulse heating, x is the position measured from the end of the sample, d is the total height of the three thin disks, and τ is the duration of the pulse. The parameters A and B are defined as follows:

$$\mathrm{A} = \frac{2Wd}{\pi^2\lambda S}\qquad \mathrm{B} = \frac{\pi^2\kappa}{d^2}\ , \tag{2.2}$$

where W is the power of the impulse heating, S is the heater area. Eq. (2.1) is established under the boundary condition of constant temperature at both sample ends. Given the rapid converge of series (1) for ΔT, summation up to n = 10 yields sufficiently accuracy for current experimental setting. The parameters A and B are determined through the least square fitting of the experimental data to Eq. (2.1) up to n = 20.

Fig. 2.1a and 2.1b shows the cell assemblies for thermal conductivity measurement. Two 0.25 mm thick TiB2-doped BN+AlN disks were used as main heaters to provide an ambient temperature. A flattened chromel-alumel thermocouple with 0.02 mm in thickness and 0.2 mm in width was inserted on one interface between two sample disks to monitor the sample temperature. An impulse heater was placed on another interface to perform a pulse heating. The folded shape of impulse heater permitted a uniform and nearly one-dimensional transient heat flow over the cross section of the sample, the corresponding transient signal was monitored by thermocouple as a peak of the electromotive force. To achieve a constant temperature boundary condition, two molybdenum blocks sandwiched the sample in contact with top and bottom sample disks and were used as a

heat sink. The sample part including heat sink and heaters was surrounded by zirconia sleeves and blocks, which can effectively limit lateral heat flow to realize one-dimensional heat flow in the sample.

To achieve higher pressure condition, the 14/8 cell (Fig. 2.1a) used in previous study (Zhang et al., 2019) was improved to a 14/6 cell (Fig. 2.1b). Since smaller truncation of 14/6 cell will cause sample irregular deformed if sample keep previous size, therefore, in 14/6 cell we decrease the sample area diameter from 2.6 mm to 2.1 mm. In this case, previous impulse heater made by molybdenum (Mo) will be hard to keep folded shape with enough number pinches and stably heat the sample. Considering stability of heating and material strength for keep special shape, I chose rhenium (Re) to make smaller size impulse heater. 0.012 mm thick Re foil was cut to disk shape with 17 folded pinches by laser, and Fig. 2.2 shows the self-made Re impulse heater. This new heater has larger resistance around 10 Ω, about 4 times larger the previous Mo impulse heater (resistance about 2.5 Ω). Larger resistance and higher melting temperature allows this new impulse heater providing stable heating under higher pressure and temperature, thus enlarge the application scope of pulse heating method.

Measurements were performed at various pressures up to 23 GPa and at various temperatures up to 1100 K. As Fe content increases, the electrical conduction of the sample disks becomes better, thermocouple and impulse heater which separated by the center disk of sample may cause a short circuit, leading to worse electrical insulation of the whole cell under high temperature. Thus, for high Fe content samples (Fp_{30} and Fp_{50}), only room temperature measurements were performed.

2.4 Results and discussion

2.4.1 Fe effect on pressure response of thermal conductivity of ferropericlase

Fig. 2.3a and 2.3b show thermal conductivity (λ) and thermal diffusivity (κ) of ferropericlase

aggregates with various Fe contents measured at room temperature as a function of pressure, respectively. λ and κ of Fp_{10}, Fp_{20}, Fp_{30} and Fp_{50} monotonically increase with increasing pressure in measured pressure range and were fitted into a linear expression with a constant pressure derivative. For Fp_3 and Fp_5, a slight drop of λ and κ were found at 19 GPa. Above this pressure, λ and κ subsequently increase again. The measurement values at pressures lower than 19 GPa can also be fitted into same function as other Fe contents. The coefficients obtained as fitting parameters are listed in Table 2.1.

The Fe substitution strongly affects both the absolute values and pressure responses of λ. The λ values of Fp_3, Fp_5, Fp_{10}, Fp_{20}, Fp_{30} and Fp_{50} under ambient condition (1bar, 300 K) estimated from linear regression are 11.5, 8.9, 6.3, 3.5, 3.0 and 2.3 $Wm^{-1}K^{-1}$, smaller than MgO periclase (55 $Wm^{-1}K^{-1}$) (Touloukian et al., 1970) by a factor of ~5, 6, 9, 16, 18, 23, respectively. The addition of Fe can enhance the mass disorder, phonon defect scattering and resonant spin-phonon scattering (Morton and Lewis, 1971; Hsieh et al., 2018), which suppress the phonon transport and reduce the thermal conductivity. Such Fe substitution effect is much more pronounced at compositions near the Mg end member, the magnitude of the reduction of λ gradually decreases with increasing X_{Fe}.

The pressure derivative of λ ($d\lambda/dP$) demonstrates difference in order of magnitude (Table 2.1), from the highest increasing rate 0.28 (Fp_3) to the lowest rate 0.01 (Fp_{30}). Such Fe content induced pressure-dependence of λ was also found in olivine solid solution, while the pressure dependence of λ of forsterite (Fo) is about 3~4 times larger than other compositions (Fo_{90}, Fo_{70} Fo_{50}, Fo_{31} and Fo_0) (Zhang et al., 2019). Apparently, effect of Fe content on pressure response of λ for MgO-FeO solid solution is more significant. Such more conspicuous influence can be explained by factors that more defects will be created by substituted iron in MgO-FeO solid solution, unique defect clustering phenomena in $Fe_{1-x}O$ (Catlow and Fender, 1975) and tetrahedral occupancy of ferric

iron in $(Mg_{1-x}Fe_x)O$ (Otsuka et al., 2010).

A previous study reported that $d\lambda/dP$ of MgO periclase is 1.88 (Dalton et al., 2013), which is even two orders of magnitude different from our Fe-rich ferropericlase (Fp_{20}, Fp_{30} and Fp_{50}) results. Fe content can also influence the spin transition pressure of Fe in ferropericlase, for Fe-poor composition, the spin transition may start from a lower pressure (< 30 GPa) (Yoshino et al., 2011). The slight drop of λ of Fp_3 and Fp_5 at about 19 GPa may be associated with the spin transition, which can cause reduction of the bulk sound velocity (Lin et al., 2013) and thus suppress the phonon conduction. For the other compositions, the measured pressure range is not enough to observe such phenomena. If spin transition induced reduction of λ in ferropericlase, λ of Fe-rich composition may have larger difference than Fe-poor one.

λ of ferropericlase has been investigated by several different methods: Ångström method in multi-anvil apparatus (Manthilake et al., 2011), time domain thermoreflectance (TDTR) method in diamond anvil cell (Goncharov et al., 2015; Hsieh et al., 2018) and light pulse thermoreflectance method in diamond anvil cell (Ohta et al., 2017). Polycrystalline ferropericlase samples were used by Manthilake et al. (2011) and Ohta et al. (2017), while single crystals of ferropericlase were used by Goncharov et al. (2015) and Hsieh et al. (2018).

In this study, polycrystalline ferropericlase samples were used. In this case, phonon-boundary scattering effect should be considered. The effect of grain boundary scattering can be estimated by:

$$\lambda_{poly}^{-1} = \lambda_{single}^{-1} + NR_{GB}\,, \tag{2.3}$$

where λ_{poly}, λ_{single}, N, and R_{GB} are the thermal conductivities of polycrystalline and single crystal, the number of grain boundaries per meter along heat flow, and the grain boundary thermal resistance, respectively (Smith et al., 2003). N was determined according to the sample grain sizes observed by FE-SEM. I assumed R_{GB} of ferropericlase is 1.0×10^{-8} m^2KW^{-1}, same as the value of

dense alumina (Smith et al., 2003; Imada et al., 2014). The calculated λ_{single} values are about 20%, 9%, 5%, 2%, 1% and 1% larger than the λ_{poly} values of Fp_3, Fp_5, Fp_{10}, Fp_{20}, Fp_{30} and Fp_{50}, respectively. The grain boundary effect is more significant for Fe-poor ferropericlase (Fp_3, Fp_5 and Fp_{10}). Therefore, I only plot the fitting curve of calculated λ_{single} of Fp_3, Fp_5 and Fp_{10} in Fig. 2.3a and Fig. 2.4 (by dashed-dot-dot lines).

Fig. 2.4 shows a comparison between the present and previous results. There is poor consistency between different groups. Although Goncharov et al. (2015) and Hsieh et al. (2018) used same experiment method (TDTR in DAC) and same composition single crystal (Fp_{10}), these measurement results provided quite different pressure dependence, especially above 20 GPa. For polycrystalline Fp_{20}, Manthilake et al. (2011) reported data obtained at only two different pressures, and its $d\lambda/dP$ shows a negative trend, which is unusual for minerals. Ohta et al. (2017) observed a reduction in a pressure range between 31 and 37 GPa and weaker pressure dependence above 37 GPa for Fp_{19}, which leads to much smaller λ values than other groups measured in DAC.

Our results for Fp_5 are fairly consistent with Manthilake et al. (2011), while our Fp_{20} has lower thermal conductivity values. Their negative pressure dependency of λ value of Fp_{20} may come from the measurement errors and very small pressure dependence of Fp_{20} thermal conductivity. Our Fp_{10} thermal conductivity values are in good agreement with Goncharov et al. (2015) and Hsieh et al. (2018) within the measured pressure range (< 15 GPa), whereas the $d\lambda/dP$ is only about one third of Hsieh et al. (2018).

In the previous studies, Hsieh et al. (2018) is the only group which discuss the Fe content influence on $d\lambda/dP$ of ferropericlase. They found lower $d\lambda/dP$ of Fp_{10} than Fp_8, which is consistent with the present results. However, $d\lambda/dP$ of Fp_{56} is larger than Fp_{10}, which is beyond our expectation. Although for Fp_{50} in this study, data were obtained only at low pressure (< 7 GPa),

which may be not enough to determine accurate $d\lambda/dP$, it is still robust that $d\lambda/dP$ for Fe-rich ferropericlase is very low. The present results demonstrate that λ of Fe-rich ferropericlase is very insensitive to pressure if we ignore the spin transition effect. One problem of the TDTR method is that the results critically depend on the thermal conductivity of the pressure transmitting medium, which is strongly pressure dependent (Goncharov et al., 2012; Tretiakov and Scandolo, 2004). Hence the TDTR method for samples with high and low λ may provide different accuracy for pressure dependence.

Overall, our results show that Fe concentration of ferropericlase has a more important effect on the pressure dependence and significantly alters the absolute thermal conductivity value.

2.4.2 Compositional dependence of thermal conductivity of ferropericlase

The room temperature thermal conductivity (λ) of ferropericlase $(Mg_{1-x}Fe_x)O$ with variable compositions (X_{Fe} = 0.03, 0.05, 0.10, 0.20, 0.30 and 0.50) at 1 bar can be derived from the pressure dependence fitting function (Table 2.1). Their λ values are valid for understanding the diversification of thermal conductivity of MgO-FeO binary system under ambient condition.

The present results at ambient condition can be represented by a model of thermal conductivity of substitution type solid solution (Padture and Klemens, 1997), in which:

$$\lambda = \lambda_i \left(\frac{\omega_0}{\omega_M}\right) \arctan\left(\frac{\omega_M}{\omega_0}\right) \tag{2.4}$$

while

$$\left(\frac{\omega_0}{\omega_M}\right)^2 = \frac{ZT}{C(1-C)}, \quad \lambda_i = C\lambda_A + (1-C)\lambda_B, \tag{2.5}$$

where ω_M is the phonon frequency corresponding to the maximum of the acoustic branch of the phonon spectrum, ω_0 is the phonon frequency where the intrinsic mean free path is equal to that due to solute atoms, Z is a constant, and C is the concentration of the solute atoms. λ_i is the solid-solution thermal conductivity without the solute-atom phonon scattering, λ_A and λ_B are thermal

conductivities with end compositions at a given temperature.

The thermal conductivity values of end members are referred from previous literature values (Touloukian et al., 1970; Akiyama et al., 1992). I obtained constant $Z = 2.29(2) \times 10^{-6}$, quite similar to the fitting result of Hasegawa et al. (2019) ($Z = 2.11(1) \times 10^{-6}$) using the same model. I also plot previous ambient condition measurement results in Fig. 2.5 (Akiyama et al., 1992; Goncharov et al., 2015; Hasegawa et al., 2019; Morton and Lewis, 1971; Ohta et al., 2017; Touloukian et al., 1970). All these data points are exactly on or near the fitting curve of this study, showing good agreements. Therefore, this well-fitted model is applicable for estimating the thermal conductivity value of ferropericlase of any composition under ambient conditions.

The λ value variation with Fe concentration of MgO-FeO solid solution (Fig. 2.5) has similar tendency with olivine (Zhang et al., 2019). However, the initial decrease of λ value in MgO-FeO system are much more dramatic than olivine system and the minimum value shifted to very high Fe content ($X_{Fe} \approx 0.92$). This suggests that in such oxide minerals with a simple cubic structure, the Fe effect is much larger for initial small addition and the effect of the phonon group velocities by replacement of larger atomic mass (Fe) are much more important than the symmetric configuration entropy influence.

2.4.3 Temperature dependence of thermal properties of ferropericlase

Fig. 2.6 and Fig. 2.7 shows λ and κ of ferropericlase aggregates with various X_{Fe} measured under high pressure as a function of temperature. The κ of all compositions (Fp_3, Fp_5, Fp_{10} and Fp_{20}) exhibits a monotonically decreasing tendency with increasing temperature, which is typical temperature dependence trend for thermal diffusivity of minerals. Pertermann and Hofmeister (2006) have inferred that based on the damped harmonic oscillator-phonon gas model (Debye et al., 1914) and spectroscopic and elastic measurements (Kolesov and Geiger, 2004), $\underline{\kappa}$ of minerals

can be represented by:

$$\kappa = A_0 + \frac{B_0}{T} + \frac{C_0}{T^2} + \cdots \tag{2.6}$$

where A_0, B_0 and C_0 are constant. Thermal diffusivity data of this study can be well fitted against temperature using Eq. (2.6) (see Fig. 2.8). Fitting results of all data are given in Table 2.2.

The variation of λ with temperature of all composition (Fp_3, Fp_5, Fp_{10} and Fp_{20}) shows a systematic tendency, first slightly increases with increasing temperature then starts to decrease at certain temperature (Fig. 2.6 and Fig 2.7). The maximum λ of each composition seems to shift to higher temperature with higher X_{Fe}, which provides a suggestion that such phenomena should be caused by Fe substitution. Compared with highly temperature-dependent λ of Fe-free end member MgO (Manthilake et al., 2011) and typical silicates such as olivine (Zhang et al., 2019), λ of Fe-bearing ferropericlase shows insensitivity to temperature change (Fig. 2.8). The sensitivity of λ to temperature variation and the absolute value of λ of different composition under each measured temperature decrease with increasing X_{Fe}, especially the initial addition of Fe to MgO results in the largest difference (endmember MgO and Fp_3).

Under measurement conditions of this study, heat carrier in ferropericlase can be considered in terms of phonons. To explain how the Fe substitution affects the temperature dependent λ of ferropericlase and leads to the unusual trend, here I consider a phonon propagating model (Broido et al., 2007), in which λ is given by:

$$\lambda = \frac{1}{\Omega}\sum_s \hbar\omega_s \frac{\partial N_s}{\partial T} v_s^2 \tau_s \tag{2.7}$$

where Ω is the volume of the sample, $\hbar\omega_s \frac{\partial N_s}{\partial T}$ is the heat capacity per mode, N_s is the Bose-Einstein distribution, T is temperature, v_s is the phonon group velocity and τ_s is the phonon transport lifetime along the applied temperature gradient. The phonon lifetime comes from the self-

consistent solution of the linearized form of the Boltzmann transport equation (BTE), commonly known as the full solution of the BTE. The initial condition for this iterative procedure is built from individual mode-dependent scattering rates including boundary scattering $1/\tau_s^b$, defect scattering $1/\tau_s^d$ and phonon scattering $1/\tau_s^{ph}$ using Matthiessen's rule (Ziman, 2001):

$$\frac{1}{\tau_s} = \frac{1}{\tau_s^b} + \frac{1}{\tau_s^d} + \frac{1}{\tau_s^{ph}} \tag{2.8}$$

In Eq. (2.7) and Eq. (2.8), temperature sensitive parameters are heat capacity and phonon scattering rate $1/\ \tau_s^{ph}$. For phonon transport of end member MgO case, the dominant scattering under room temperature is phonon-defect scattering while phonon-phonon scattering gradually becomes predominant with increasing temperature and the phonon-phonon scattering will saturated at a certain temperature, combining smaller influence of first increase then saturated heat capacity. I can find decreases of both λ values and $d\lambda/dT$ with increasing temperature. Once Fe substitutes in the solid solution system, the heavier Fe atoms will reduce the phonon group velocity v_s and increasing the phonon-defect scattering rating $1/\tau_s^d$ due to mass disorder and additional defect clustering brought by FeO (Catlow and Fender, 1975). From pure Mg system to initial Fe addition, such defect scattering change will have the largest effect, thus the λ values will apparently drop a lot after only small amount of Fe join (absolute value of MgO is ~5 times larger than Fp_3) and continuously decrease with increasing Fe concentration under room temperature. During temperature rising, considering defect clustering phenomena in $Fe_{1-x}O$ (Catlow and Fender, 1975) and tetrahedral occupancy of ferric iron in $(Mg_{1-x}Fe_x)O$ (Otsuka et al., 2010), large item $1/\tau_s^d$ makes the initial improvement of temperature dependent phonon-phonon scattering rate $1/\tau_s^{ph}$ not remarkable. At relatively low temperature the total change of phonon lifetime τ_s can be smaller than the increase of C_P. Consequently, λ will increase with increasing temperature in such temperature range. After temperature becomes enough high, more contribution of phonon-phonon

scattering makes reduction of phonon lifetime τ_s larger than heat capacity change. Then the λ value starts to decrease with increasing temperature. Higher X_{Fe} yields higher weight for phonon-defect scattering rate $1/\tau_s^d$, thus delays the appearance of temperature effect on phonon lifetime than heat capacity. The shift of the maximum λ value against temperature for different X_{Fe} and the decrease of temperature sensitivity of λ with increasing X_{Fe} can be explained by such mechanism. Especially for Fp_{20}, the defects scattering is so significant that both the increase and decrease of thermal conductivity with temperature are not conspicuous, making an almost constant λ value in the measurement temperature range.

Due to the significance of heat capacity change for λ variation with temperature, the measured λ values against temperature can be fitted by an empirical function, which usually represents the heat capacity change with temperature:

$$\lambda = A_1 T + B_1 T^{-2} + C_1 T^{-0.5} + D_1 \tag{2.9}$$

where A_1, B_1, C_1 and D_1 are the fitting constants and T is the temperature. The fitting curve and fitting parameters are shown in Fig. 2.8 and Table 2.2, respectively.

The behavior characterized by first increase and subsequent decrease in λ of ferropericlase with increasing temperature was also found in Manthilake et al. (2011), which is the only report of temperature dependence of ferropericlase data under high pressure. Although they use a literature estimate for C_P value to obtain λ from their measured κ value, their data obtained at 14 GPa show a similar trend. Their data obtained at 8 GPa do not show such unique tendency, which might be caused by not proper selection of heat capacity. I compared my data obtained at 9 GPa with their data obtained at 8 GPa in Fig. 2.9. Their Fp_5 data are in good agreement with ours while their Fp_{20} values are higher.

2.5 Geological implications

2.5.1 Thermal conductivity of ferropericlase under planetary mantle conditions

Knowledge of accurate λ values of main mantle phases is significant for understanding mantle dynamics and thermal history of planetary interior. To extrapolate the experimental results from limited laboratory conditions to various planetary mantle P, T conditions, we need to construct a universal equation to describe λ of ferropericlase with variable X_{Fe} under different P, T conditions.

Although λ of ferropericlase shows a unique tendency characterized by first increase then decrease from room temperature to high temperature, in hot planetary mantle, the increase part of λ up to ~500 K can be ignored. Therefore, I fit data obtained above 500 K by an empirical formula showing temperature dependence, which is expressed as:

$$\lambda_{P,T} = m\lambda_{P,295K}\left(\frac{295}{T}\right)^{N_{Fe}^{k}}, \tag{2.10}$$

where m is a constant with same value m = 1.245 for all fitting compositions, $\lambda_{P,295K}$ is the λ value under pressure P and 295 K, N_{Fe} is the Fe number (100 - #Mg) of ferropericlase and k is a fitting constant. The fitting values of k at different pressures are shown in Table 2.3. Fitting results reveal that k yields average values in the range of X_{Fe}, ~ –0.63 for Fe-poor composition ($X_{Fe} < 0.1$) and ~ –0.47 for Fe-rich composition ($X_{Fe} \geq 0.1$), respectively. If k = –0.5 is chosen for all compositions, the deviation of calculated λ values from measurement ones is less than 8%, while the deviation is estimated to be less than 5% using the average k values. Comparison between experimental and calculated values are presented in Fig. 2.10. For estimation of λ of mantle materials under variable mantle conditions, errors around 8% is within acceptable range, thus in a universal equation describing λ values of ferropericlase under mantle condition, k can set to be –0.5 for simplification.

$\lambda_{P,295K}$ can be calculated from a linear relationship against pressure P, expressed as $a_0P + a_1$. In Table 2.1, I show the values of constant pressure derivative a_0 and I found lna_0 has a linear relationship with the Fe number (100 - #Mg) of ferropericlase as shown in Fig. 2.11. a_1 equals to

the λ value at room temperature and 1bar, which has been described in Eq. (2.4) and Eq. (2.5) with constant $Z = 2.29(2) \times 10^{-6}$. After summarizing, the universal equation of λ of ferropericlase under mantle condition is given by:

$$\lambda_{P,T} = m\left\{e^{-(n_0 N_{Fe}+n_1)} \cdot P + \left[\left(C\lambda_{MgO} + (1-C)\lambda_{FeO}\right)\sqrt{\frac{ZT}{C(1-C)}} \cdot arctan\sqrt{\frac{C(1-C)}{ZT}}\right]\right\}\left(\frac{295}{T}\right)^{N_{Fe}^{k}}. \qquad (2.11)$$

where m, n_0, n_1, Z, and k are constant (Table 2.4), C is the solute atom Mg concentration (= 1-N_{Fe}/100), N_{Fe} is the Fe number of ferropericlase, T is the temperature, λ_{MgO} and λ_{FeO} are λ values of MgO and FeO at room temperature and 1 bar (e.g., Touloukian 1970; Akiyama et al., 1992).

This universal equation can be a straightforward tool for numerical modelling works of dynamics and thermal evolution of the planetary interior. I calculated the thermal conductivity of ferropericlase with different X_{Fe} using Eq. (2.11), based on adiabatic temperature profile in the Earth's mantle proposed by Katsura et al. (2010). Fig. 2.12 shows depth profiles of λ calculated using different k values. The solid lines represent the λ variation with constant k value, –0.5, while the dashed lines yield more specific results from k values suitable for each X_{Fe}, -0.63 (for $X_{Fe} < 0.1$) and -0.47 (for $X_{Fe} \geq 0.1$). For Fp_3 and Fp_{10}, λ values increase by a factor of three through the whole mantle, while λ depth profile for Fp_{30} shows only a slight increase ~1.3 W $m^{-1}K^{-1}$. At the base of the mantle, λ of Fp_3 are much larger than that of Fp_{30} by a factor of 5. If we only consider the Fe induced pressure dependence, a difference of the λ values between these two compositions would reach 10 times, thus the Fe content dependent temperature response of λ of ferropericlase somewhat reduce the gap between Fe-poor and -rich compositions. However, since the pressure response of λ is very large compared to the temperature dependence, ferropericlae has remarkably different thermal properties between low and high Fe compositions in the deeper mantle: the former can be regarded as thermal conductor while the latter behaves like a thermal insulator in the deep part of the mantle.

The point to note here is that I ignore the influence of Fe spin transition in our universal equation, which has been found by DAC methods (Ohta et al., 2017 and Hsieh et al., 2018). Hsieh et al. (2018) found little decrease of λ induced by spin transition for Fp_8 and Fp_{10}, indicating that the additional scattering caused by spin transition may not be significant for Fe-poor composition, at least such influence cannot be identified within the TDTR method measurement accuracy. On the contrast, for Fe-rich composition like Fp_{56}, spin transition leads to ~17% decrease of the λ value under lowermost mantle pressure condition and room temperature. Since the spin transition pressure range becomes wider with increasing temperature (Lin and Tsuchiya, 2008), such decrease of λ can be smaller at high temperatures corresponding to the lower mantle. Therefore, I conclude that the effect of the spin transition on λ of ferropericlase in the mantle would not largely change our estimated values from the universal equation. Moreover, the spin transition can affect more apparently for Fe-rich ferropericlase and further decrease their thermal conductivity value, which can even enlarge the difference of the heat transport ability between Fe-poor and -rich ferropericlase in the deep mantle of the Earth. The influence of spin transition will not change the main conclusion of this study.

2.5.2 Application to mantle dynamics and evolution

Ferropericlase with the large variations of thermal conductivity under different conditions can play a unique role in controlling the cooling of Earth's magma ocean (MO). λ of ferropericlase highly depends on Fe concentration, end member MgO and Fe-poor ferropericlase ($X_{Fe} < 0.1$) are good thermal conductor while ferropericlase with extremely Fe-rich composition ($X_{Fe} \geq 0.3$) can act as a thermal insulator under the whole mantle condition. Thus, the crystallization sequence and depth at which solidification starts will be important for the heat loss in the early Earth.

The MO crystallization history can be affected by multiple factors and many possible scenarios

have been described by previous studies (e.g., Labrosse et al., 2007; Boukaré et al., 2015; Trønnes et al. 2019). During the crystallization of MO, as Fe preferentially partitions into melt, initially crystallized solids will experience significant depletion of Fe near endmember case (Boukaré et al., 2015). In the pyrolitic mantle, ferropericlase becomes the first liquidus phase, until being replaced by bridgmanite above 31 GPa (Ito et al., 2004). As the density of Mg-rich ferropericlase is comparable to the peridotite liquid density at 20~25 GPa (Suzuki & Ohtani, 2003), if ferropericlase first crystallized in the early stage and the convection of the MO is slow, Fe-depleted ferropericlase grains may form a thin layer at this depth. Such Fe-poor ferropericlase layer has several times higher thermal conductivity than other candidate silicates and cannot efficiently prevent the heat loss of the deeper melt layer. Heat conduction through such a floating layer will be remarkably high. The direct contact part of underlying MO may quickly solidify while the overlying MO still suffered from remarkable heat flux.

In the late stage of the solidification of MO, long-lived FeO-enriched basal magma ocean (BMO) has been proposed (e.g., Labrosse et al., 2007). As Fe preferentially partitions into ferropericlase (Irifune et al., 2010), Fe-rich ferropericlase with high density can sink in the MO. If such Fe-rich ferropericlase were not dispersed by later vigorous solid mantle convection and stably accumulated at the base of the solid mantle, they can maintain some hotter and denser regions due to the low thermal conductivity value for geological time scale. For example, our model predicts a λ value of Fp_{30} about 4.2 $Wm^{-1}K^{-1}$ at the lowermost mantle while Fp_{50} has even smaller value about 2.3 $Wm^{-1}K^{-1}$. Previous studies have estimated high λ values of the lowermost mantle from 8.0 to 12.8 $Wm^{-1}K^{-1}$ (Manthilake et al., 2011; Ohta et al., 2017; Hsieh et al., 2018), which are larger than our Fp_{30} value by a factor of 2–3 and larger than Fp_{50} by a factor of 4–6. Fe-rich ferropericlase also has very low sound velocities (Wicks et al., 2010). Hot dense pockets with low thermal conductivity

match features of seismologically observed ULVZs well, which are composed of chemically denser materials (e.g., iron-rich) and would be favorably sited along the edges of hotter LLSVPs (Li et al. 2017; Zhao et al., 2017). Therefore, Fe-rich ferropericlase accumulates can be one possible origin for the ULVZs, which suppress heat flux from underlying core compared with the surrounding mantle.

The Fe-dependent λ of ferropericlase might also has a unique importance for understanding the cooling of MO and core of Venus, Mars, and other terrestrial exoplanets. The initial composition and temperature of the MO coupled with the atmospheric conditions will control the solidification sequence and density contrast between melts and crystallized grains, determining whether a floating Fe-depleted good thermal conducting layer or a dense Fe-rich thermal insulating layer of ferropericlase will form or not, which would accelerate or delay the furthering cooling of magma ocean and the core. Zeff and Williams (2019) examined fractional crystallization of the Martian MO and predicted the formation of a thermochemical boundary layer (TCBL) at the base of the mantle, which may consist of iron-rich ferropericlase and garnet. In this case, more Fe-rich ferropericlase in the Martian mantle with lower λ value rather than at CMB of the Earth can suppress heat flux from the core. A liquid Martian core without vigorous dynamo can maintain without formation of solid inner core. For Venus, the sister planet of the Earth, O'Rourke (2020) claimed that a thick basal magma ocean may still exist today. Whether an Fe-rich ferropericlase layer overlying on the core exists or whether similar ULVZs are forming at the base of the MO of Venus are interesting issues for understanding the past of Earth's thermal evolution and the role of ferropericlase during the cooling of the MO of a terrestrial planet.

2.6 Conclusion

The major conclusions of this work are as follows:

i. Thermal conductivity of ferropericlase is largely varied by different Fe contents. The estimated thermal conductivity values of Fp_3, Fp_5, Fp_{10}, Fp_{20}, Fp_{30} and Fp_{50} under ambient condition (1bar, 300 K) are smaller than MgO periclase by a factor of ~5, 6, 9, 16, 18, and 23, respectively.

ii. The pressure response of λ of ferropericlase strongly depends on Fe content. The pressure effect decreases with increasing Fe content. Fe-poor composition has a pressure dependence 10 times larger than Fe-rich composition.

iii. Thermal conductivity of ferropericlase is not sensitive to temperature variation compared with silicates. Ferropericlase aggregates with all measured compositions show a unified tendency characterized by a first increase then decrease against temperature and the maximum value shifts at higher temperature for higher Fe content composition.

iv. Thermal conductivity of ferropericlase can be described by a universal equation, which can allow us predicting thermal conductivity of ferropericlase with any composition under mantle conditions.

v. The Fe-rich ferropericlase with low λ can explain one possible origin of ULVZs. Due to highly composition dependent λ of ferropericlase, the crystallization sequence and depth of ferropericlase can also influence the magma ocean cooling of terrestrial planets. Thus, when modelling the solidification of magma ocean, largely variable composition-, pressure- and temperature dependent λ of ferropericlase should be considered.

Reference

Akiyama, T., Ohta, H., Takahashi, R., Waseda, Y., Yagi, J. (1992). Measurement and modeling of thermal conductivity for dense iron oxide and porous iron ore agglomerates in stepwise reduction. ISIJ Int., 32, pp. 829-837.

Boukaré, C., Ricard, Y., Fiquet, G. (2015). Thermodynamics of the MgO–FeO–SiO2 system up to 140 GPa: application to the crystallization of Earth's magma ocean. J. Geophys. Res. Solid Earth 120, 6085–6101.

Broido, D. A., Malorny, M., Birner, G., Mingo, N., Stewart, D. A. (2007). Intrinsic lattice thermal conductivity of semiconductors from first principles. Appl. Phys. Lett. 91, 231922.

Catlow, C. R. A. and Fender, B. E. F. (1975). J. Phys. C: Solid State Phys. 8 3267.

Dalton, D.A., Hsieh, W.-P., Hohensee, G.T., Cahill, D.G., Goncharov, A.F. (2013). Effect of mass disorder on the lattice thermal conductivity of MgO periclase under pressure. Sci. Rep., 3, p. 2400.

Debye, P. (1914). Vorträge über die kinetische Theorie der Materie und der Elektrizität. B.G. Teuber, Berlin.

Goncharov, A.F., Wong, M.L., Dalton, D.A., Ojwang, J., Struzhkin, V., Konopkova, Z., Lazor, P. (2012). Thermal conductivity of argon at high pressures and high temperatures. J. Appl. Phys., 111, p. 112609.

Goncharov, A., Lobanov, S., Tan, X., Hohensee, G., Cahill, D., Lin, J.-F., Thomas, S.-M., Okuchi, T., Tomioka N. (2015). Experimental study of thermal conductivity at high pressures: Implications for the deep Earth's interior. Phys. Earth Planet. Inter., 247, pp. 11-16.

Hasegawa, A., Ohta, K., Yagi, T., Hirose, K., Okuda, Y., Kondo, T. (2019). Composition and pressure dependence of lattice thermal conductivity of (Mg,Fe)O solid solutions. C. R. Géosci., 351, pp. 229-235.

Hsieh, W.-P., Deschamps, F., Okuchi, T., Lin, J. F. (2018). Effects of iron on the lattice thermal conductivity of Earth's deep mantle and implications for mantle dynamics. Proceedings of the National Academy of Sciences, 115(16), 4099–4104.

Imada, S., Ohta, K., Yagi, T., Hirose, K., Yoshida, H., Nagahara, H. (2014). Measurements of lattice thermal conductivity of MgO to core–mantle boundary pressures. Geophys. Res. Lett., 41, pp. 4542-4547.

Irifune, T., Shinmei, T., McCammon, C.A., Miyajima, N., Rubie, D.C., Frost, D.J. (2010). Iron partitioning and density changes of pyrolite in Earth's lower mantle. Science, 327, pp. 193-195.

Ito, E., Kubo, A., Katsura, T., Walter, M.J. (2004). Melting experiments of mantle materials under lower mantle conditions with implications for magma ocean differentiation. Phys. Earth Planet. Inter., 143–144, pp. 397-406.

Katsura, T., Yoneda, A., Yamazaki, D., Yoshino, T., Ito, E. (2010). Adiabatic temperature profile in the mantle. Phys. Earth Planet. Inter., 183, pp. 212-218.

Kolesov, B.A., Geiger, C.A. (2004). A temperature-dependent single-crystal Raman spectroscopic study of fayalite: evidence for phonon-magnetic excitation coupling. Physics and Chemistry of Minerals, 31, 155–161.

Labrosse, S., Hernlund, J., Coltice N. (2007). A crystallizing dense magma ocean at the base of the Earth's mantle. Nature, 450(7171), 866–869.

Lin, J-F., Speziale, S., Mao, Z., Marquardt, H. (2013). Effects of the electronic spin transitions of iron in lower mantle minerals: Implications for deep mantle geophysics and geochemistry. Rev Geophys 51:244–275.

Lin, J. F., Tsuchiya. T. (2008). Spin transition of iron in the Earth's lower mantle, Phys. Earth Planet. Inter., 170, 248–259.

Li, M., McNamara, A.K., Garnero, E.J., Yu, S. (2017). Compositionally-distinct ultra-low velocity zones on Earth's core-mantle boundary. Nat Commun 8:177.

Manthilake, G.M., de Koker, N., Frost, D.J., McCammon, C.A. (2011). Lattice thermal conductivity of lower mantle minerals and heat flux from Earth's core. Proc. Natl. Acad. Sci. USA, 108, pp. 17901-17904.

Morton, I.P., Lewis, M.F. (1971). Effect of iron impurities on the thermal conductivity of magnesium oxide single crystals below room temperature. Phys. Rev. B, 3, pp. 552-559.

Ohta, K., Yagi, T., Hirose, K., Ohishi, Y. (2017). Thermal conductivity of ferropericlase in the Earth's lower mantle. Earth Planet Sci Lett 465:29–37.

O'Rourke, J. G. (2020). Venus: a thick basal magma ocean may exist today. Geophysical Research Letters, 47(4), ISSN 19448007. doi: 10.1029/2019GL086126.

Osako, M., Ito, E., Yoneda, A. (2004). Simultaneous measurements of thermal conductivity and thermal diffusivity for garnet and olivine under high pressure. Phys. Earth Planet. Inter. 143–144, 311-320.

Otsuka, K., McCammon, C.A., Karato, S. (2010). Tetrahedral occupancy of ferric iron in (Mg, Fe)O: implications for point defects in the Earth's lower mantle. Phys. Earth Plan. Int., 180 (2010), pp. 179-188.

Padture, N., Klemens, P. (1997). Low thermal conductivity in garnets. J. Am. Ceram. Soc., 80, pp. 1018-1020.

Pertermann, M., Hofmeister, A.M. (2006). Thermal diffusivity of olivine-group minerals. Am. Mineral 91, 1747–1760.

Sinmyo, R., Hirose, K. (2013). Iron partitioning in pyrolitic lower mantle. Phys. Chem. Miner., 40, pp. 107-113, 10.1007/s00269-012-0551-7.

Smith, D., Fayette, S., Grandjean, S., Martin, C., Telle, R., Tonnessen, T. (2003). Thermal resistance of grain boundaries in alumina ceramics and refractories. J. Am. Ceram. Soc., 86, pp. 105-111.

Suzuki, A., Ohtani, E. (2003). Density of peridotite melts at high pressure. Phys. Chem. Miner. 30, 449–456.

Thorne, M.S., Garnero, E.J. (2004). Inferences on ultralow-velocity zone structure from a global analysis of SPdKS waves. J Geophys Res B Solid Earth 109:1–22.

Touloukian, Y.S., Powell, R.W., Ho, C.Y., Klemens, P.G. (1970). Thermal conductivity nonmetallic solids. Thermophysical Properties of Matter, vol. 2, Thermophys. Prop. Res. Cent., New York.

Tretiakov, K.V., Scandolo, S. (2004). Thermal conductivity of solid argon at high pressure and high temperature: a molecular dynamics study. J. Chem. Phys., 121, pp. 11177-11182.

Trønnes, R. G., Baron, M. A., Eigenmann, K. R., Guren, M. G., Heyn, B. H., Løken, A., Mohn, C. E. (2019). Core formation, mantle differentiation and core-mantle interaction within Earth and the terrestrial planets. Tectonophysics, 760, 165–198.

Wicks, J.K., Jackson, J.M., Sturhahn, W. (2010). Very low sound velocities in iron-rich (Mg,Fe)O: Implications for the core-mantle boundary region. Geophys Res Lett 37: L15304.

Yoshino, T., Ito, E., Katsura, T., Yamazaki, D., Shan, S., Guo, X., Nishi, M., Higo, Y., Funakoshi K. (2011). Effect of iron content on electrical conductivity of ferro-periclase with implications for the spin transition pressure. J. Geophys. Res., 116, B04202.

Zeff, G., Williams, Q. (2019). Fractional crystallization of martian magma oceans and formation of a thermochemical boundary layer at the base of the mantle. Geophys Res Lett 46 (20): 10997-11007.

Zhang, Y., Yoshino, T., Yoneda, A., Osako, M. (2019). Effect of iron content on thermal conductivity of olivine with implications for cooling history of rocky planets. Earth and Planetary Science Letters, 519, 109–119.

Zhao, C., Garnero, E. J., Li, M., McNamara, A., Yu, S. (2017). Intermittent and lateral varying ULVZ structure at the northeastern margin of the Pacific LLSVP. J. Geophys. Res. 122, 1198–1220.

Ziman, J. M. (2001). Electrons and Phonons: The Theory of Transport Phenomena in Solids. Clarendon Press, Oxford.

Tables

Table 2.1 Fitting parameters of thermal conductivity λ and thermal diffusivity κ

Composition	$\lambda = a_0P + a_1$		$\kappa = b_0P + b_1$	
	a_0 (GPa^{-1})	a_1 ($Wm^{-1}K^{-1}$)	b_0 (GPa^{-1})	b_1 ($10^{-6}m^2s^{-1}$)
Fp_3	0.278	11.439	0.066	3.690
Fp_5	0.223	8.873	0.034	2.172
Fp_{10}	0.121	6.318	0.009	1.722
Fp_{20}	0.046	3.487	0.007	1.055
Fp_{30}	0.013	3.007	0.003	0.818
Fp_{50}	0.028	2.316	0.003	0.507

Table 2.2 Fitting parameters of thermal conductivity λ and thermal diffusivity κ

Compositions	**P(GPa)**	$\lambda = A_1T + B_1T^{-2} + C_1T^{-0.5} + D_1$			
		A_1	B_1	C_1	D_1
Fp_{10}	6	-0.00859	89242.143	-187.986	19.459
Fp_{20}	6	0.00177	-184962.341	121.920	-1.684
Fp_3	9	0.00000125	-799117.410	519.628	-6.901
Fp_5	9	-0.00439	-201679.559	62.898	27.956
Fp_{10}	9	-0.00284	-328938.214	117.055	5.217
Fp_{20}	9	0.000842	-129194.333	69.924	0.983
Fp_3	12	-0.00677	-510667.305	230.024	9.240
Fp_5	12	-0.00775	-346107.134	27.224	15.956
Fp_{10}	12	0.00413	-751412.913	450.723	-10.983
Fp_{20}	12	0.00101	-171884.365	100.843	-0.117
Fp_3	15	-0.00972	-481693.632	165.154	14.554
Fp_{10}	15	-0.00341	-199964.807	49.399	8.466
Fp_{20}	15	0.00224	-248978.600	156.942	-2.790
Fp_3	18	0.00665	-1132850.000	807.707	-19.636
Fp_5	18	-0.00704	-332061.247	61.324	15.277
Fp_3	21	0.00320	-1428890.000	860.179	-18.426
Fp_3	23	0.00423	-1495170.000	918.805	-21.011
Compositions	**P(GPa)**	$\kappa = A_0 + B_0T^{-1} + C_0T^{-2}$			
		A_0	B_0	C_0	
Fp_{10}	6	0.689	583.073	-74616.940	
Fp_{20}	6	1.006	-9.209	11674.354	
Fp_3	9	0.646	1656.715	-168899.162	
Fp_5	9	0.796	777.299	-78299.011	
Fp_{10}	9	0.746	594.901	-84628.382	
Fp_{20}	9	1.042	-30.594	15437.571	
Fp_3	12	0.850	1698.441	-185738.296	
Fp_5	12	0.730	905.043	-109088.687	
Fp_{10}	12	1.001	410.226	-49122.098	
Fp_{20}	12	1.005	4.788	9434.674	
Fp_3	15	1.0438	1688.649	-179775.375	
Fp_{10}	15	0.898	531.064	-74735.502	
Fp_{20}	15	1.064	-20.774	14273.844	
Fp_3	18	1.443	1294.021	-86384.776	
Fp_5	18	1.060	714.643	-60880.824	
Fp_3	21	0.855	1854.094	-199464.405	
Fp_3	23	1.546	1289.715	-90492.361	

Table 2.3 Fitting parameters of *k* under different pressure for each composition

$\lambda_{P,T} = m\lambda_{P,295K}(295/T)^{(N_{Fe}^k)}$				
P(GPa)	k (Fp_3)	k (Fp_5)	k (Fp_{10})	k (Fp_{20})
6			-0.43818	-0.44601
9	-0.54949	-0.58407	-0.47252	-0.51004
12	-0.63568	-0.65600	-0.49011	-0.44262
15	-0.67362	-0.63246	-0.45671	-0.50051
18	-0.59684			
21	-0.63617			
23	-0.70253			
average	-0.63239	-0.62418	-0.46438	-0.47480

Table 2.4 Constant parameter values of universal equation for thermal conductivity λ of ferropericlase

	m	n_0	n_1	Z	k	λ_{MgO} (Touloukian 1970)	λ_{FeO} (Akiyama et al., 1992)
value	1.245	0.1117	0.9447	2.292×10^{-6}	-0.5	55.2	5.44

Figures

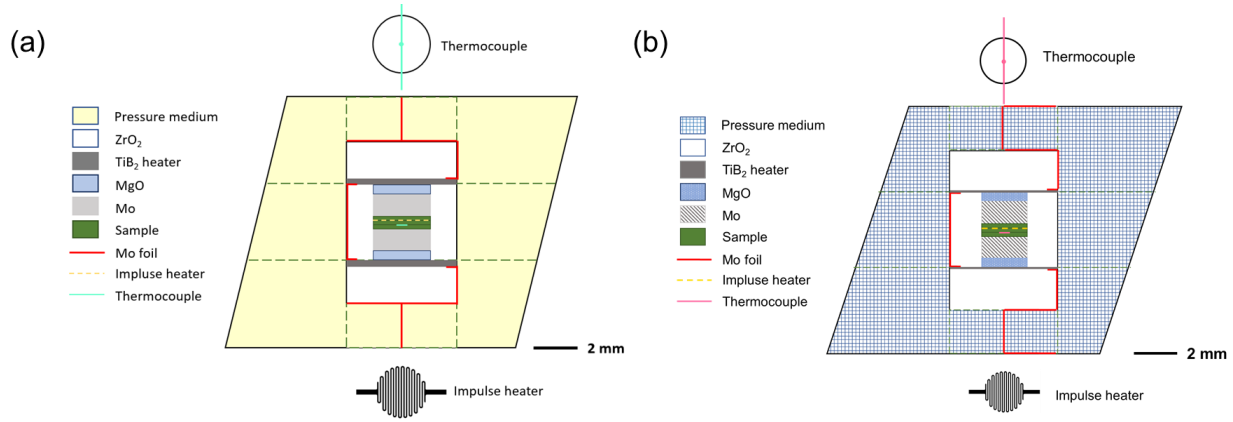

Fig. 2.1 Cell design for pulse heating method. (a) 14/8 cell for Fp_{10}, Fp_{20}, Fp_{30} and Fp_{50} thermal conductivity measurement. (b) 14/6 cell for Fp_3 and Fp_5, which allows higher pressure generation up to 23 GPa.

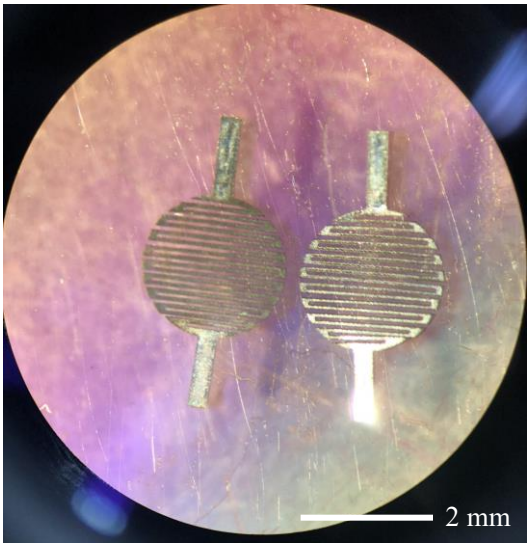

Fig. 2.2 Self-made Re impulse heater with 17 pinches.

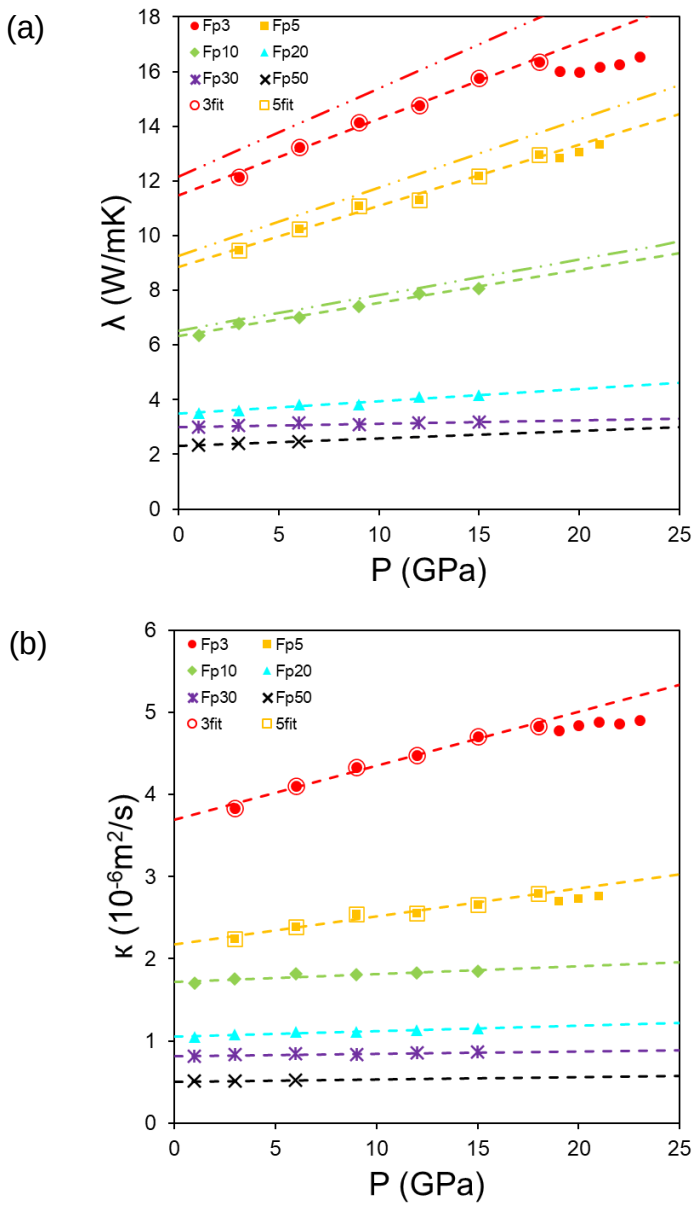

Fig. 2.3 (a) Pressure dependence of thermal conductivity λ of ferropericlase: fitting results of measurement values are shown in dashed lines; fitting results of calculated single crystal values are shown dashed-dot-dot lines. (b) Pressure dependence of thermal diffusivity κ of ferropericlase: fitting results are shown in dashed lines. Errors of λ (ca. 3%) and κ (ca. 2%) are summation of the uncertainties derived from heating area S, pulse heating power W, sample thickness d and the fitting errors of A and B.

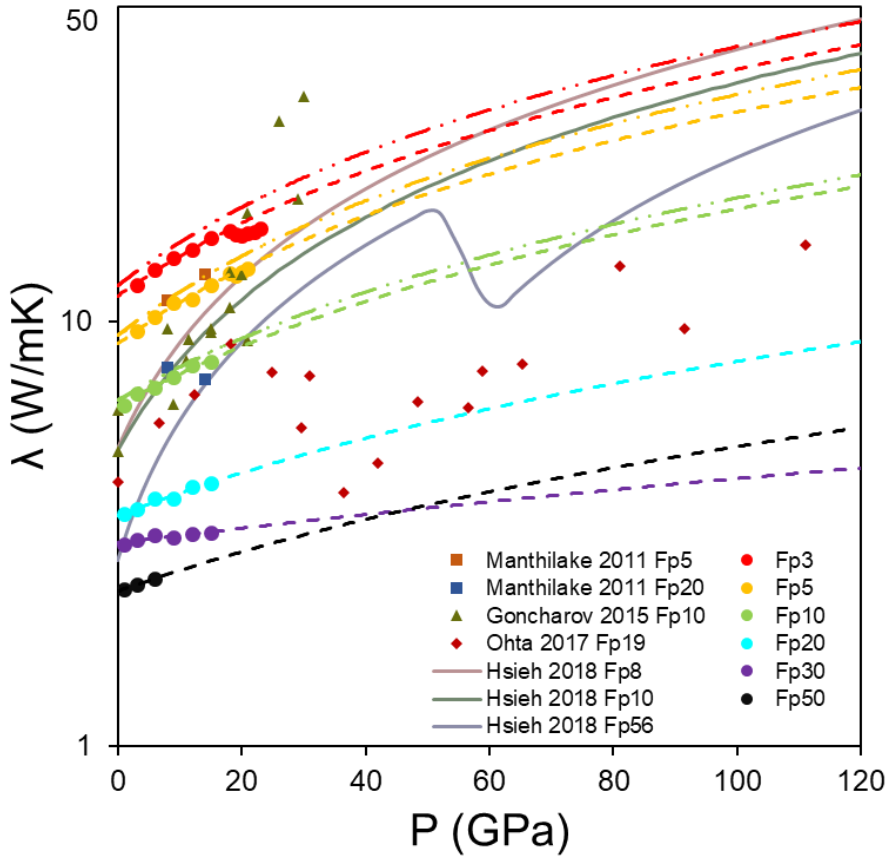

Fig. 2.4 Comparison of thermal conductivity λ of ferropericlase obtained from the present study as a function of pressure with previous results (Mantilake et al., 2011; Goncharov et al., 2015; Ohta et al., 2017; Hsieh et al., 2018).

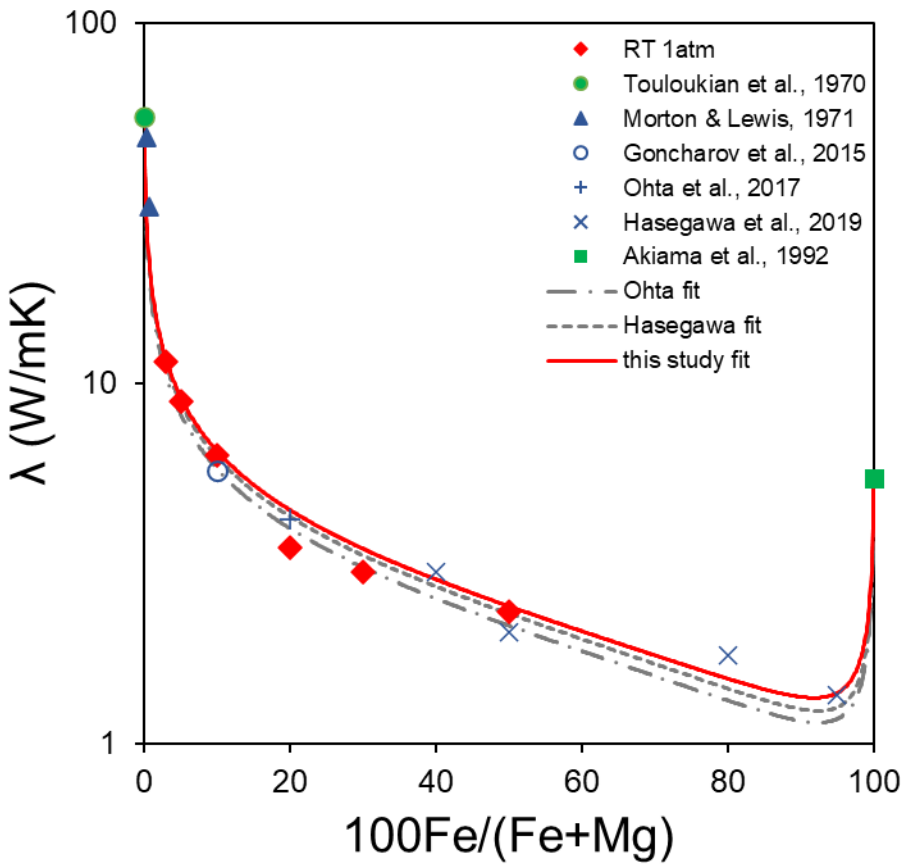

Fig. 2.5 Compositional dependence of thermal conductivity λ under room temperature at 1 bar. Dashed-dot and dashed lines represent fitting results from Ohta et al. (2017) and Hasegawa et al. (2019), respectively.

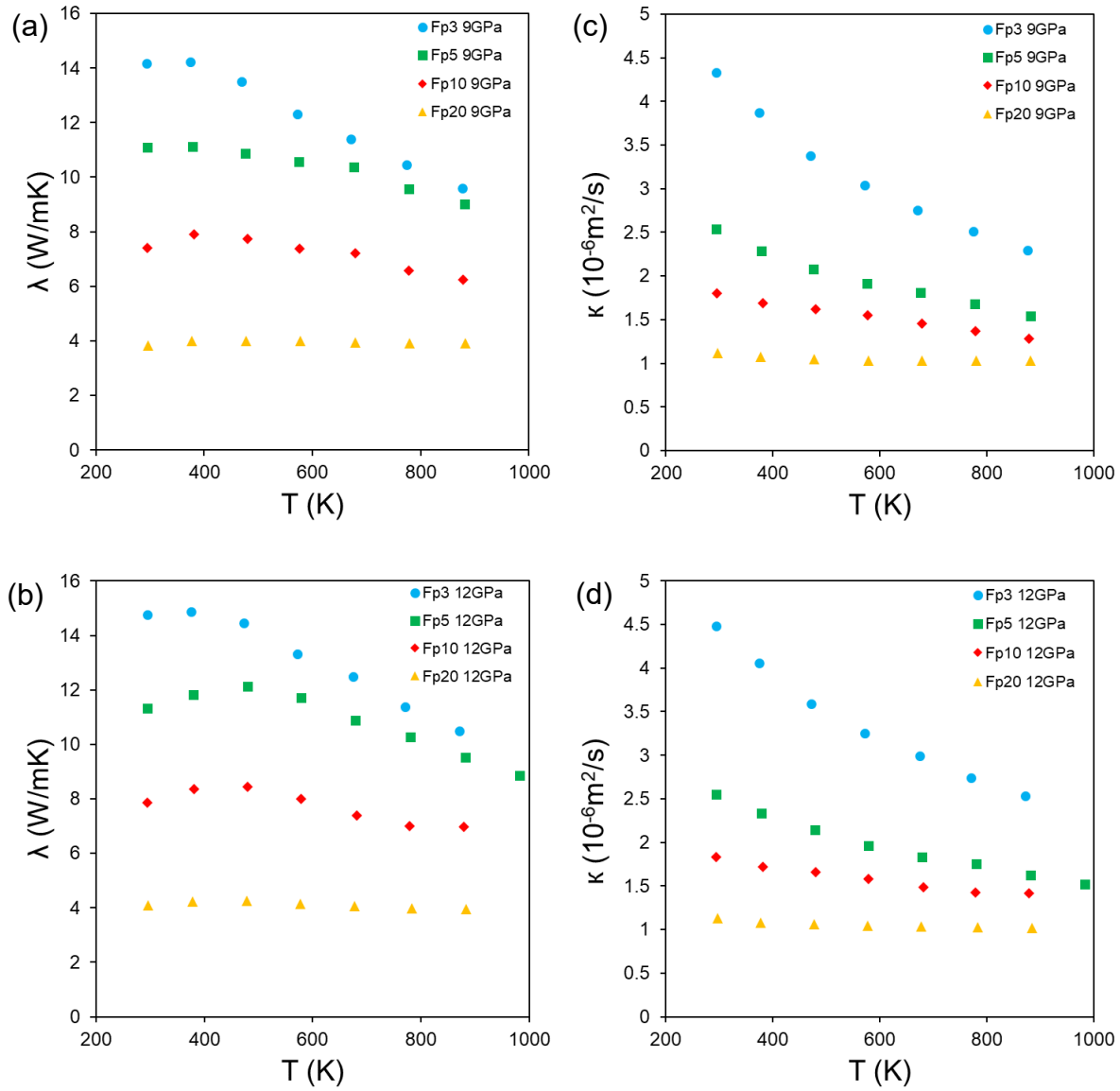

Fig. 2.6 Temperature dependence of thermal conductivity λ of ferropericlase with different Fe contents at pressures of (a) 9 GPa and (b) 12 GPa. Temperature dependence of thermal diffusivity κ of ferropericlase with different Fe contents at pressures of (c) 9 GPa and (d) 12 GPa.

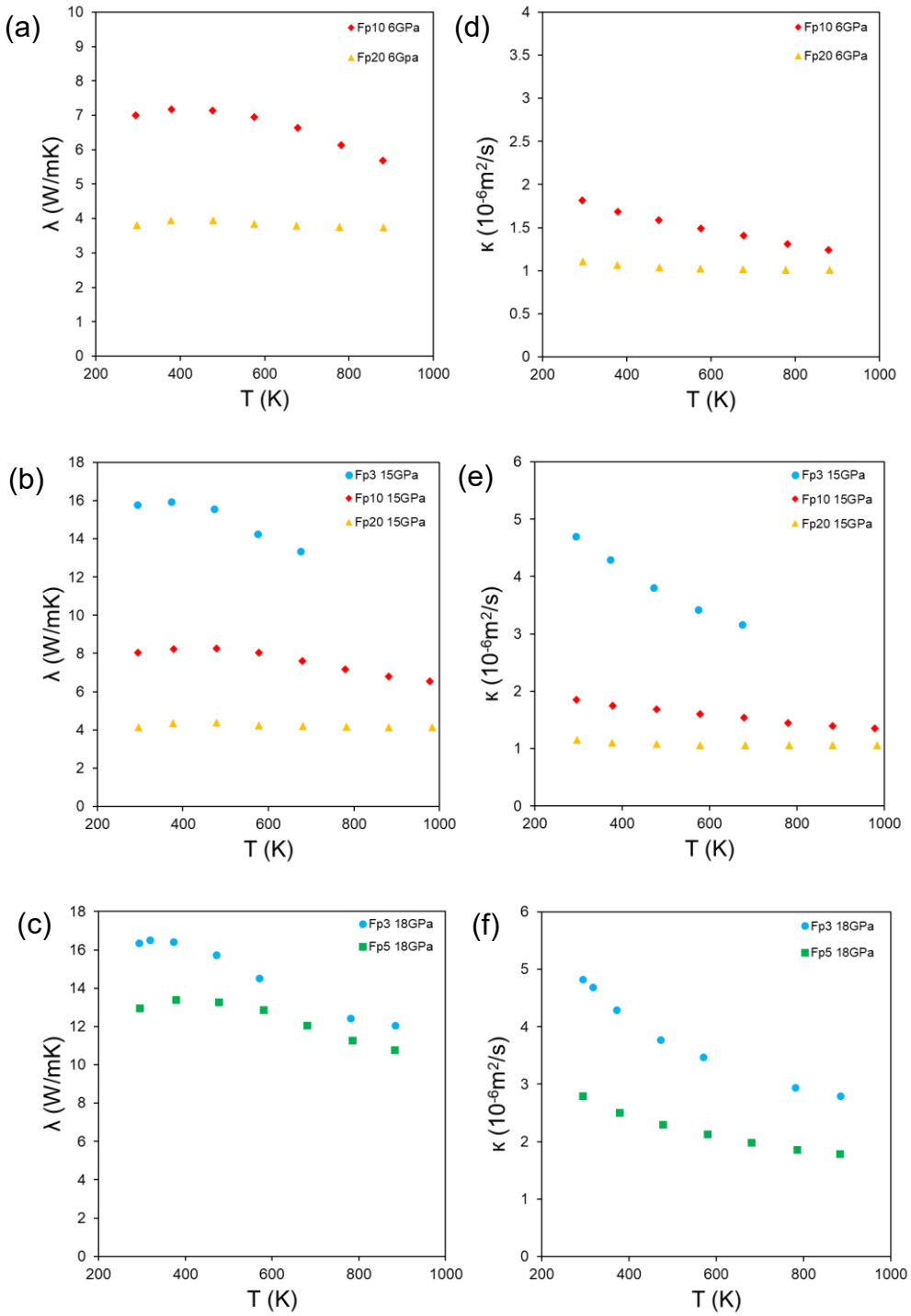

Fig. 2.7 Temperature dependence of thermal conductivity λ of ferropericlase with different Fe contents at pressures of (a) 6 GPa, (b) 15 GPa and (c) 18 GPa. Temperature dependence of thermal diffusivity κ of ferropericlase with different Fe contents at pressures of (d) 6 GPa, (e) 15 GPa and (f) 18 GPa.

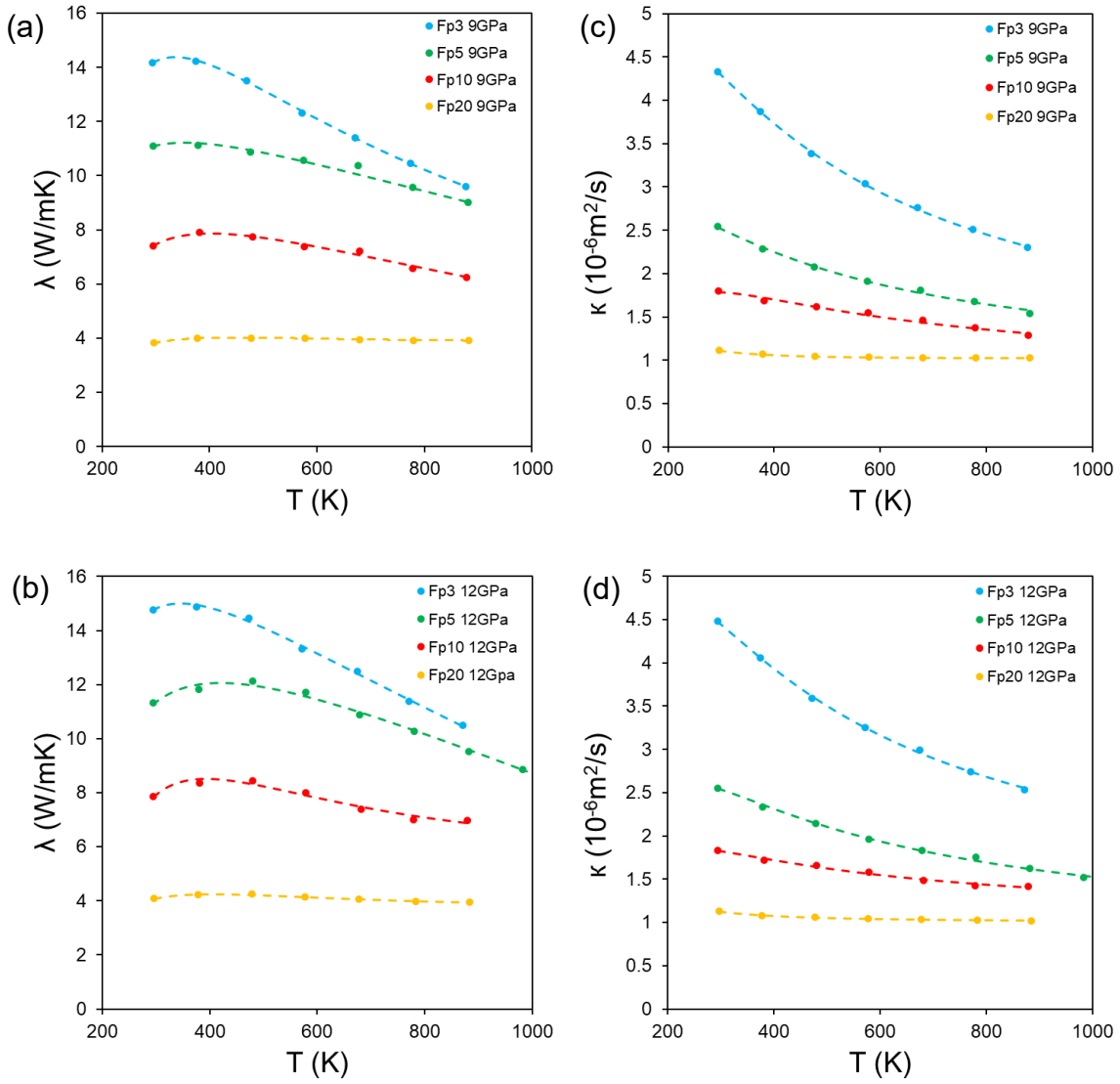

Fig. 2.8 Fitting curve of temperature dependence of thermal conductivity λ of ferropericlase with different Fe contents at pressures of (a) 9 GPa and (b) 12 GPa. Fitting curve of temperature dependence of thermal diffusivity κ of ferropericlase with different Fe contents at pressures of (c) 9 GPa and (d) 12 GPa.

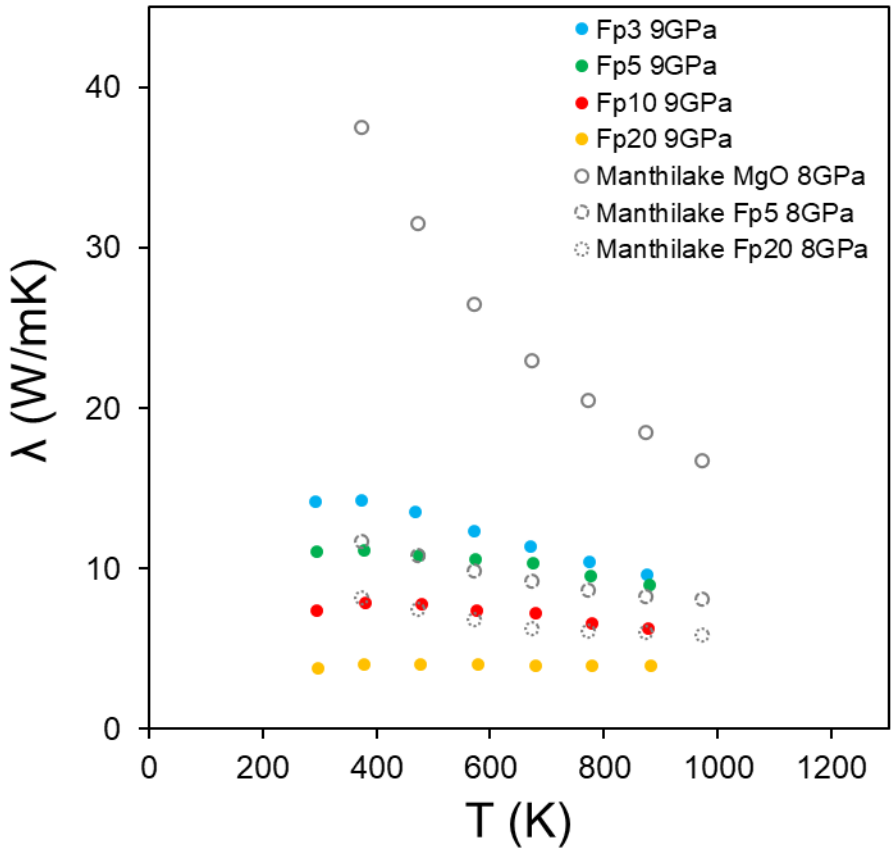

Fig. 2.9 Comparison of temperature dependence of thermal conductivity λ of ferropericlase with previous results by Manthilake et al. (2011).

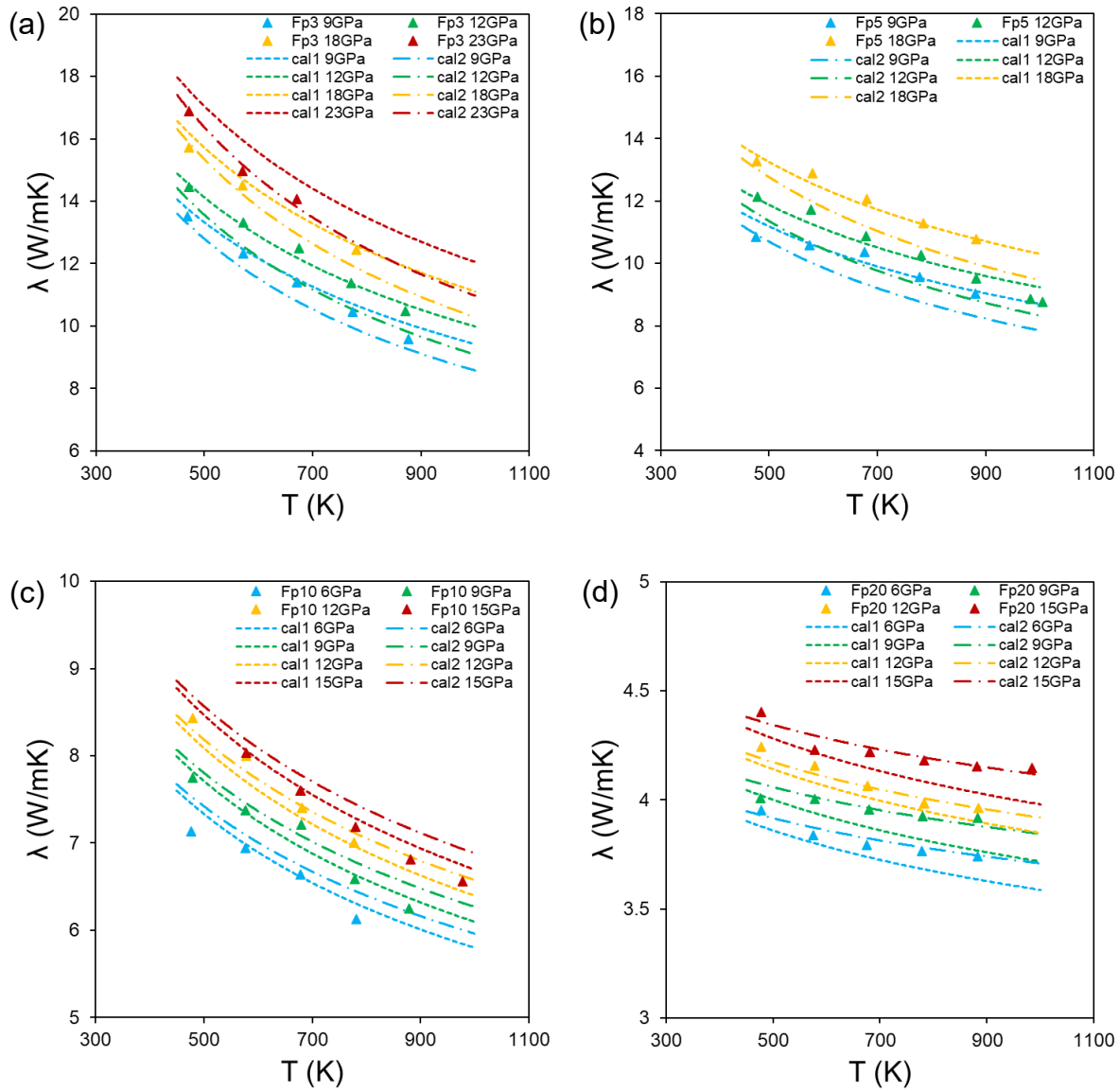

Fig. 2.10 Comparison of experimental results and calculated values from equation $\lambda_{P,T} = m\lambda_{P,295K}(295/T)^{(N_{Fe}^{k})}$: $k = -0.63$ (Fp_3 and Fp_5) or -0.47 (Fp_{10} and Fp_{20}) for dashed line and $k = -0.5$ for dashed-dot line.

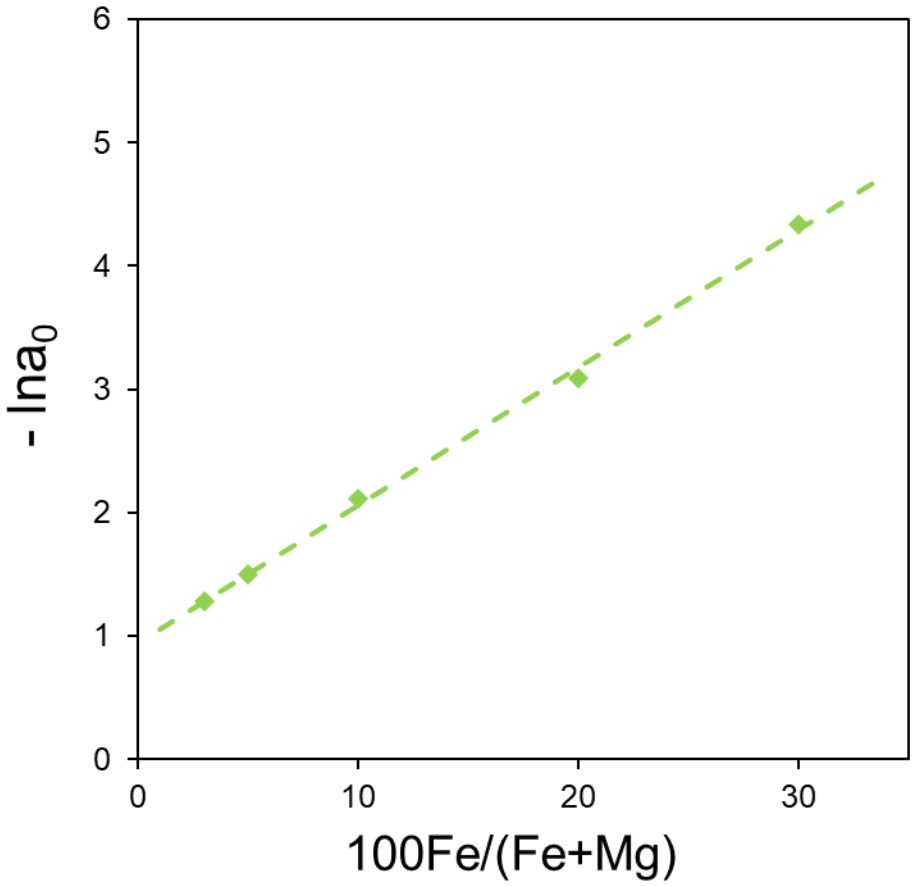

Fig. 2.11 Linear relationship between lna_0 and Fe number of ferropericlase.

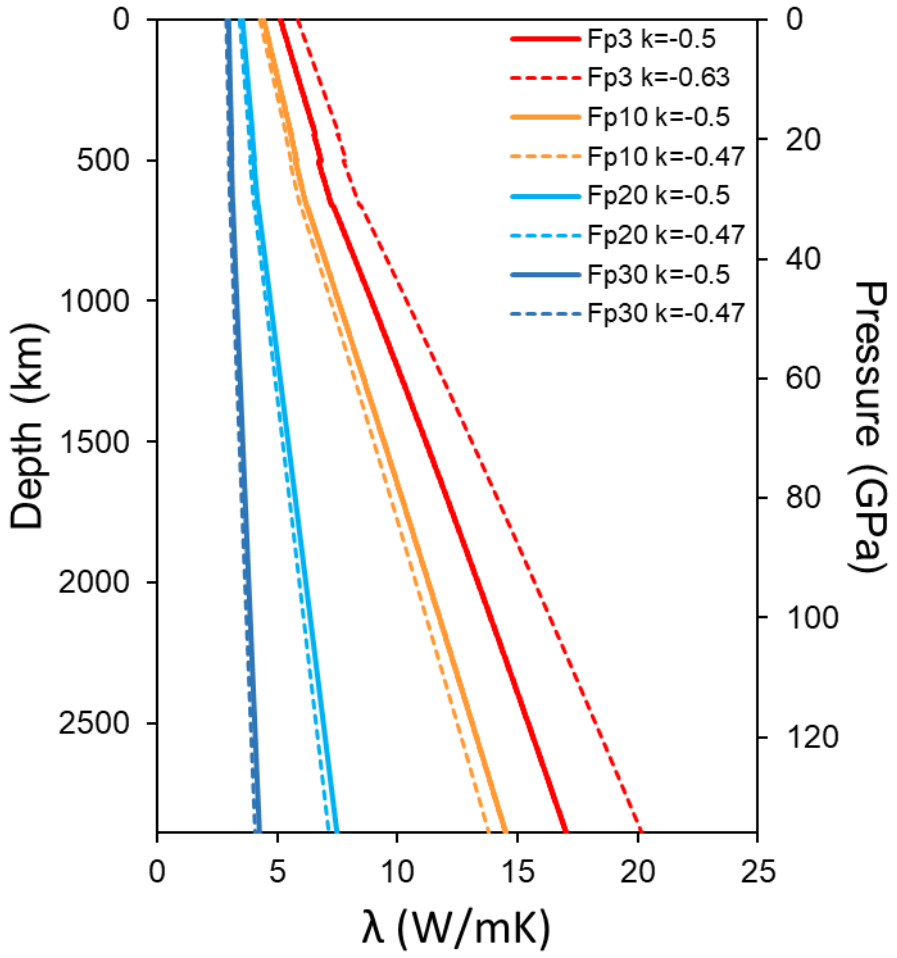

Fig. 2.12 Thermal conductivity of ferropericlase with different Fe contents along geotherm.

Part 3. Simultaneous measurements of thermal conductivity and thermal diffusivity of bridgmanite and post-spinel: implications for planetary mantle dynamics and evolution

3.1 Abstract:

Aluminium (Al)-, iron (Fe)-bearing bridgmanite is thought to be the dominant phase in the Earth's lower mantle. Its thermal conductivity plays important roles in mantle dynamics and thermal evolution of Earth and Venus. Although a number of studies have reported thermal properties of bridgmanite, the absolute values and pressure dependence of thermal conductivity of the end member and impurity influence on its thermal conductivity are still controversial. The temperature dependence of bridgmanite thermal conductivity is also poorly constrained. In this study, simultaneous measurements of thermal conductivity (λ) and thermal diffusivity (κ) of post spinel and bridgmanite with five different compositions ($MgSiO_3$, $Mg_{0.97}Fe_{0.03}SiO_3$, $Mg_{0.91}Fe_{0.09}SiO_3$, $Mg_{0.97}Al_{0.05}Si_{0.98}O_3$ and $Mg_{0.89}Fe_{0.09}Al_{0.05}Si_{0.97}O_3$) were performed up to 24 GPa and 1100 K by a pulse heating method in a large volume multi-anvil press. The results show that the addition of a small amount of impurity (5 mol% Al or 3 mol% Fe) to the end member bridgmanite leads to significant decrease of λ, to almost half values. Addition of impurities will decrease not only the absolute value of λ, but also result in smaller pressure, temperature dependence of λ. The impurity influence is not simple linear relationships with substitution amount, additional Al impurity (5 mol%) leads to higher absolute value, pressure dependence and temperature dependence of Fe-bearing bridgmanite ($Mg_{0.91}Fe_{0.09}SiO_3$), possibly due to increase of ferric iron content. The impurity effect on λ could influence the delayed phase transition of a subduction slab at 660 km discontinuity by controlling the conductive heating efficiency, thus, control the residence time of slab stagnancy. The sensitive temperature dependence of the end member λ may provide clues for sharp divergence of secular cooling rate between Earth and Venus.

3.2 Introduction

Geological activities on planets are driven by interior heat engines. The rate and mode of heat

transfer from the center of the planet to the surface controls the intensity of the planet's external geological activity and internal thermal state and dynamics. Thermal conductivity (λ) of planetary mantle materials governs the heat transport inside a terrestrial planet, thus plays important role in determining the long-time evolution of temperature distribution of mantle and core (Stacey and Loper, 1984) and also energy balance of the planet (Lay et al., 2008). Simplified constant λ values are commonly adopted in most numerical simulations. Tosi et al., (2013) demonstrated that variable λ values with pressure and temperature strongly influence the mantle temperature, buoyancy and convection mode. Therefore, to well understand more realistic thermal history and nowadays dynamics of the planet, elaborate pressure-, temperature- and composition-dependent λ of the planet mantle main phases are necessary.

Aluminum (Al)- and iron (Fe)-bearing $MgSiO_3$ bridgmanite is the most abundant mineral in Earth's lower mantle. The composition and spatial distribution of bridgmanite are heterogeneous in the lower mantle. High pressure experiments suggest that bridgmanite in Earth's lower mantle can accommodate a substantial amount of Fe and Al, and the contents depend on the bulk rock composition. Bridgmanite in harzburgite is Al depleted, while bridgmanite in mid ocean ridge basalt (MORB) has considerable high Fe_2O_3 and Al_2O_3 contents of ~ 23 wt.% and ~ 16 wt.%, respectively (Hirose et al., 2005; Irifune et al., 2010; Sinmyo and Hirose, 2013). Bridgmanite-enriched domains might exist in the lower mantle (Ballmer et al., 2017), while at 660 km ringwoodite will break into polycrystalline aggregate of bridgmanite and ferropericlase, which is called post-spinel phase (Ishii et al., 2019). The impurity effect and spatial distribution difference can influence the heat transport performance of bridgmanite. Especially for a subducting slab, in comprise of several rock layers with different compositions, the cold nature and slow thermal equilibration of endothermic reaction will delay the growth of dense bridgmanite at 660 km

seismic discontinuity and lead to stagnancy of slabs at the base of transition zone (Chapman and Clarke, 2021). The different λ of bridgmanite with variable Fe, Al contents in each layered bulk rocks may control the rate of phase transition by altering the conductive heating efficiency during the slab stagnation. Also, as first liquids phase in deep mantle of Earth and Venus (Trønnes et al., 2019), impurity-depleted bridgmanite's λ value under different *P, T* conditions can vary the early-stage magma ocean cooling of the two twin terrestrial planets and related to the divergence of the past evolution and present dynamics of Earth and Venus. Therefore, the pressure, temperature and impurity effect on thermal conductivity of bridgmanite should be fully studied.

A number of studies try to investigate thermal conductivity of bridgmanite under high pressure both in multi-anvil apparatus (Manthilake et al., 2011) and diamond anvil cell (DAC) (Ohta et al., 2012; Hsieh et al., 2017; Okuda et al., 2017; Okuda et al., 2019). However, for both Mg end member case and impurity bearing case, results of multi-anvil method were in illy consistent with those of DAC methods. $MgSiO_3$ bridgmanite λ value derived at ambient temperature in Manthilake et al., (2011) was nearly twice larger than measurement values in Ohta et al., (2012) and Hsieh et al., (2017). Manthilake et al. (2011) demonstrated strong reduction of λ values of bridgmanite by even small addition of Al or Fe impurity. In contrast, Hsieh et al. (2017) showed impurities almost has no influence before a lattice distortion pressure and Okuda et al. (2017) reported only 19% reduction of λ values due to Fe, Al incorporation. The linear relationship with small slope between λ values of bridgmanite and impurity contents given by Okuda et al. (2019) cannot account for results in Manthilake et al. (2011). Also, the temperature dependence of thermal conductivity of bridgmanite was only obtained by Manthilake et al. (2011). Therefore, the existing experimental data are not sufficient to understand thermal properties variations of bridgmanite under different conditions. Moreover, those previous experiment methods failed in direct measurements of

thermal conductivity values, instead, they measured thermal diffusivity (Manthilake et al., 2011; Ohta et al., 2012; Okuda et al., 2017; Okuda et al., 2019) or thermal effusivity (Hsieh et al., 2017). To calculate λ values, estimation values of heat capacity are necessary for such methods, possibly leading to larger errors. Thus, direct and systematic measurements for thermal conductivity values of bridgmanite both with and without impurities are necessary.

In this study, high accuracy pulse heating method (Osako et al., 2004) combining with high-pressure experimental technique was adopted in a large volume multi-anvil apparatus. Simultaneous measurements of thermal conductivity and thermal diffusivity of post-spinel and bridgmanite with 5 different compositions ($MgSiO_3$, $Mg_{0.97}Fe_{0.03}SiO_3$, $Mg_{0.91}Fe_{0.09}SiO_3$, $Mg_{0.97}Al_{0.05}Si_{0.98}O_3$ and $Mg_{0.89}Fe_{0.09}Al_{0.05}Si_{0.97}O_3$) were performed under high pressure up to 24 GPa. At 24 GPa, temperature dependence data were taken up to 1100 K. Based on present data, impurity effects on thermal properties of bridgmanite and its influence on slab dynamics and cooling history of terrestrial planets will be discussed.

3.3 Experimental

3.3.1 Sample preparation

Starting materials for the thermal conductivity measurements were well-sintered polycrystalline post-spinel (aggregate of bridgmanite and ferropericlase with initial composition $(Mg_{0.9}Fe_{0.1})_2SiO_4$) and bridgmanite with the following nominal compositions: $MgSiO_3$, $Mg_{0.97}Fe_{0.03}SiO_3$, $Mg_{0.91}Fe_{0.09}SiO_3$, $Mg_{0.97}Al_{0.05}Si_{0.98}O_3$ and $Mg_{0.89}Fe_{0.09}Al_{0.05}Si_{0.97}O_3$. To obtain post-spinel and bridgmanite samples with homogeneous grain size and required size for measurement experiments (diameter > 2mm), glass rod and aggregates are used as starting material for synthesis experiment.

MgO, SiO_2, Fe_2O_3 and Al_2O_3 powders with different ratios were mixed well in agate mortar with ethanol for desired compositions, The oxide mixtures then were compressed to disk-shaped pellets

with 1–2 mm thickness and baked in gas mixture furnace at 1573 K under iron-wüstite (IW) buffer for more than 8 hours. CO_2 and H_2 gases flowed into the furnace to control the internal oxygen fugacity, and oxides reacted to form olivine and enstatite. After quench, the recovered pellets of compositions for aggregate sintering were well ground to fine-grained powder (~1 μm).

Aggregates with different impurity contents were sintered at 1373 K and 1 GPa in an end-loaded piston cylinder apparatus. To keep the oxygen fugacity of samples and eliminate the contamination of water, Fe foil with 0.02 mm thickness was used as a sample capsule. The recovered samples were well-sintered and then cored to cylindrical shape with 2.3 mm. To avoid trace amounts of water induced fast grain growth, glass rod was chosen as the starting material for the Mg end member synthesis experiment. $MgSiO_3$ enstatite composition pallets were melted by CO_2 laser in a levitation furnace with flowing argon gas at the high-energy X-ray diffraction beamline BL04B2 of SPring-8. After quench in the argon gas flow, bubble-free transparent glass balls with diameter of 2.5-4 mm were obtained (Fig. 3.1). The glass balls were then cut and cored to cylindrical shape with 2.3 mm diameter.

Synthesis experiments were performed at 24 GPa and in temperature range 2000–2100 K in a Kawai-type multi-anvil apparatus (USSA5000). Well-shaped glass and aggregates were loaded into iron (Fe) capsule made of 0.2 mm thick foil. Cr_2O_3-doped MgO octahedra with a 14-mm edge length was used as pressure medium and $LaCrO_3$ sleeve were used as heater. 46 mm tungsten carbide cubes with 6 mm truncation edge length were used for pressure generation. The relationship between power and temperature was established in several test runs. In these runs, the temperature was monitored with a $W_{97}Re_3$–$W_{75}Re_{25}$ thermocouple placed adjacent to the capsule. Then synthesis experiments were performed by power control using the power-temperature relationship to avoid sample deformation induced by thermocouple. The adapted cell assembly can

be found in Fig. 3.2a. The recovered samples with 2.0-2.2 mm diameters were well sintered, and samples with composition of $MgSiO_3$ (Fig. 3.3a) and $Mg_{0.97}Al_{0.05}Si_{0.98}O_3$ (Fig. 3.3b) were even transparent.

3.3.2 Sample characterization

Phase identification of the synthesized materials was performed by two dimensional (2D) micro-focused X-ray diffractometer (RINT RAPID II) in reflection geometry. The X-ray diffraction patterns were identified to be ferropericlase and bridgmanite for post-spinel sample and bridgmanite for other samples. Microstructures of the recovered samples were observed by field-emission scanning electron microscope (FE-SEM). All samples exhibited a homogeneous equigranular texture. For post-spinel, both bridgmanite and ferropericlase have a fine grain size about 1 μm. Grain size of bridgmanite samples were mostly around 10 μm. For $Mg_{0.89}Fe_{0.09}Al_{0.05}Si_{0.97}O_3$, the grain size was finer and about 5 μm. The chemical composition of bridgmanite samples both before and after thermal conductivity measurement were determined by an electron probe microanalyzer (EPMA) (JEOL JXA-8800), although the recovered sample with a composition of $Mg_{0.89}Fe_{0.09}Al_{0.05}Si_{0.97}O_3$ (run 5K3606) was not available due to blow-out during decompression. The average chemical compositions for each sample are shown in Table 3.1.

3.3.3 Thermal conductivity measurement

The thermal conductivity measurements were conducted by means of the pulse-heating method (Osako et al., 2004; Zhang et al., 2019) in the Kawai-type apparatus (USSA5000). Measurements were performed at various pressures up to 24 GPa under room temperature and at 24 GPa data was taken under various temperatures up to 1100 K.

Fig. 3.2b shows the cell assemblies for thermal conductivity measurement. Two 0.25 mm thick TiB_2-doped BN+AlN disks performed as main heaters to provide an ambient temperature. To

realize a constant temperature boundary condition, two molybdenum blocks were used as a heat sink, sandwiching the sample in contact with top and bottom sample disks. The sample area including heat sinks and heaters was surrounded by zirconia sleeve and spacers, which can effectively restrict lateral heat flow to implement one-dimensional heat flow in the sample. An impulse Re heater with 15 μm in thickness and a flattened K-type (chromel-alumel) thermocouple with 0.02 mm in thickness and 0.2 mm in width were inserted on two interfaces between two sample disks to generate a pulse heating and monitor the sample temperature, respectively. The folded shape of impulse heater allowed a uniform and nearly one-dimensional transient heat flow over the cross section of the sample, the corresponding transient signal was detected by thermocouple as a peak of the electromotive force.

3.4 Results and discussion

3.4.1 Pressure response of thermal conductivity of post-spinel and bridgmanite

Fig. 3.4a and 3.4b show thermal conductivity (λ) and thermal diffusivity (κ) of post-spinel and bridgmanite with various compositions measured at room temperature as a function of pressure, respectively. Both λ and κ of post-spinel and bridgmanite monotonically increase with increasing pressure in measured pressure range and were fitted into a linear expression assuming a constant pressure derivative. The coefficients obtained as fitting parameters are listed in Table 3.2.

Both the absolute values and pressure responses of λ of bridgmanite under room temperature are fairly affected by the impurity substitution. The λ values of $Mg_{0.97}Al_{0.05}Si_{0.98}O_3$, $Mg_{0.97}Fe_{0.03}SiO_3$ (En_{97}), $Mg_{0.91}Fe_{0.09}SiO_3$ (En_{91}), and $Mg_{0.89}Fe_{0.09}Al_{0.05}Si_{0.97}O_3$ under ambient condition (1bar, 300 K) estimated from linear regression are 6.3, 5.9, 3.8, and 4.0 $Wm^{-1}K^{-1}$, which are about 60%, 56%, 36%, 38% of $MgSiO_3$ bridgmanite (10.5 $Wm^{-1}K^{-1}$), respectively. The addition of small amount of impurity (5 mol% Al or 3 mol% Fe) yields almost half λ values by enhancement of the mass

disorder, phonon-defect scattering and resonant spin-phonon scattering (Morton and Lewis, 1971; Hsieh et al., 2018), which suppress the phonon transport and reduce the thermal conductivity. The impurity substitution effect is much more pronounced at compositions near the Mg end member, the magnitude of the reduction of λ becomes much milder for further impurity adding.

The pressure derivative of λ ($d\lambda$ / dP) shows several factors of difference within the measured composition range (Table 3.2), from 0.53 ($MgSiO_3$) to 0.09 ($Mg_{0.91}Fe_{0.09}SiO_3$). Such impurity induced pressure-dependence of λ was also found in ferropericlase and olivine solid solution, while the pressure dependences of λ of end member of each are 1 order and 3~4 times larger than impurity-bearing cases, respectively (Part 2; Zhang et al., 2019). Apparently, compared to dramatic impurity effect on ferropericlase with a simple cubic structure (see Part 2), the moderate influence of impurity of bridgmanite is closer to olivine (Zhang et al., 2019), which is also silicate mineral with orthorhombic structure. Absolute value at ambient condition and pressure dependence of post-spinel are about 80% and 68% of $Mg_{0.97}Fe_{0.03}SiO_3$, respectively, which may suggest that effect of ferropericlase phase is smaller than bridgmanite phase at room temperature.

The present study first time acquired a pressure dependence of λ values of bridgmanite in a multi-anvil apparatus. I compare results of this study with previous experimental and simulation results in Fig. 3.5. Although Ångström method measurement in multi-anvil apparatus did not determine pressure dependence of λ for $MgSiO_3$ bridgmanite at room temperature (Manthilake et al., 2011), their room temperature λ value measured at 26 GPa is consistent with value extrapolated from pressure dependence line of this study. Such absolute values and pressure dependence of the end member are also supported by classical molecular dynamics (MD) simulations (Haigis et al., 2012) and *ab initio* lattice dynamics calculations based on phonon gas model (PGM) (Ghaderi et al., 2017). However, room temperature measurements in diamond anvil cell (DAC), both time domain

thermoreflectance (TDTR) method (Hsieh et al., 2017) and light pulse thermoreflectance method (Ohta et al., 2012), showed much smaller absolute values and pressure dependence of $MgSiO_3$ bridgmanite. Such performance of heat transfer is rather closer to our impurity bearing sample ($Mg_{0.89}Fe_{0.09}Al_{0.05}Si_{0.97}O_3$). Moreover, the impurity effect reported by DAC experiments was negligibly small under the measurement pressure range of this study (Hsieh et al., 2017; Okuda et al., 2017; Okuda et al., 2019). One possible explanation for the discrepancy between multi-anvil results and DAC results can be the difference of sample. As polycrystalline $MgSiO_3$ bridgmanite sample used in this study (Fig. 3.3) are well sintered from bubble free glass quenched in Ar gas flow (Fig. 3.1), the effect of water can be excluded. In addition, the transparency of our sample may suggest much smaller phonon-defect scattering and phonon-boundary scattering. Therefore, end member results of this study are in good agreement with simulation results of Ghaderi et al. (2017), which correspond to crystals with no defects.

Okuda et al. (2019) estimated the λ of their impurity bearing bridgmanite samples at 135 GPa and 300 K, combined with Ohta et al., (2012) and Okuda et al., (2017) results, and provided a linear relationship between λ of (Al, Fe)-bearing bridgmanite and the summation of Fe and Al content in per formula unit. Here I plot our estimated values of λ in this study at both 0 GPa and 135 GPa under room temperature together with data used by Okuda et al. (2019) in Fig. 3.6. Apparently, the composition dependence of λ suggested by this study is far from simple linear correlation. This trend is more similar to that of olivine presented in Zhang et al. (2019), although it becomes more complex due to Al substitution. Even with higher impurity content in per formula unit, $Mg_{0.97}Al_{0.05}Si_{0.98}O_3$ has slightly higher absolute value and pressure dependence than $Mg_{0.97}Fe_{0.03}SiO_3$. This can be explained by smaller atomic mass and induced mass disorder of Al than Fe, with same molar amount, later one will produce more reduction of phonon group velocity

and has shorter phonon lifetime thus result in lower λ value. I also found $Mg_{0.89}Fe_{0.09}Al_{0.05}Si_{0.97}O_3$ had larger pressure dependence and absolute value than $Mg_{0.91}Fe_{0.09}SiO_3$, the additional Al impurity increased the conduction efficiency of bridgmanite at room temperature. One possible reason is that the addition of Al will increase ferric iron (Fe^{3+})/ ferrous iron (Fe^{2+}) ratio in bridgmanite (Frost et al., 2004). Fe^{3+} may has smaller influence than Fe^{2+}. Also, Fe^{3+} and Al^{3+} pair is very stable, and will decrease the vacancy number caused by Fe^{3+}, therefore can decrease the phonon-defect scattering and show better heat transport ability under ambient temperature.

3.4.2 Temperature dependence of thermal conductivity of post-spinel and bridgmanite

Fig. 3.7 shows λ and κ of post-spinel and bridgmanite with various impurity contents measured under high pressure as a function of temperature. Both the λ and κ of all compositions exhibit a monotonically decreasing trend with increasing temperature, which is typical temperature dependence for thermal properties of minerals. Pertermann and Hofmeister (2006) have inferred that based on the damped harmonic oscillator-phonon gas model (Debye et al., 1914) and spectroscopic and elastic measurements (Kolesov and Geiger, 2004), κ of minerals can be represented by:

$$\kappa = A_0 + \frac{B_0}{T} + \frac{C_0}{T^2} + \cdots \tag{3.1}$$

where A_0, B_0 and C_0 are constant. Thermal diffusivity data of this study can be well fitted against temperature using Eq. (3.1). Fitting results of all data are given in Table 3.2.

The variation of λ with temperature was fitted into a well-accepted empirical power-law approach to show the combined effects of pressure and temperature on thermal conductivity. The only fitting parameter is the exponent n. The fitting results of the following expressions are given in Table 3.2:

$$\lambda = \lambda_{295K,P} \left(\frac{295}{T}\right)^n, \tag{3.2}$$

where $\lambda_{295K,\ P}$ is the thermal conductivity value at 295 K and specified pressure derived from the pressure dependence fitting results (Table 3.2). *n* implies the temperature dependence of λ.

Post-spinel has a small *n* value about 0.3, nearly half of $Mg_{0.97}Fe_{0.03}SiO_3$. Such small temperature dependence exhibits the impact of ferropericlase with composition around $Mg_{0.8}Fe_{0.2}O$, an extremely temperature insensitive material (see Part 2).

For bridgmanite, parameter *n* of end member is near 1 at relatively low temperature (< 800 K) and decrease to 0.7 due to possible saturation at higher temperature (>800 K), while those of impurity-bearing bridgmanite are much smaller than 1. With the increase of impurity content, *n* becomes smaller, such a phenomenon is similar to olivine (Zhang et al., 2019). For olivine, *n* changes from about 1 for end member to ~ 0.7 for olivine with 10 mol% Fe substitution. For bridgmanite, *n* reduces from around 1 to ~ 0.6 with only 3 mol% introducing of Fe and even drops to about 0.2 with more Fe addition (9 mol%). This may indicate that impurity influence on temperature dependence is more pronounced for bridgmanite.

$Mg_{0.89}Fe_{0.09}Al_{0.05}Si_{0.97}O_3$ shows much larger temperature dependence than $Mg_{0.91}Fe_{0.09}SiO_3$ and has smaller thermal conductivity at higher temperature. Two factors may lead to such results. First, the phonon-defect is more significant at low frequency, which means the vacancy induced lowering of $Mg_{0.91}Fe_{0.09}SiO_3$ λ will affect less under high temperature. Second, $Fe^{3+}AlO_3$ charge-coupled substitution distorts the B-site octahedral more (Huang et al., 2021), under high temperature, the dominant phonon-phonon scattering might be more intense due to such distorting and larger mass disorder.

I compared the present data with the only bridgmanite thermal conductivity λ and thermal diffusivity κ temperature dependence data reported by Manthilake et al. (2011) in Fig. 3.8a and 3.8b. The composition of samples used in Manthilake et al. (2011) is very close to this study, only

Al-bearing bridgmanite is slightly different, 2.5 mol% $AlAlO_3$ addition in this study while 2 mol% adding in their experiment. For impurity-bearing bridgmanite, κ values are in fairly good agreement with each other. However, the discrepancy of λ values can be as large as 56% of values of this study. The Ångström method used by Manthilake et al. (2011) actually measured the κ of sample, λ values were acquired through calculation using assumed heat capacity value. I thus assign such divergency to improper choice of heat capacity in their study. As for end member composition, both λ and κ values have a difference as large as 40% of values of this study. This study implies a larger temperature dependence of the end member λ value. The disparity might come from the different conditions of $MgSiO_3$ bridgmanite samples, for example, defect content, grain size and transparency of the sample might all alter the phonon scattering under different temperatures.

3.4.3 Heat capacity

One advantage of pulse heating method is that the simultaneous measurement of λ and κ allows us to acquire heat capacity information. Heat capacity C can be calculated from measured λ and κ by:

$$C = \frac{\lambda}{\rho\kappa} \tag{3.3}$$

The calculated C should be an average value of C_v and C_p considering the boundary condition of this method. In Fig. 3.9, comparison with literature calculated ambient pressure heat capacity value of $MgSiO_3$ bridgmanite is shown, which was based on experimental *P-V-T* measurement data and Kieffer's model of C_V (Saxena et al., 1999). Heat capacity obtained by this study is firmly consistent with such calculated values within error, suggesting that pulse heating method can provide valuable referenceable heat capacity value under high pressure. As introduced before, other high pressure thermal conductivity measurement methods don't directly measure λ and

assumed C is needed. Discrepancy between groups may be partially caused by different adopted C value. Therefore, I also plotted heat capacity values used by Hsieh et al. (2017), Okuda et al. (2017) and Okuda et al. (2019) in Fig. 3.9. Hsieh et al. (2017) used values almost the same as values obtained in this study while much smaller values were chosen by Okuda et al. (2017) and Okuda et al. (2019). Despite this, we cannot explain the inconsistency between multi-anvil results and DAC results only by heat capacity difference. More experimental studies are needed to find the reason for the disagreement.

3.5 Planetary implication

3.5.1 Compositional dependent λ contribute to the stagnancy of subduction slabs

Most subducted oceanic lithosphere tends to sink to the core-mantle boundary as the relatively lower temperature inside of the slabs make them denser than the surrounding pyrolite mantle almost throughout the whole mantle condition (Ringwood, 1975; Fukao et al., 1992). Nevertheless, seismic tomographic images show that many slabs deflected subhorizontally above, across or below the 660 km discontinuity, which are regarded so called stagnant slabs (Fukao et al., 2009). Several mechanisms have been proposed to clarify such stagnation, one plausible explanation is the density inversion between due to a negative Clapeyron slope induced deeper depth phase transition reaction: ringwoodite decomposed to bridgmanite and ferropericlase (e.g., Irifune & Ringwood, 1987). Such stalling may not be permanent, the conductive heating from the surrounding mantle will gradually trigger the delayed growth of ferropericlase and bridgmanite and thermal weakening (Nakakuki et al., 2010; Chapman et al., 2021). Also, during such evolution, basalt may become less dense than harzburgite and pyrolite, thus be 'filtered' by transition zone (Weinstein, 1992). Impurity induced complex pressure, temperature dependence variation of λ of bridgmanite can help understand the thermal and chemical evolution within the stalling slabs and

may related to a rapid switching of subduction dynamics (from stagnation to penetration) in the lower mantle (Agrusta et al., 2017).

I calculate the λ values of bridgmanite with different impurity content along the adiabatic temperature profile of Earth's interior (Katsura et al., 2010) and cold slab geotherm (Thompson 1992) according to fitting results of this study (Table 3.2). Fig. 3.10 shows the depth profiles for λ at usual slabs stagnant depth. Unlike temperature-insensitive λ of ferropericlase, bridgmanite thermal properties both sensitive to pressure and temperature, therefore the value gaps due to pressure dependence difference between different impurity bearing cases will be somehow offset by temperature dependence change. However, heat conduction performance of various compositions still has non-negligible disparities. Compositions of $Mg_{0.91}Fe_{0.09}SiO_3$ and $Mg_{0.89}Fe_{0.09}Al_{0.05}Si_{0.97}O_3$ in this study can represent bridgmanite in harzburgite and pyrolite respectively. As for a subducted MORB rock, Fe and Al contents of bridgmanite are believed to be both ~10 mol% (e.g., Sinmyo et al., 2011), which has even higher Al content than the highest impurity bearing composition in this study. As shown in Fig. 3.10, at usual slab stalling depth (between 660 km and 1000 km), λ of bridgmanite in harzburgite is about 1.5 times larger than bridgmanite in pyrolite under both surrounding mantle condition and a cold slab condition. MORB bridgmanite which contain twice amount of Al than pyrolite bridgmanite is expected to have even lower thermal conductivity due to larger mass disorder, lower phonon group velocity and possible larger temperature dependence due to more Al^{3+}-Fe^{3+} pair. Therefore, for a stagnant slab with layered structure following orders of MORB, harzburgite and pyrolite from up down, the conduction heating efficiency are quite different for different parts. Fig 3.11a and 3.11b are schematic figures for scenarios of initial stagnant of a slab at 660 km and after long time subhorizontal deflection around 660 km. At initial stalling stage, the formation of bridgmanite in

MORB with low λ at the top surface of slab and the existence of garnet with low λ (Osako, et al., 2004) in MORB layer will retard heat conduction toward center of the slab. In a bottom part of the stagnant slab composed of pyrolite bridgmanite, heat conduction from the surrounding mantle beneath the slab will be a bit faster than that from the top, but its efficiency will slowly become worse as temperature increases due to lower λ value at higher temperature. Small λ value of slab surface impedes the temperature equilibrium between surrounding hot mantle and colder slab, thus delayed the transition to denser phase inside of the slabs, resulting in long time struggle of slabs at the base of transition zone, which could be longer than previous estimation based on results of this study. As the formation of bridgmanite in MORB needs higher temperature than in harzburgite and pyrolite (Chapman et al., 2021), once enough temperature triggered reaction (to form bridgmanite + ferropericlase) in the harzburgite layer, efficiency of heat conduction and density inversion between MORB and harzburgite will abruptly increase. And the following increase of temperature will not bother heat conduction of such temperature-insensitive harzburgite layer much. The density inversion and viscosity contrast with surrounding mantle will even cause the 'peel' of MORB layer from downside layers due to larger buoyancy and high viscosity of bridgmanite-lack MORB at this depth (van Keken et al., 1996), and the direct touch of surrounding mantle with harzburgite will further accelerate the thermal equilibrium. Therefore, rapid temperature rising and phase transition will start within the center of the slab. Within a much shorter period, the delayed growth of bridgmanite and ferropericlase in the slab center will finished, the consequently denser slab then may start to penetrate downward again.

3.5.2 Effect of temperature-sensitive λ on early-stage cooling rate of Venus and Earth

Venus and Earth are regarded as twin planets, the different thermal evolutions of planetary interior between two planets provide hints for understanding how chemical and physical variables

alter rocky planet evolution. Unlike Earth with a dynamo more than 3.4 Gyr (Tarduno et al., 2010), today's Venus has no global magnetic field (Phillips and Russell, 1987). Whether such phenomena are caused by lack of an inner core (e.g., Nimmo and Stevenson 2000) or a completely frozen solid core of Venus (Dumoulin et al., 2017) has been debated for a long time. Early thermal history of two planets may hold clues for present day sharp divergency, such as the existence of plate tectonics and magnetic field. Bridgmanite can be considered to be a main phase in the lower mantle and a liquidus phase at the base of deep magma ocean of large rocky planets (Ito et al., 2004). The thermal properties of bridgmanite can control the cooling rate of two twin planets. The initially crystallized bridgmanite should be Fe-depleted and will sink or float to depth of a neutral buoyancy around 72-80 GPa (1700-1860 km) in the Earth magma ocean (Trønnes et al. 2019). A stable accumulated layer of bridgmanite at this depth will separate the magma ocean and govern the heat loss from basal magma ocean and underlying core. For Venus, which has smaller size and less density than Earth, such an accumulated layer should be in a deeper part considering the neutron buoyancy condition, where the temperature could be higher (Trønnes et al. 2019). Since λ of $MgSiO_3$ has a large temperature dependence, which has been suggested both by experiment measurement results of this study and simulation predictions (Ghaderi et al., 2017), a lower λ of the early accumulated bridgmanite can be speculated in Venus. This means Venus has a slower early cooling rate of the basal magma ocean and core than Earth. Also, with the secular cooling, the λ will gradually increase, suggesting that the initially slower cooling rate will have more and more large heat loss gap with faster one. Such initial interior heat transport differences may trigger the long-time evolution paths diverse. Therefore, based on the temperature-sensitive thermal conductivity of bridgmanite, the lower mantle dominant phase, an entire liquid core of Venus is preferred from the view of this study.

3.6 Conclusion

The major conclusions of this work are as follows:

i. Thermal conductivity of bridgmanite is strongly affected by impurity. The λ values of $Mg_{0.97}Al_{0.05}Si_{0.98}O_3$, $Mg_{0.97}Fe_{0.03}SiO_3$, $Mg_{0.91}Fe_{0.09}SiO_3$, and $Mg_{0.89}Fe_{0.09}Al_{0.05}Si_{0.97}O_3$ under ambient condition (1bar, 300 K) estimated from linear regression are about 60%, 56%, 36%, 38% of $MgSiO_3$ bridgmanite, respectively.

ii. The pressure response of λ of bridgmanite is reduced by impurity. Additional adding of small amount of Al can increase pressure dependence of Fe-bearing bridgmanite.

iii. Thermal conductivity of Mg end member bridgmanite is sensitive to temperature variation. Impurity will decrease the temperature dependence of λ, Al substitution will increase temperature dependence of Fe-bearing bridgmanite.

iv. Different λ values of bridgmanite in MORB, harzburgite, and pyrolite can lead to different conductive heating efficiency for stagnant slabs. Faster heat conduction of harzburgite bridgmanite will result in quick completion of transition to denser phase inside the slabs and trigger restart of sinking of a stagnant slab.

v. Temperature-sensitive λ value of Mg end member bridgmanite may cause the magma ocean cooling rate difference from the initial crystallization of impurity depleted bridgmanite.

Reference

Agrusta, R., Goes, S., van Hunen, J. (2017). Subducting-slab transition zone interaction: Stagnation, penetration and mode switches. Earth and Planetary Science Letters, 464, 10–23.

Ballmer, M. D., Houser, Hernlund, C. J. Wentzcovitch, W. R. M. Hirose, K. (2017). Persistence of strong silica-enriched domains in the Earth's lower mantle, Nat. Geosci., 10(3), 236–240.

Chapman, T., Clarke, G. L. (2021). Delayed Growth of Ferropericlase and Bridgmanite Controls Slab Residence at the 660-km Discontinuity. J. Geophys. Res, 126, e2020JB021487.

Debye, P. (1914). Vorträge über die kinetische Theorie der Materie und der Elektrizität. B.G. Teuber, Berlin.

Dumoulin, C., Tobie, G., Verhoeven, O., Rosenblatt, P., Rambaux, N. (2017). Tidal constraints on the interior of Venus. J. Geophys. Res., Planets 122, 1338–1352.

Frost, D. J., Liebske, C., Langenhorst, F., McCammon, C. A., Tronnes, R. G., Rubie., D. C. (2004). Experimental evidence for the existence of iron-rich metal in the Earth's lower mantle, Nature, 428, 409–412.

Fukao, Y., Obayashi, M., Inoue, H., Nenbai, M. (1992). Subducting slabs stagnant in the mantle transition zone. Journal of Geophysical Research, 97, 4809–4822.

Fukao, Y., Obayashi, M., Nakakuki, T., & Deep Slab Project Group (2009). Stagnate slab: A review. Annual Review of Earth and Planetary Sciences, 37, 19–46.

Ghaderi, N., Zhang, D-B., Zhang, H., Xian, J., Wentzcovitch, R.M., Sun, T. (2017). Lattice thermal conductivity of MgSiO3 perovskite from first principles. Sci. Rep., 7 (2017), p. 5417.

Haigis, V., Salanne, M. Jahn, S. (2012). Thermal conductivity of MgO, MgSiO3 perovskite and post-perovskite in the Earth's deep mantle, Earth Planet. Sci. Lett., 355–356, 102–108.

Hirose, K., Takafuji, N., Sata, N., Ohishi, Y. (2005). Phase transition and density of subducted

MORB crust in the lower mantle. Earth and Planetary Science Letters, 237, 239–251.

Hsieh, W.P., Deschamps, F., Okuchi, T., Lin, J.F. (2017). Reduced lattice thermal conductivity of Fe-bearing bridgmanite in Earth's deep mantle. J. Geophys. Res., Solid Earth, 122 (7) (2017), pp. 4900-4917

Huang, R., Boffa-Ballaran, T., McCammon, C. A., Miyajima, N., Frost, D. J. (2021). The effect of Fe-Al substitution on the crystal structure of MgSiO3 bridgmanite. Journal of Geophysical Research, 126, e2021JB021936.

Irifune, T., & Ringwood, A. E. (1987). Phase transformations in a harzburgite composition to 26 GPa: Implications for dynamical behavior of subducting slab. Earth and Planetary Science Letters, 86, 365–376.

Irifune, T., Shinmei, T., McCammon, C.A., Miyajima, N., Rubie, D.C., Frost, D.J. (2010). Iron partitioning and density changes of pyrolite in Earth's lower mantle. Science, 327, pp. 193-195.

Ishii, T., Huang, R., Myhill, R., Fei, H., Koemets, I., Liu, Z., Maeda, F., Yuan, L., Wang, L., Druzhbin, D., Yamamoto, T., Bhat, S., Farla, R., Kawazoe, T., Tsujino, N., Kulik, E., Higo, Y., Tange, Y., Katsura, T. (2019). Sharp 660-km discontinuity controlled by extremely narrow binary post-spinel transition. Nature Geoscience, 12(10), 869–872.

Ito, E., Kubo, A., Katsura, T., Walter, M.J. (2004). Melting experiments of mantle materials under lower mantle conditions with implications for magma ocean differentiation. Phys. Earth Planet. Inter., 143–144, pp. 397-406.

Katsura, T., Yoneda, A., Yamazaki, D., Yoshino, T., Ito, E. (2010). Adiabatic temperature profile in the mantle. Phys. Earth Planet. Inter., 183, pp. 212-218.

Kolesov, B.A., Geiger, C.A. (2004). A temperature-dependent single-crystal Raman spectroscopic study of fayalite: evidence for phonon-magnetic excitation coupling. Physics and Chemistry of

Minerals, 31, 155–161.

Lay, T., Hernlund, J., Buffett, B. A. (2008). Core–mantle boundary heat flow. Nat. Geosci. 1, 25–32.

Manthilake, G.M., de Koker, N., Frost, D.J., McCammon, C.A. (2011). Lattice thermal conductivity of lower mantle minerals and heat flux from Earth's core. Proc. Natl. Acad. Sci. USA, 108, pp. 17901-17904.

Morton, I.P., Lewis, M.F. (1971). Effect of iron impurities on the thermal conductivity of magnesium oxide single crystals below room temperature. Phys. Rev. B, 3, pp. 552-559.

Nakakuki, T., Tagawa, M., Iwase, Y. (2010). Dynamical mechanisms controlling formation and avalanche of a stagnant slab. Physics of the Earth and Planetary Interiors, 183, 309–320.

Nimmo, F., Stevenson, D. (2000). Influence of early plate tectonics on the thermal evolution and magnetic field of Mars. J. Geophys. Res. 105, 11,969–11,979.

Ohta, K., Yagi, T., Taketoshi, N., Hirose, K., Komabayashi, T., Baba, T., Ohishi, Y., Hernlund, J. (2012) Lattice thermal conductivity of MgSiO3 perovskite and post-perovskite at the core–mantle boundary. Earth Planet Sci Lett 349–350:109–115.

Okuda, Y., Ohta, K., Yagi, T., Sinmyo, R., Wakamatsu, T., Hirose, K., Ohishi, Y. (2017). The effect of iron and aluminum incorporation on lattice thermal conductivity of bridgmanite at the Earth's lower mantle. Earth Planet. Sci. Lett., 474, pp. 25-31, 10.1016/j.epsl.2017.06.022.

Okuda, Y., Ohta, K., Sinmyo, R., Hirose, K., Yagi, T., Ohishi, Y. (2019). Effect of spin transition of iron on the thermal conductivity of (Fe, Al)-bearing bridgmanite. Earth and Planetary Science Letters, 520, 188–198.

Osako, M., Ito, E., Yoneda, A. (2004). Simultaneous measurements of thermal conductivity and thermal diffusivity for garnet and olivine under high pressure. Phys. Earth Planet. Inter. 143–144,

311-320.

Pertermann, M., Hofmeister, A.M. (2006). Thermal diffusivity of olivine-group minerals. Am. Mineral 91, 1747–1760.

Phillips, J.L., Russell, C.T. (1987). Upper limit on the intrinsic magnetic field of Venus. J. Geophys. Res. 92, 2253–2263.

Ringwood, A. E. (1975). Composition and petrology of the Earth's mantle. New York. McGraw-Hill.

Saxena, S. K., Dubrovinsky, L. S., Tutti, F., LeBihan, T. (1999). Equation of state of MgSiO3 with the perovskite structure based on experimental measurements, Amer. Mineral., 84, 226–232.\

Sinmyo, R., Hirose, K., Muto, S., Ohishi, Y., Yasuhara, A. (2011). The valence state and partitioning of iron in the Earth's lowermost mantle. J. Geophys. Res., 116, Article B07205.

Sinmyo, R., Hirose, K. (2013). Iron partitioning in pyrolitic lower mantle, Phys. Chem. Miner., 40, 107–113.

Stacey, F. D., Loper, D. E. (1984). Thermal histories of the core and mantle, Phys. Earth Planet. Inter., 36, 99–115.

Tarduno, J.A., Cottrell, R.D., Watkeys, M.K., Hofmann, A., Doubrovine, P.V., Mamajek, E.E., Liu, D., Sibeck, D.G., Neukirch, L.P., Usui, Y. (2010). Geodynamo, solar wind, and magnetopause 3.4 to 3.45 billion years ago. Science, 327, pp. 1238-1240.

Thompson, A. B. (1992). Water in the Earth's upper mantle, Nature, 358, 295–302.

Tosi, N., Grott, M., Plesa, A.-C., Breuer, D. (2013). Thermochemical evolution of Mercury's interior. J. Geophys. Res. Planets, 118, 2474–2487.

Trønnes, R. G., Baron, M. A., Eigenmann, K. R., Guren, M. G., Heyn, B. H., Løken, A., Mohn, C. E. (2019). Core formation, mantle differentiation and core-mantle interaction within Earth and the

terrestrial planets. Tectonophysics, 760, 165–198.

van Keken, P. E., Karato, S., Yuen, D. A. (1996). Rheological control of oceanic crust separation in the transition zone. Geophys. Res. Lett. 23, 1821–1824.

Weinstein, S. A. (1992). Induced compositional layering in a convecting fluid layer by an endothermic phase-transition, Earth Planet. Sci. Lett., 113(1–2), 23–39.

Zhang, Y., Yoshino, T., Yoneda, A., Osako, M. (2019). Effect of iron content on thermal conductivity of olivine with implications for cooling history of rocky planets. Earth and Planetary Science Letters, 519, 109–119.

Tables

Table 3.1 Chemical composition of synthetic bridgmanite aggregates before and after thermal conductivity measurement.

	5K3636	5K3617	5K3629	5K3563	5K3602
SiO_2	60.54	60.25	58.74	58.83	57.66
MgO	40.81	39.08	35.74	39.34	35.63
FeO	0	2.19	6.27	0	6.49
Al_2O_3	0	0	0	2.58	2.53
Total	101.35	101.52	100.75	100.75	102.31
	5K3637	5K3623	5K3632	5K3273	5K3606
SiO_2	59.83	59.74	58.42	59.06	
MgO	40.68	39.26	36.01	39.77	
FeO	0	2.13	6.55	0	
Al_2O_3	0	0	0	2.61	
Total	100.51	101.13	100.98	101.44	

For each sample, five different spots were analyzed.

Table 3.2 Fitting parameters of thermal conductivity λ and thermal diffusivity κ

Composition	**$\lambda = a_0P + a_1$**		**$\kappa = b_0P + b_1$**	
	a_0 (GPa^{-1})	a_1 ($Wm^{-1}K^{-1}$)	b_0 (GPa^{-1})	b_1 ($10^{-6}m^2s^{-1}$)
$MgSiO_3$	0.530	10.549	0.140	3.141
$Mg_{0.97}Fe_{0.03}SiO_3$	0.199	5.878	0.046	1.702
$Mg_{0.91}Fe_{0.09}SiO_3$	0.089	3.815	0.024	1.004
$Mg_{0.97}Al_{0.05}Si_{0.98}O_3$	0.269	6.303	0.066	1.867
$Mg_{0.89}Fe_{0.09}Al_{0.05}Si_{0.97}O_3$	0.150	3.957	0.031	1.114
Post spinel	0.136	4.752	0.028	1.263
Composition	$\lambda = \lambda_{295K,\,P}(295/T)^n$		$\kappa = A_0 + B_0T^{-1} + C_0T^{-2}$	
	n		A_0	B_0	C_0
$MgSiO_3$ (T < 800K)	1.107		1.312	-699.692	672373.122
$MgSiO_3$ (T > 800K)	0.702				
$Mg_{0.97}Fe_{0.03}SiO_3$	0.562		0.688	148.576	138779.473
$Mg_{0.91}Fe_{0.09}SiO_3$	0.160		0.364	412.067	-17152.851
$Mg_{0.97}Al_{0.05}Si_{0.98}O_3$	0.622		0.819	-37.353	235508.515
$Mg_{0.89}Fe_{0.09}Al_{0.05}Si_{0.97}O_3$	0.498		0.442	300.678	34856.699
Post spinel	0.318		0.307	518.175	-13980.932

Figures

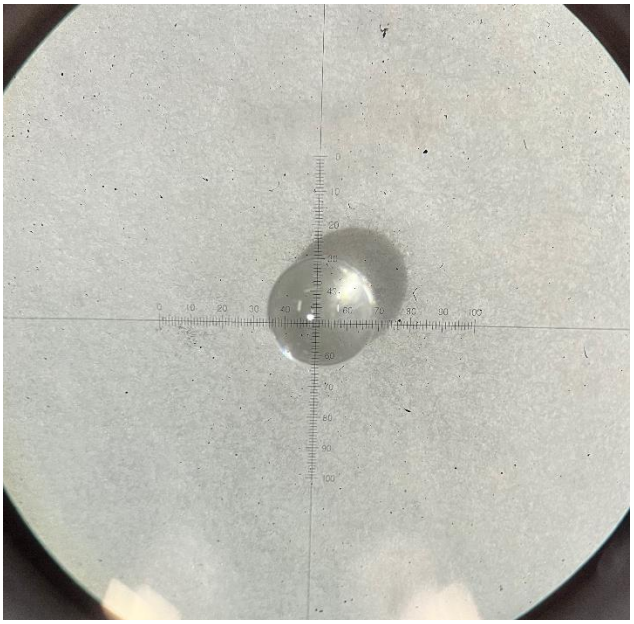

Fig. 3.1 Typical bubble-free MgSiO3 glass made in levitation furnace.

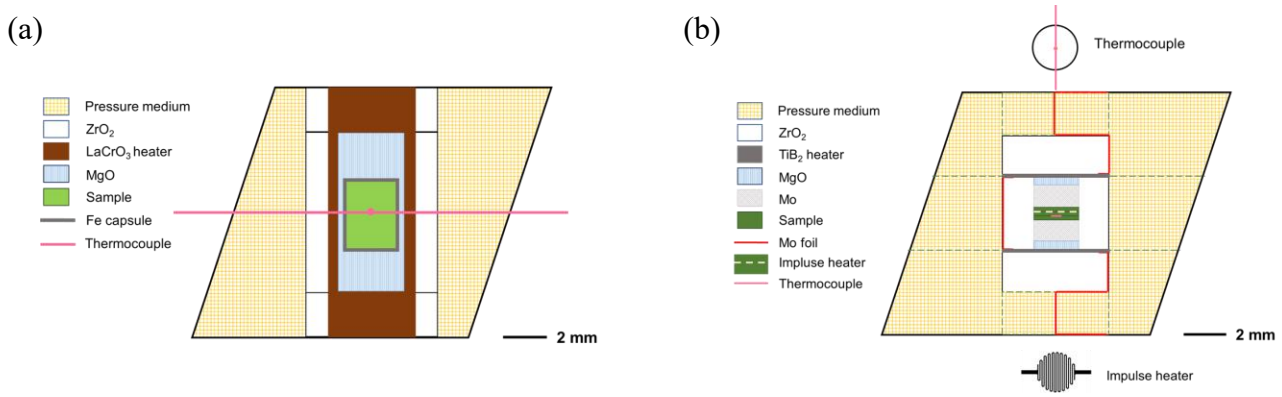

Fig. 3.2 (a) 14/6 cell for synthesis experiments of post spinel and bridgmanite. (b) 14/6 cell for thermal conductivity measurement experiments.

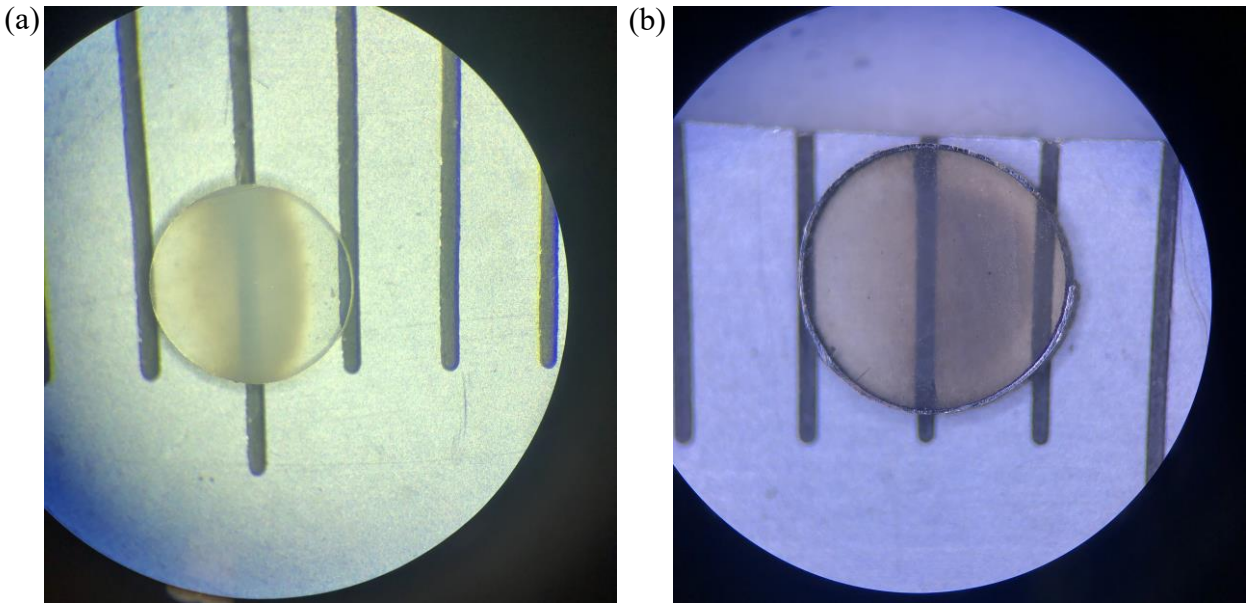

Fig. 3.3 (a) MgSiO3 bridgmanite sample used in this study. (b) $Mg_{0.97}Al_{0.05}Si_{0.98}O_3$ bridgmanite sample used in this study.

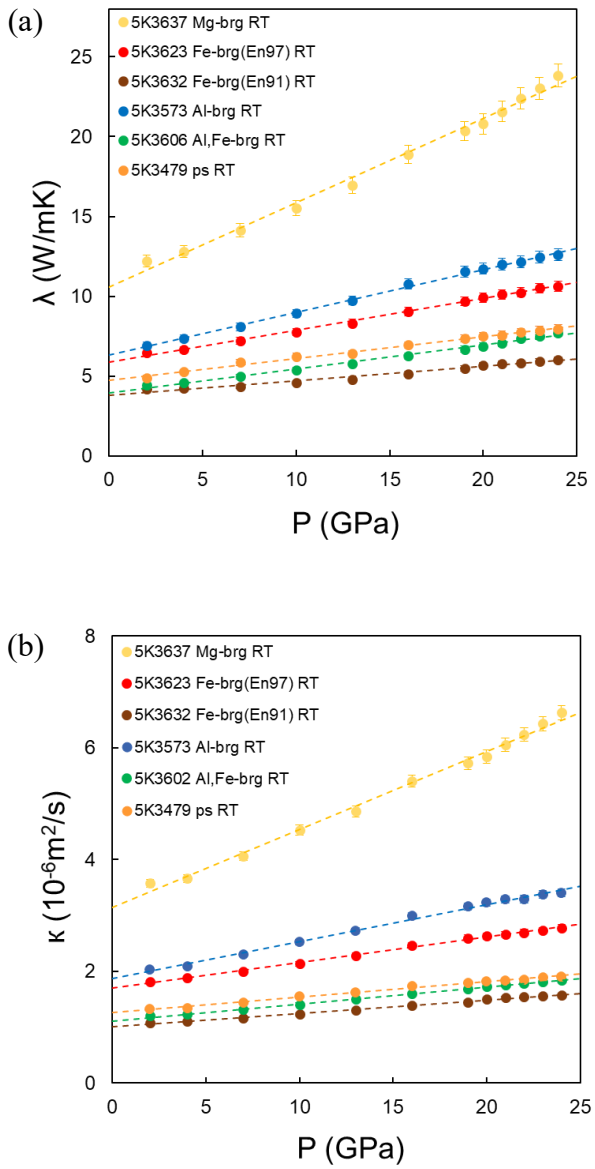

Fig. 3.4 (a) Pressure dependence of thermal conductivity λ of post-spinel and bridgmanite: fitting results of measurement values are shown in dashed lines. (b) Pressure dependence of thermal diffusivity κ of post-spinel and bridgmanite: fitting results are shown in dashed lines. Errors of λ (ca. 5% for $MgSiO_3$ bridgmanite and 3% for other compositions) and κ (ca. 2%) are summation of the uncertainties derived from heating area S, pulse heating power W, sample thickness d and the fitting errors of A and B.

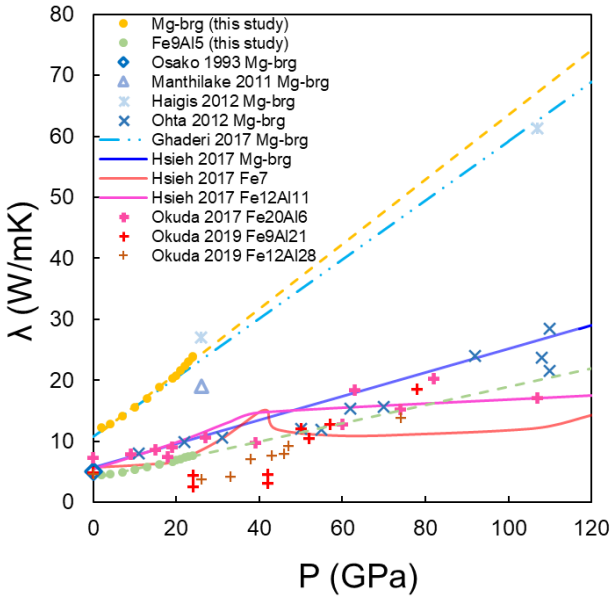

Fig. 3.5 Comparison of room temperature thermal conductivity λ of bridgmanite with previous study.

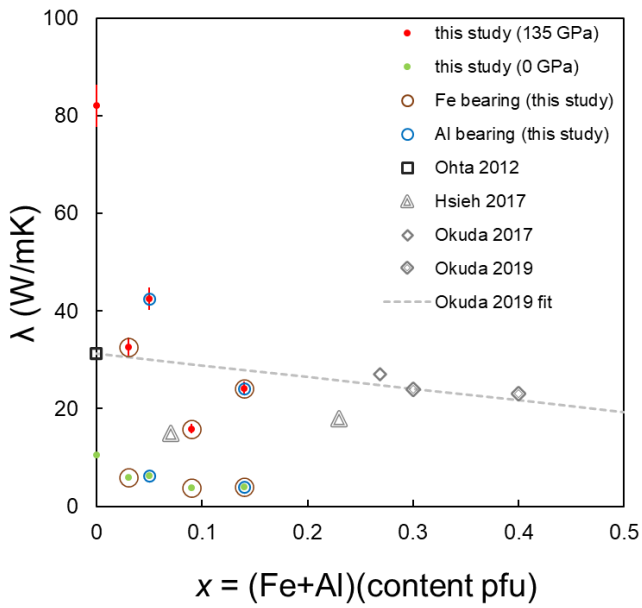

Fig. 3.6 Composition dependence of thermal conductivity λ of bridgmanite at room temperature.

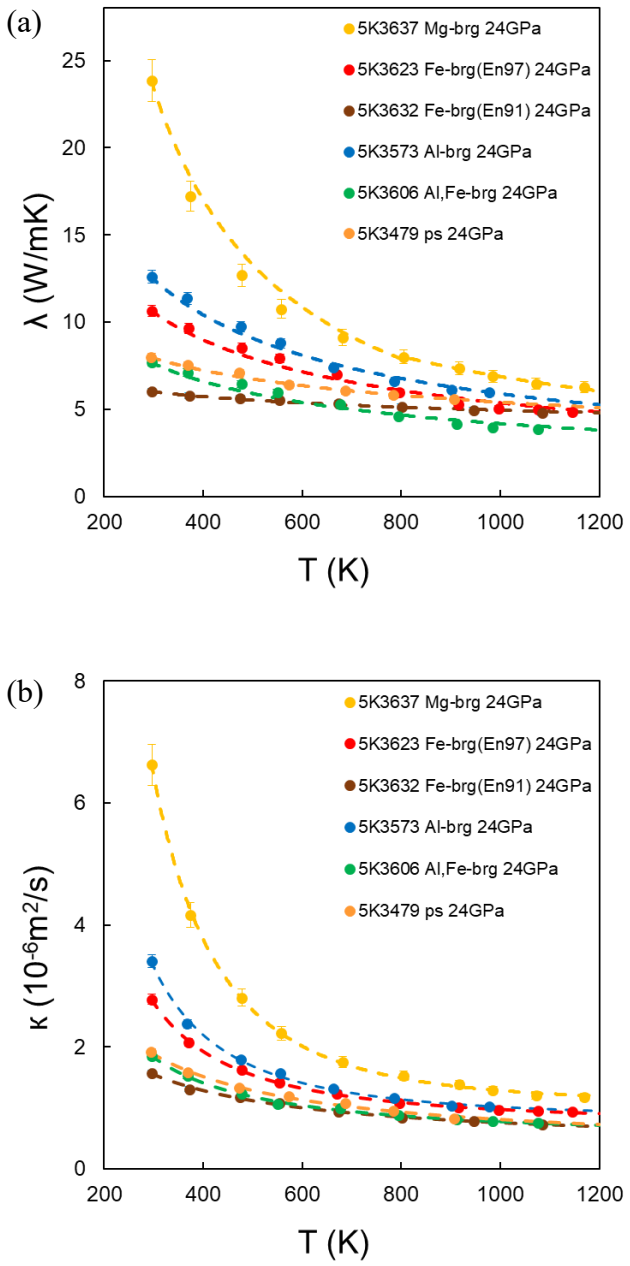

Fig. 3.7 (a) Temperature dependence of thermal conductivity λ of post-spinel and bridgmanite with different impurity contents at 24 GPa. (b) Temperature dependence of thermal diffusivity κ of post-spinel and bridgmanite with different impurity contents at 24 GPa.

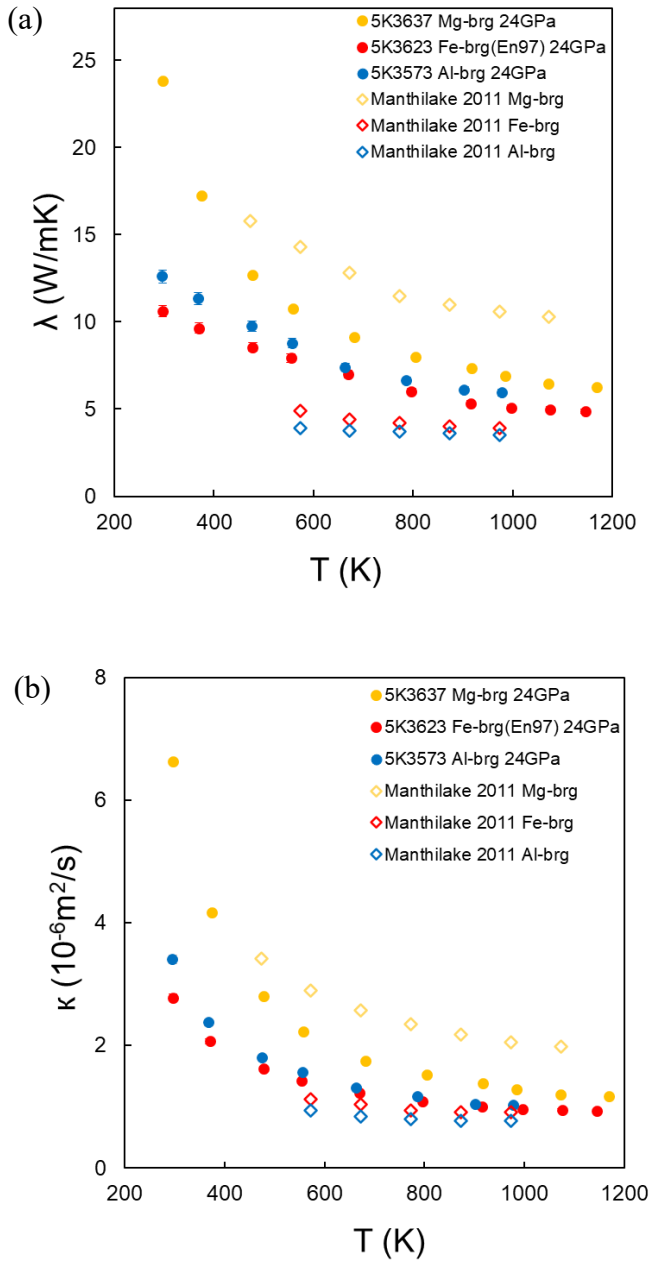

Fig. 3.8 Comparison of thermal conductivity λ and thermal diffusivity κ of bridgmanite under high temperature with previous study.

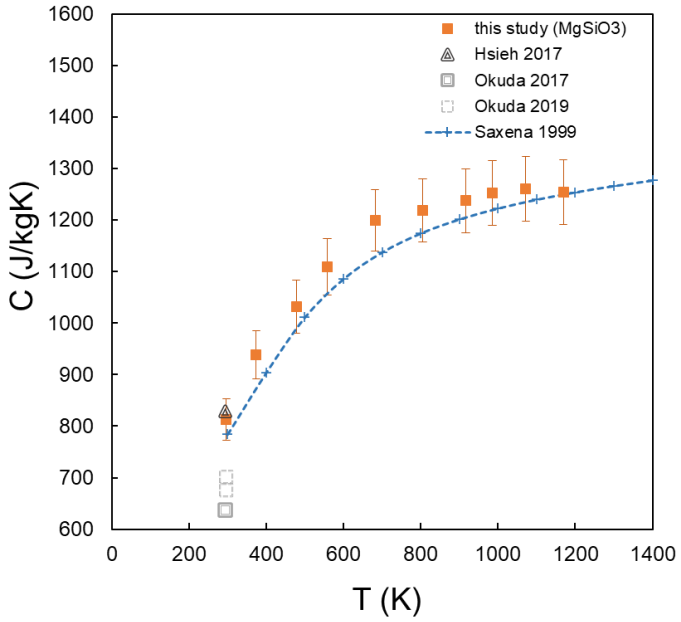

Fig. 3.9 Comparison of heat capacity *C* of bridgmanite with previous study.

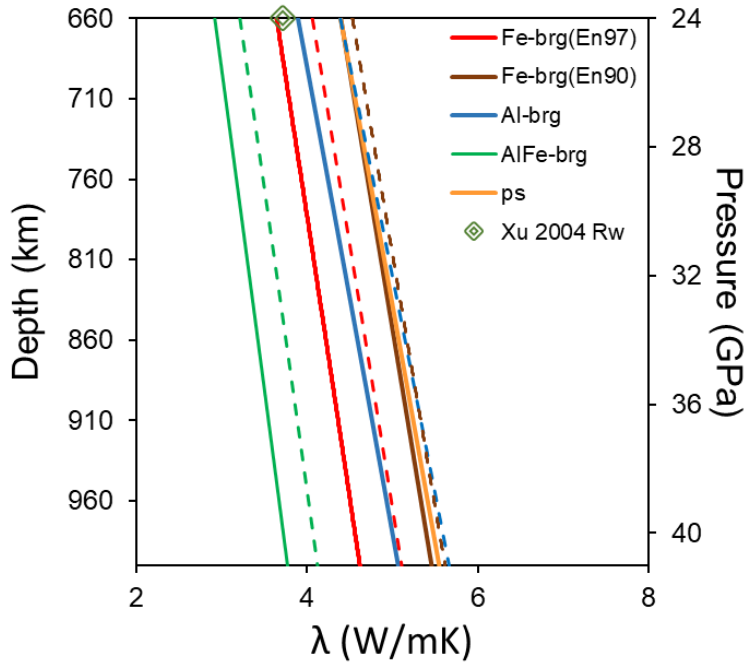

Fig. 3.10 Thermal conductivity of bridgmanite with different impurity contents along mantle geotherm and cold slab geotherm. Solid lines represent average mantle conditions and dashed lines represent cold slab conditions.

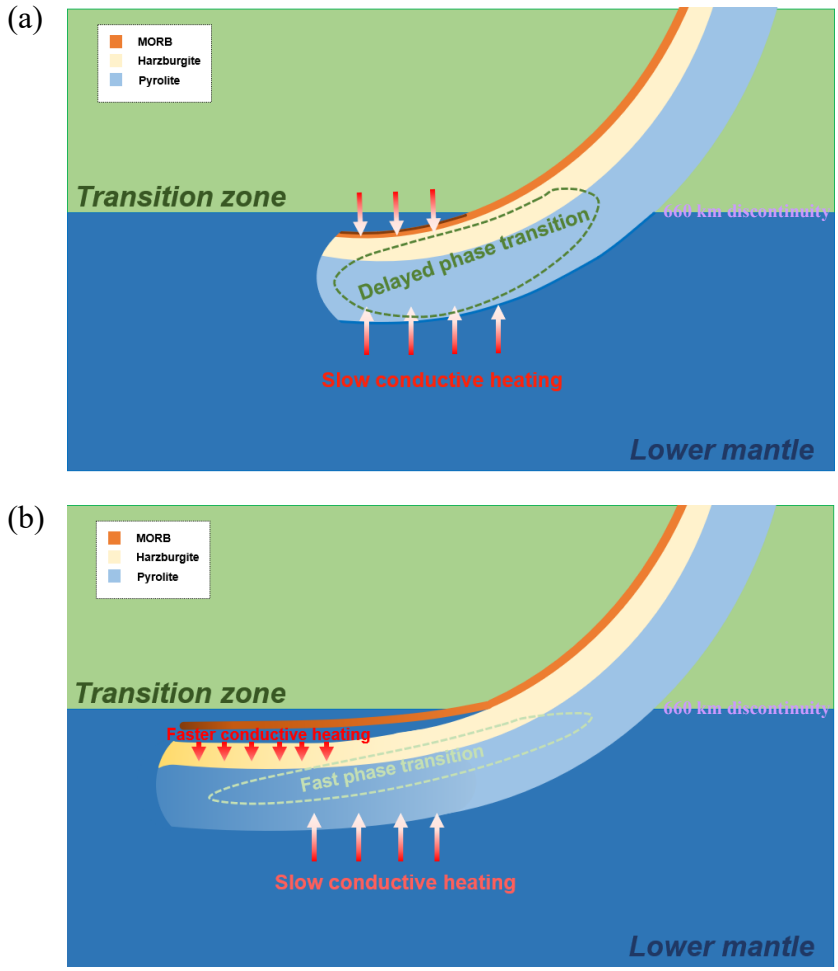

Fig. 3.11 Schematic figures for different scenarios of stagnant slabs: (a) initial stagnant of a slab at 660 km; (b) after long time subhorizontal deflection around 660 km.

Acknowledgments

First and foremost, I would like to sincerely express my gratitude to my supervisor T. Yoshino for his patient instruction and tireless support during my Ph.D. course. He is so enlightened that I can enjoy a free and flexible research life in HACTO group.

I'm grateful to M. Osako and A. Yoneda from the bottom of my heart for imparting experiment and analysis methods to me unreservedly. My growth and progress cannot be separated from their great help.

I appreciate E. Ito, D. Yamazaki, N. Tsujino a lot for their inspiring discussion in seminars and their admirable research attitude, which will benefit me forever. And many thanks to C. Zhao who help me quickly adapt to high pressure study as my tutor. Thank all the faculties and staffs in IPM for provide comfortable study and life conditions in Misasa. Also thank other students in my group for supporting each other with me in some difficult moments of research and dailylife.

Last but not least, I would like to thank my parents who give me unconditional support and considerate care. Their encouragement and love are always my driving force.

This work was supported by JSPS Research Fellowship for Young Scientists (DC2-JP21J15543 to Y. Zhang) and the Ministry of Education, Culture, Sports, Science, and Technology of the Japanese Government (Grant Numbers: 15H05827, 17H01155 and 21H04996 to T. Yoshino).